Direct Numerical Simulation of Friction Drag Reduction in Spatially Developing Turbulent Boundary Layers

March 2013

Yukinori Kametani

School of Science for Open and Environmental Systems

Graduate School of Science and Technology
Keio University

Acknowledgements

I would like to express my deepest gratitude to my supervisor, Professor Koji Fukagata. Since I started the research activity at Keio University as an undergraduate student, I have been strongly encouraged to proceed my study. Thanks to his warm support, I could challenge to expand my work widely and enjoy not only my research but also the life at the laboratory. I can clearly say that my origin as a researcher is at Fukagata Laboratory.

I appreciate Professor Shinnosuke Obi, Professor Akiko Matsuo, and Professor Takeshi Yokomori for indispensable discussion on the present thesis. Especially I would like to show my deep gratitude to Professor Shinnosuke Obi for the whole advices for not only the research but also various issues including studying abroad through the laboratory life. I am deeply grateful to Professor Pierre Sagaut at Universitè Pierre Marie Curie (UPMC). He supervised me for my work in second year of Ph.D. course in Paris. Due to his suggestion and advices, I could start a new study from a new viewpoint by using the attached eddy model. I am sure that I could grow up as a researcher working for turbulent flow through the life at UPMC.

I express my gratitude to Doctor Yoshitsugu Naka for lots of advise since I was an under graduate student. Working with him together at the beginning of my research life made me decide to head for the doctoral degree. I would like to thank all my friends in Obi-Fukagata laboratories for great and precious time. In particular, I thank Dr. Hiroya Mamori for helping me all the time.

I thank my friend,Takuya Kawata. I am very proud to have spent time with him at same laboratory since 2007.

Finally, I do appreciate to my family for supporting me all the time.

This research has been financially supported by Japan Society for the Promotion of Science (JSPS), Grant-in-Aid for JSPS Fellows, 24·3450, 2012, the silent supersonic aircraft research program of Japan Aerospace Exploration Agency (JAXA), and the Keio University Global COE program, the Center for Education and Research of Safe, Secure and Symbiotic System Design.

Abstract

Viscosity of the causes a boundary layer on a solid surface and generates skin friction drag. The large skin friction drag of turbulent flow has a huge impact on the global environment. Its reduction is required, in particular, for reducing fuel consumption in major transports such as aircrafts, trains and ships.

In this thesis, direct numerical simulations of skin friction drag reduction in spatially developing turbulent boundary layers are performed. To analyze the mechanisms, the skin friction drag, C_f, is physically decomposed into four different contributions according to the FIK identity (Fukagata et al. 2002): the contributions from boundary layer thickness, the Reynolds shear stress, mean convection, and spatial development. Furthermore, the control efficiency is important for the practical application. Two control methods are examined in the present study: uniform blowing/suction and uniform heating/cooling. As the results, the uniform blowing and uniform cooling achieved the skin friction drag reduction with different mechanisms, while uniform suction and heating enhance it. From the FIK identity, the enhancement of the mean convection term, which works as the reduction factor, plays a significant role to achieve the drag reduction due to the mass flux through the wall. On the other hand, the uniform cooling achieves skin friction drag reduction by suppression of the turbulent eddies near the wall. In terms of the control efficiency, it is found that the uniform blowing can achieve the net-energy saving, while the uniform cooling cannot achieve it.

Contents

List of Figures

List of Tables

Nomenclature

Roman Symbols

a speed of sound

C_{ij}, D^{p}_{ij}, D^{t}_{ij}, D^{ν}_{ij}, P_{ij}, ϕ_{ij}, ε_{ij} convection, pressure-diffusion, turbulent-diffusion, viscous diffusion, production, re-distribution, dissipation terms of RSTE

C_f global skin friction coefficient

c_f skin friction coefficient

C_k, D^{p}_{k}, D^{t}_{k}, D^{ν}_{k}, P_k, ε_k terms in the transport equation of turbulent kinetic energy

c_v, c_p specific heat at constant volume / pressure

f arbitrary physical quantity

g gravity constant

f_{ex} external force

c^{δ}, c^{T}, c^{C}, c^{D} Contribution from boundary layer thickness, Reynolds shear stresses, mean convection, spatial development of FIK

C^{δ}, C^{T}, C^{C}, C^{D} Contribution from boundary layer thickness, Reynolds shear stresses, mean convection, spatial development of global FIK

Gr Grashof number

k turbulent kinetic energy

L domain length

L^D Length in driver part

Ma Mach number

p pressure

Pr $\left(= \frac{\mu g c_p}{\lambda}\right)$ Prandtl number

q heat flux

R gas constant

Re_δ Reynolds number based on 99% boundary thickness

Re_{δ_m} Reynolds number based on momentum thickness

Re_τ friction Reynolds number

Re_θ Reynolds number based on momentum thickness

Ri Richardson number

T temperature

UB, US, UH, UC Uniform blowing, suction, heating, cooling.

U_i time-averaged velocity

$\overline{u_i' u_j'}$ the Reynolds stress

x, y, z the Cartesian Coordinate in streamwise, transverse and spanwise directions

x_i coordinate

Greek Symbols

δ 99% boundary thickness

δ_d Displacement thickness

δ_{ij} Kronecker delta

θ Momentum thickness in Chap. 5

γ $(=\frac{c_p}{c_v})$ specific heat ratio

λ thermal conductivity

μ viscosity

ν kinematic viscosity

ρ density

τ_{ij} stress

τ_w wall shear stress

θ Momentum thickness, (temperature in Chap. 5)

Superscripts

$*$ dimensional value

$'$ disturbance component

Subscripts

$_{ctr}$ values in controlled case

$_{ijk}$ indexing subscripts

$_\infty$ Values in free stream

$_{nc}$ values in uncontrolled case

$_0$ values at inlet

Acronyms

TCHNL Turbulent channel flow

CTA Constant Temperature Anemometer

CTR Control

DNS Direct Numerical Simulation

DRV Drive

HWA Hot-Wire Anemometer

PSD Power Spectral Density

RANS Reynolds Averaged Navier-Stokes

RSS Reynolds shear stress

STBL Spatially developing Turbulent Boundary Layer

TDMA Tridiagonal matrix algorithm

VSS Viscous shear stress.

Chapter 1

Introduction

1.1 Background

The environmental burden is one of the important global issues. Starting with the Kyoto Protocol to the United Nations Framework Convention on Climate Change adopted at COP3 in 1997, the global objectives among advanced nations to reduce the emission of the green house gasses (GHGs) have been discussed and activated. In the protocol, advanced nations put the mark to reduce 5% of whole emission of the GHGs: carbon dioxide (CO_2), methane (CH_4), nitrous oxide (N_2O), sulphuhr hexafluoride (SF_6), hydrofluorocarbons (HFCs), and perfluorocarbons (PFCs). Although Japanese government announced 6% of the reduction of GHS compared to the ones in year 1990 by 2012, it has not been achieved by the government yet due to other domestic issues like the reconstruction from the Earthquake at Tohoku-coast in March 2011, economics, or other financial issues.

In order to prevent the exhaustion of fossil fuels, new energy sources such as the methane hydrate, solar, hydrogen, and nuclear power have been developed. The fossil fuels, however, still occupy the majority of the energy sources in the society due to their cost-effective performance. Therefore, cost-effective and energy-effective utilization of the present fuels has also been a controversial and important issue.

From the viewpoint of social demands, the public transports such as aircrafts, bullet trains, and ships are tend to be accelerated for shortening traveling time. This fact indicates the increase of fuel consumption and GHG emission. Figure 1.1 shows the trends of transport use in France from 19th century. This figure presents the increasing

Table 1.1: Source of the energy

Total	21,565 [$\times 10^{15}$ J]
Atomic power plant	2,248
Hydroelectric, geothermal, etc.	1,334
Natural gas	4,019
Petroleum	9,042
Coal	4,922

Table 1.2: End energy consumption

Total	14,726 [$\times 10^{15}$ J]
Household use	2,056
Business use	2,920
Passenger-transports	2,134
Freight-transports	1,341
Industries	6,273

social demand of the transports systems and also indicates that the fuel consumption increases exponentially. It is clear that the energy consumption increases as time goes by. The large carrier-capacity and faster transports are still being pursued. Since the improvement of efficiency of the fuel combustion results in cost-down, the social demand in skin friction drag reduction is becoming more important in business.

The ministry of Environment in Japan reports some statistical data about energy consumptions. The data are referred from the database of Ministry of the Environment (http://www.env.go.jp). Tables 1.1 and 1.2 show the energy source and the end usage of the energy in the Japanese society. In the process of production or usage of energy, the approximately 30% of energy is lost in the end. As seen in Tables 1.1 and 1.2, over 20% of the total produced energy is consumed for transportation of people and freights.

Figure 1.2 shows the energy consumption of various transports in Japan in 2011. From Fig. 1.2 (a), for people-transports, a dominant use is from cars (about 80%) but that from airplane cannot be ignorable because it reaches around 10%. Furthermore, the role of aircrafts is quite important in modern society due to their ability of the traveling distance. On the other hand, for freight-transports, the energy use from ships is secondly dominant in total use in Japan as shown in Fig. 1.2 (b). Thanks to the effort of the development in the field of cars, the energy consumption has decreased from 2005 to 2010. Although the total amount of energy consumption has been maintained or reduced in the recent few years in Japan after COP3, it is more than that of ten years ago.

Suppression of the gas emission by improving combustion efficiency has been pursued for the transports. The drag of fluid flow is one of the causes of the increase of fuel consumption. The drag of the fluid flow includes, mainly, pressure drag by flow separation and skin friction drag by viscosity of the fluid. The engineers and scientists have achieved the reduction of pressure drag, for example, by streamlinear shape. The skin friction drag is caused by the formation of boundary layers as shown in Fig. 1.3. The chaotic motion of the flow by turbulent transition of the boundary layer enhances skin friction drag. The reduction of skin friction drag has also been studied but it is not practical yet due to their difficulty in their size or maintenance to be considered. For instance, the riblets, the fine V-groove, on the wall-surface have been examined (see Garcia-Mayoral and Jiménez, 2011). Airbus Company examined the riblets with A320 and achieve a few percent of fuel-saving. From the maintenance cost and their durability, however, the riblets are still not appropriate for commercial use.

Skin friction drag reduction is one of promising ways for saving energy consumption but it is still a challenging issue.

1.2 Previous work

1.2.1 Spatially developing turbulent boundary layers

Existence of viscosity generates velocity deficit by viscous diffusion between solid a surface and fluid flow, viz., energy loss. More than one hundred years have passed since the seminal lecture by Ludwig Prandtl in 1904, where he introduced the boundary-layer concept. Despite the considerable progress in the last century, even the simplest quantity, i.e., the mean streamwise velocity component, in the seemingly simplest flow fields, i.e., the fully developed turbulent channel and pipe flow as well as the zero-pressure-gradient (ZPG) spatially developing turbulent boundary layer (STBL), is still far from being fully understood. Turbulent flow in a channel and a pipe can achieve the fully developed condition, while STBL cannot achieve this due to the nature of spatial development. These are categorized into the 'internal flow' and the 'external flow,' respectively. In the present thesis, the STBL is focused, targeting the flow which appears around transports systems.

1.2.2 Numerical investigations of turbulent wall-bounded flow

The motion of fluid flow includes eddies of various scales. It is difficult to know all information of the physical variables such as velocity, pressure or thermodynamical properties, which are invisible. A numerical simulation enables us to know these pieces of information. The pioneering work was done by Smagorinsky (1963) as a large eddy simulation (LES) for atmospheric flow in meteorology. Later, Deadorff (1970) and Schumann (1975) performed LES of turbulent flow bounded by walls.

Owing to the development of numerical schemes and the progress of computers in 1980's, analysis of turbulence using numerical simulation has extensively been performed. Today, the numerical simulation has become a major tool for the research of skin friction drag reduction. Although the surfaces appearing in the practical transports such as aircraft or trains are geometrically complex, it is important to investigate the physics of skin friction drag reduction in simple geometries to know the essence of viscous phenomena. Therefore, the numerical simulation in the canonical flows like channel, pipe and spatially developing plane boundary layer is attractive.

Direct numerical simulation (DNS) is a powerful tool to analyze the behavior of turbulence because its motion is calculated without any turbulent models, viz., the simulation just obeys the governing equations. Although the Reynolds number is limited to be low due to the computational cost, the DNS is still a powerful tool to analyze the mechanism of skin friction drag because the wall-turbulent flows owes a universal structure arranged by wall units: friction velocity, $u_\tau^* = \sqrt{\tau_w^*/\rho^*}$, and kinematic viscosity, ν^*, where superscript * denotes dimensional values. In the wall units, the velocity and the length are non-dimensionalized as

$$U_i^+ = \frac{U^*}{u_\tau^*} \,, \tag{1.1}$$

$$x_i^+ = \frac{u_\tau^* x_i^*}{\nu^*} \,. \tag{1.2}$$

While early DNS employed the spectral method, which had been the sole method to stably and accurately simulate turbulent flows without introducing upwinding (which introduces numerical diffusion), flow geometry was limited to some canonical flows. The numerical diffusivity of upwind scheme for advection term causes unphysical phenomena, generating excessive viscosity in the numerical simulation. To avoid such numerical viscosity, a stable and non-diffusive (i.e., energy conservative) finite difference method (FDM) had been explored for long time.

Since the energy conservative second-order FDM on the uniform grid was proposed by Harlow (1965) or Piacsek and Williams (1970) in the early 1960's, the method for practical numerical configurations (such as higher order FDMs, nun-uniform grid. etc.) had been strongly pursued for thirty years. Morinishi et al. (1998) reported a class of energy-conservative FDMs on uniform Cartesian grids including generalization to higher order FDMs. Subsequently, Kajishima (1999a) (also Bewley, 1999; Ham et al., 2002) extended its second order version to a non-uniform Cartesian grid. Moreover, energy conservative FDM has been extended to, e.g., the cylindrical coordinates (Fukagata and Kasagi, 2002b; Morinishi et al., 2004), arbitrary orthogonal curvilinear coordinates (Nikitin, 2006) and the low Mach number approximation (Desjardins et al., 2008).

1.2.3 Turbulent structures in wall-bounded flow

The wall turbulence has been studied since the 19th century. Turbulent structures in wall-bounded flow have been attractive issues for a few decades with the great development of computer and measurement method. Smith and Metzler (1983) found that the streamwise length and the spanwise spacing of the low-speed streaks are about 100 ν^*/u_τ^* (wall-units) and 1000 ν^*/u_τ^*, respectively. The remarkable phenomena caused by the vortex structures are the ejection and the sweep. These phenomena were analyzed by Chen and Blackwelder (1976), i.e., the quadrant analysis for the decomposition of the Reynolds shear stress. The ejection, which is the motion of low speed-fluid moving away from the wall, is caused by the rotation of the vortex structure. On the other hand, the sweep attracts the high speed-fluid toward the wall. Jimenez and Moin (1991) presented a minimal channel unit: the domain size wider than 100 ν^*/u_τ^* in spanwise direction sustains turbulence, whereas a narrower box can not sustain it. Subsequently, Hamilton et al. (1994) proposed a regeneration cycle among streaky structures, the streamwise-dependent disturbances and streamwise vortices, in the minimum channel flow.

A lot of vortices are generated near the wall, which are called quasi-streamwise vortices (QSV). The diameter of QSV is around $25-30$ ν^*/u_τ^* and the streamwise length is $150-300$ ν^*/u_τ^* (Kasagi et al., 2004). This QSV appears in the buffer layer, where the turbulent kinetic energy (TKE) production takes a peak (Robinson, 1991). It is known that QSV increase the skin friction drag exceedingly.

As the Reynolds number increases, the large-scale structure, which owns long wavelength in the streamwise direction in the outer layers of STBLs, appears. One of the hot issues is how the turbulent kinetic energy of the large scale motion affects the turbulent intensities, the Reynolds shear stress or skin friction drag. Marusic et al. (2010a) decomposed the velocity fluctuations from the experiment of HW into the small-scale motion and the large scale motion. The second peak in the power spectra density (PSD) of streamwise fluctuation was presented (also see the Ganapathisubramani et al., 2003). Later, Hutchins et al. (2011) performed the measurement with the spanwise array of hot film sensor, and illustrate the streamwise vortex meandering near the wall. Moreover, the behavior of the induced streamwise vortices by the vortex generator near the wall was observed by Lögdberg et al. (2009) and they found the 'hooklike' vortex core motion.

Although the large structures is important for the turbulent structures in the practical cases, its analysis by the DNS had been impossible because it dependeded on the machine performance. The recent progress in the high performance computers enable to investigate higher Reynolds number flows by DNS, e.g., $Re_\tau \approx 590$ by Moser et al., 1999, $Re_\tau \approx 1020$ by Abe et al., 2004, $Re_\tau \approx 1160$ by Iwamoto et al., 2004, $Re_\tau \approx 2000$ by Hoyas and Jimenez, 2006, $Re_\tau \approx 2320$ by Iwamoto et al., 2005. Due to this development of the performance of the computers, the large-scale structure can be found in DNS. In these days, the focus are directed to the ones in spatially developing turbulent boundary layers as well as the internal flows such as channel or pipe turbulence (see Monty et al., 2009; Schlatter and Örlü, 2010).

1.2.4 Decomposition of skin friction drag

Fukagata et al. (2002a) derived the identity equation which decomposes the skin friction drag into different components, called the FIK identity. This identity enables us to evaluate the control effect and its mechanisms physically and quantitatively. The skin friction in turbulent channel flow, for instance, is decomposed into contributions from the laminar component and Reynolds shear stress. For the spatial developing turbulent boundary layers, the skin friction drag is decomposed into four contributions (see Chap. 2). The FIK identity is applied to various controlled flow field, e.g., for spanwise wavy wall by Peet and Sagaut (2009), wall-deformation channel by Nakanishi et al. (2012), or supersonic wall-turbulence by Gomez et al. (2009).

1.2.5 Skin friction drag reduction control

Despite the extensive research conducted, a practical method for skin friction drag is still being explored. The drag exerted by the fluid flow is mainly composed of the skin friction drag and the pressure drag caused by the flow-separation. Although the pressure drag is reduced by the streamliner shaping, easily found in shapes of bullet trains and local trains in Japan, reduction of skin friction drag is still far from practice and under investigation. The skin friction drag, however, accounts for about 50% in total drag appears on the surface of commercial aircrafts, for instance (Gad-el Hak, 1996). The control schemes are mainly categorized into two: passive control and active control, as shown in Fig. 1.4. The active control, which charges the energy into the flow by some form, is attractive due to its potential for significant amount of drag reduction. Especially, the predetermined control, which can be performed without using any sensors, is strongly focused to save the financial cost for fabrication.

A variety of ideas for skin-friction drag reduction have been examined, especially since the late 1980's following the emergence of direct numerical simulation (DNS) of wall-bounded flow (Kim et al., 1987), as shown in Fig. 1.5. These studies have recently been reviewed, e.g., by Kim (2003) on the feedback control schemes, Kim and Bewley (2007) on the linear control theory, Kasagi et al. (2009b) on the hardware and practical control schemes, and White and Mungal (2008) on the skin friction drag reduction by polymer additives.

Most of the previous numerical studies on friction drag reduction have dealt with internal flows, such as channel flows (see e.g., Kim (2003); Kim and Bewley (2007); Kasagi et al. (2009b) and references therein). A theoretical framework is also better established for internal flows: for instance, we now know the mathematical relationship between the Reynolds stress and friction drag (Fukagata et al., 2002a) and the theoretical limit of active friction drag reduction control for flows in a plane channel (Bewley, 2009) and in arbitrary ducts (Fukagata et al., 2009). No such limit, however, is currently known for external flows as stated in the recent review by Choi et al. (2008).

In comparison to channel flows, much fewer studies have been reported for spatially developing turbulent boundary layers, even though practical friction drag reduction control should be targeted at the external flows (since in internal flows a slight increase in pipe diameter is sufficient to significantly reduce the pumping power). Recently, however, the analysis in the spatially developing boundary layer has also been advanced. Park and Choi (1999) and Kim et al. (2002) performed DNS with steady blowing or suction from a localized spanwise slot. They concluded that blowing reduces the skin friction drag and suction increases it; blowing shifts the turbulence away from the wall and enhances it and suction has the opposite effect. More recently, Pamiès et al. (2007) have performed large eddy simulations of a spatially developing turbulent boundary layer using the opposition control of Choi et al. (1994). They also examined the case of uniform blowing (UB) in combination with opposition control. A larger drag reduction than that of the opposition control alone was achieved.

Kim et al. (2003) performed DNS of STBL with injection or suction through the slot on the wall-surface. They investigated the effect of the control on the pressure fluctuation, skin friction drag and pressure drag. Brillant et al. (2004) performed LES of STBL at $Re_l = 850,000$ with porous wall. The results were compared with the experimental work of Bellettre et al. (2000). Vigdorovich (2005) analytically investigate the effect of the uniform blowing on the skin friction drag and the displacement thickness by using the time averaged boundary layer equation. The result agreed with the experiment of blowing control of Simpson et al. (1969). Kim and Sung (2006) performed DNS of STBL with time-periodic blowing from a slot. They investigate the effect of periodic control-input on the flow field from phase-averaged data. As for the relation between input and output, Bagheri et al. (2003) and Scherader et al. (2009) numerically investigated the control input and its output by using Navier-Stokes equation from the viewpoint of the control engineering.

1.2.5.1 Uniform blowing/suction

The blowing and suction of the flow through the wall-surface are used in engineering applications. For example, the blowing is used for turbine-film cooling to prevent damage by the heat and to achieve high performance of the turbine. On the other hand, suction is often used in slotted wing to avoid flow separation or prevent the flow from turbulent transitions. The UB is also attractive as a means for skin friction drag, as illustrated by the results of Pamiès et al. (2007). The modification of turbulence by UB and US has bean studied in detail by Sumitani and Kasagi (1995) by using direct numerical simulation (DNS) of turbulent channel flow. They found that the Reynolds shear stress increase on the blowing side and decreases on the suction side; by contrast, the friction drag reduces on the blowing side and increases on the suction side. This somewhat peculiar trends (also found in the blowing/suction slot case by Park and Choi (1999) was explained by identity equation between the Reynolds shear stress and the friction drag (Fukagata et al., 2002a). This identity described in detail in the next section) was applied to the Sumitani and Kasagi (1995) case revealed the following mechanism: on the blowing side, where the Reynolds shear stress is increased, convection due to the mean wall normal velocity contributes to drag reduction; the opposite was found on the suction side. For the numerical condition, both of uniform blowing and suction have to be perform simultaneously to keep net mass in the channel, viz., the effect on the shear flow of each cad: blowing or suction, are not discussed individually. Both characters of the mass injection in blowing and suppression the turbulent transition in suction possibly reduces the skin friction drag. Due to this, it is necessary to investigate the effect of the uniform blowing and suction and their mechanisms in spatially developing turbulent boundary layer as an examination in an external flow.

1.2.5.2 Uniform cooling/heating

One of the attractive media for friction drag reduction is body force. Buoyancy is a body force in the gravitational direction generated by the temperature difference between the wall and mainstream in the gravitational direction. Buoyancy convects the fluid and transports turbulent energy in the engineering flow field or geophysical one. Due to buoyancy, thermal stratification is made in boundary layers. Iida and Kasagi (1997) and Iida and Kasagi (2002) performed DNS of turbulent channel flow under stable and unstable density stratification, respectively. They found that under weakly unstable density stratification, skin friction drag was reduced due to suppression of streamwise vortices near the wall. They also showed that it is possible to relaminarize the flow at large amplitude of Richardson number. The DNS of spatially developing turbulent thermal boundary layer under stable/unstable stratification was investigated by Hattori et al. (2007) to assure the dissipation of contaminant in the atmospheric phenomena. The results were found to be in accordance with the finding in a channel flow. These results suggest the possibility of turbulence control using the buoyant force with uniform wall-surface heating (UH)/cooling (UC) in external turbulent flows. Moreover, the wall-heating or cooling is supposed to be applied in practice more easily than uniform blowing/suction from the wall due to the ease to drive the uniform force on the wall. To treat the buoyancy as a control media, clarification of the mechanism of reduction or enhancement of friction drag by buoyancy is necessary.

1.2.6 Control efficiency

Due to the effort of scientists and engineers, the drag reduction has been achieved by various methods mentioned above. Theoretical consideration for skin friction drag reduction control has been studied for last decade years. From the viewpoint of the practical applications, it is necessary to indicate the efficiency of the controls to consider not only the theories but also the applications. In this thesis, the efficiency is argued by two parameters: a gain, G, and a net-energy saving rate, S. A gain expresses how much drag reduction is obtained by unit input power, while a net-energy saving rate expresses how much energy is saved. The mathematical details are mentioned in Chap. 2.

Fukagata et al. (2009) mathematically proved the limitation of the power balance in a fully developed duct flow:

> *The lowest net power required to drive an incompressible constant mass-flux flow in a periodic duct having arbitrary constant-shape cross-section, when controlled via a distribution of zero-net mass-flux blowing/suction over the no-slip channel walls or via any body forces, is exactly that of the Stokes flow.*

This sentence indicates the possibility of the skin friction drag reduction to achieve the net energy-saving. Other way to discuss the application is done by Frohnapfel et al. (2012). They mentioned the evaluation of the control effect for the view of the energy consumption and convenience, viz., the reducing the fuel consumption or faster traveling speed.

1.3 Objective and organization of this thesis

The objective of the present thesis are to investigate the effect of uniform/blowing and uniform heating/suction in a spatially developing turbulent boundary layer by using direct numerical simulation. By using FIK identity, the mechanism of the skin friction drag reduction is quantitatively surveyed. This thesis is composed as following.

In Chap. 2, the theoretical and mathematical bases of the present study are presented including the governing equations of the fluid motion, the Reynolds Averaged Navier-Stokes equation (RANS), the FIK identity, the definitions of boundary layers and control efficiency.

In Chap. 3, the details of direct numerical simulation performed in present study is presented. The base flow is simulated to validate this code by using some statistical features. This codes are verified by comparing with Wu and Moin (2009)

In Chap. 4, DNS with uniform blowing or suction is performed. The input parameter is the amplitude of wall normal velocity on the wall. The physics and reduction/enhancement mechanisms are investigated.

In Chap. 5, DNS with uniform heating or cooling is performed. The input parameter is the Richardson number. The buoyancy is applied in DNS by using the

Boussinesque approximation. The physics and reduction/enhancement mechanisms are investigated.

Finally, the achievements in the present thesis are summarized in Chap. 6.

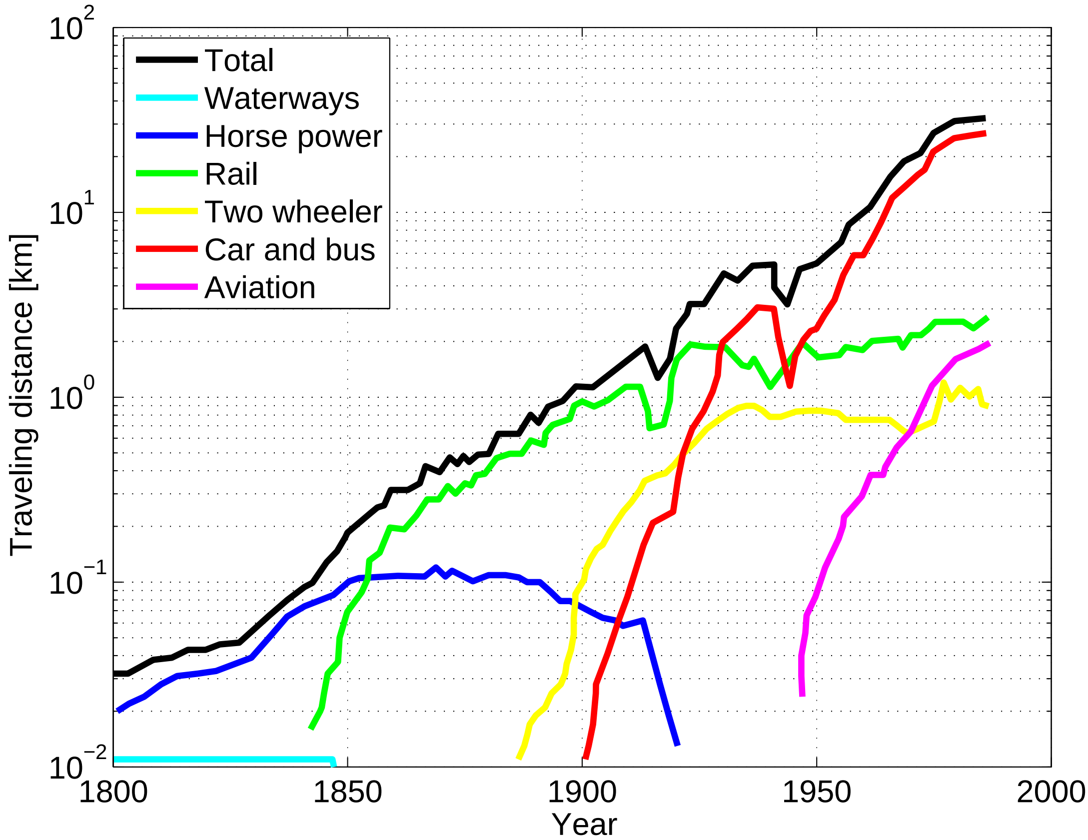

Figure 1.1: Travel distance per full day 1800−2000, France (excluding walk). Data referred from Banister et al. (2011)

(a)

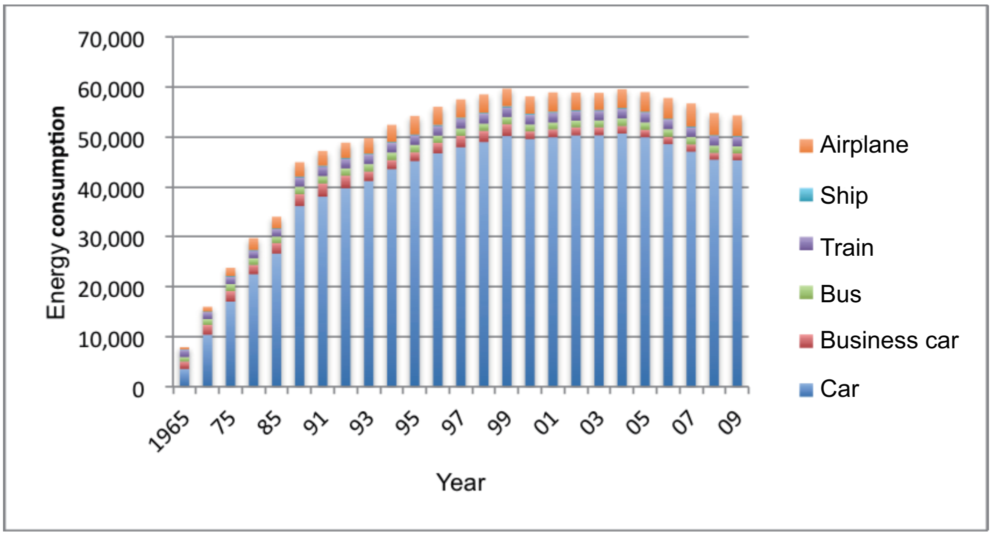

(b)

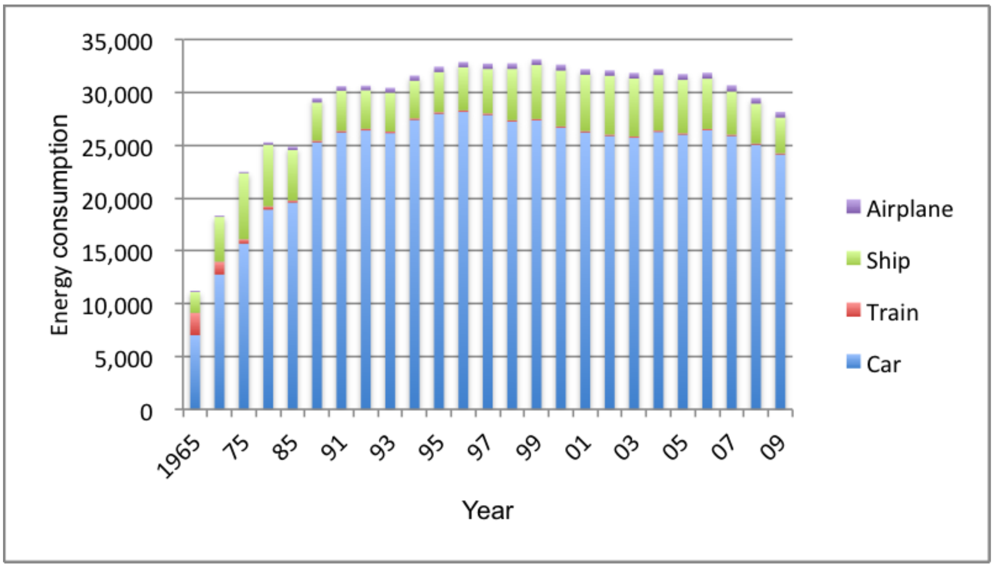

Figure 1.2: Change of energy consumption ($\times 10^{10}$ kcal). (a) transports for people. (b) transports for freight.

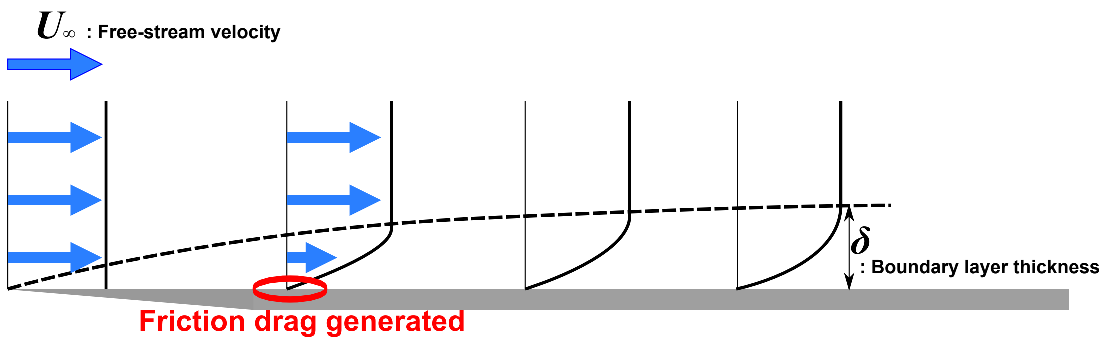

Figure 1.3: Spatially developing boundary layer

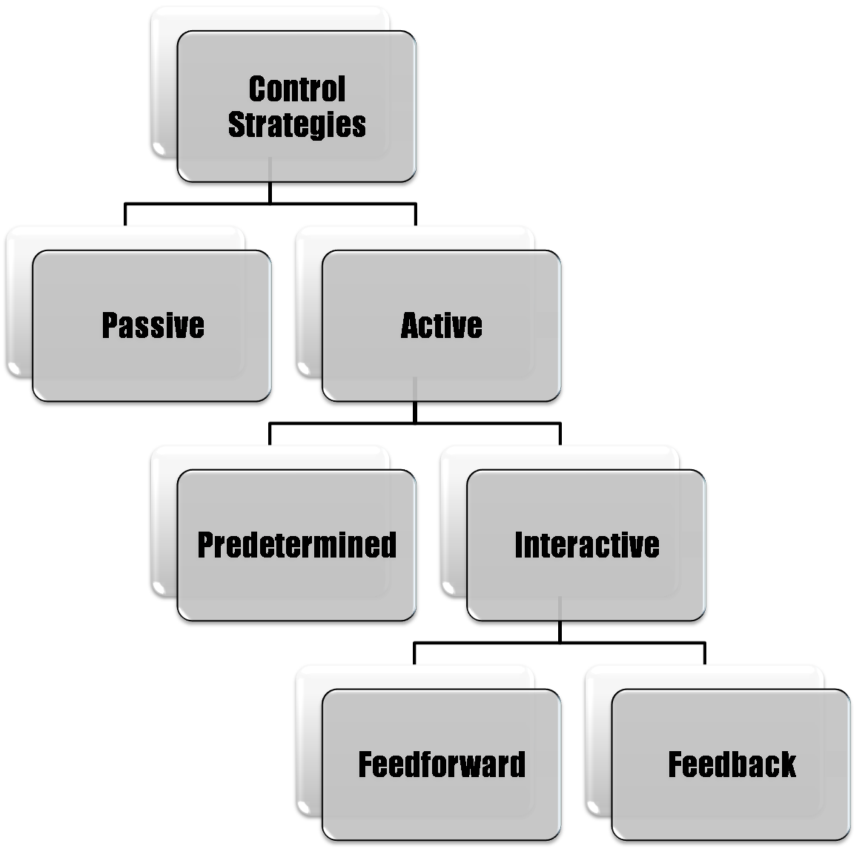

Figure 1.4: Strategic category for flow controls.

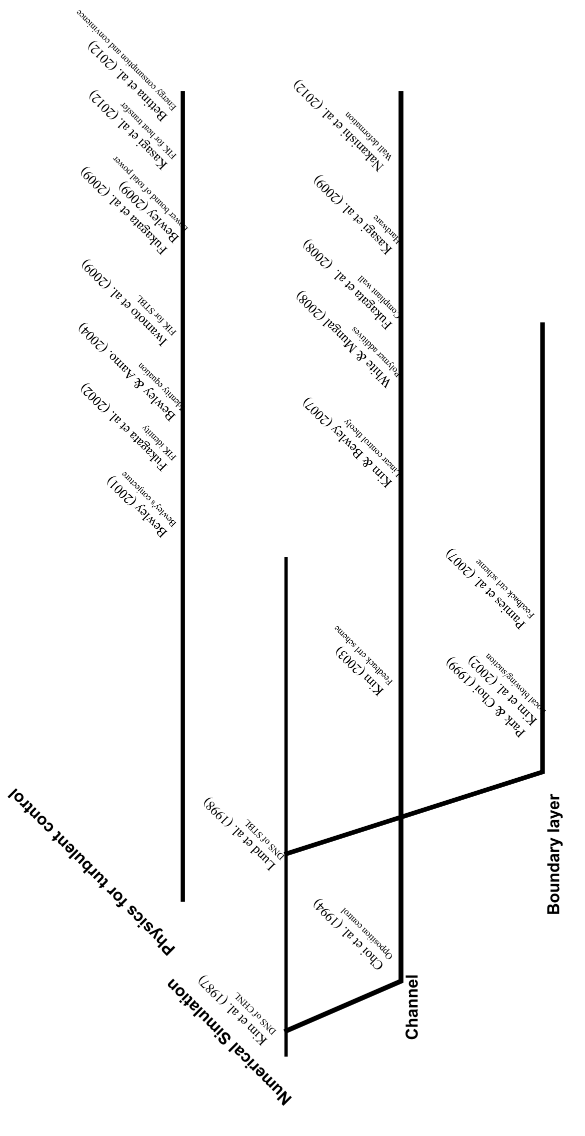

Figure 1.5: History of the work on skin friction drag reduction control.

Chapter 2

Theoretical preparations

2.1 Governing equations for the fluid motion

The motion of fluid is governed by three conservation laws: the conservation of mass, momentum and energy as the continuity, the Navier-Stokes and the energy equation;

$$\frac{\partial \rho^*}{\partial t^*} = -\frac{\partial \rho^* u_i^*}{\partial x_i^*} \tag{2.1}$$

$$\frac{\partial \rho^* u_i^*}{\partial t^*} = -\frac{\partial \rho^* u_i^* u_j^*}{\partial x_j^*} - \frac{\partial p^*}{\partial x_i^*} + \frac{\partial \tau_{ij}^*}{\partial x_j} + f_i^* \tag{2.2}$$

$$\frac{\partial \rho^* T^*}{\partial t^*} = -\frac{\partial \rho^* T^* u_i^*}{\partial x_i^*} - p^* \frac{\partial u_i^*}{\partial x_i^*} + \frac{\partial q_i^*}{\partial x_i} + \tau_{ij}^* \frac{\partial u_i^*}{\partial x_j^*} \tag{2.3}$$

where x_i (i =1, 2, 3) are the Cartesian coordinates and u_i are the corresponding velocity components. The stress tensor τ_{ij} and heat flux vector q_i are composed as

$$\tau_{ij}^* = \mu^* \left(\frac{\partial u_i^*}{\partial x_j^*} + \frac{\partial u_j^*}{\partial x_i^*} - \frac{2}{3} \frac{\partial u_k^*}{\partial x_k^*} \delta_{ij} \right), \tag{2.4}$$

where δ_{ij} denotes Kronecker's delta, and

$$q_i^* = -\lambda^* \frac{\partial T_i^*}{\partial x_j^*}, \tag{2.5}$$

where λ denotes thermal conductivity, respectively. In the present thesis, since the air or water flows are assumed, the property of fluid can be considered as the newtonian and the Stoke's hypothesis is assumed for τ^*_{ij}. Assuming the incompressible flow, the continuity, Navier-Stokes and energy equation reduce to

$$\frac{\partial u^*}{\partial x^*_i} = 0, \tag{2.6}$$

$$\frac{\partial u^*}{\partial t^*} = -\frac{\partial u^*_{ij}}{\partial x^*_j} - \frac{\partial p^*}{\partial x^*_i} + \nu^* \frac{\partial^2 u^*_i}{\partial x^*_j \partial x^*_j}, \tag{2.7}$$

$$\frac{\partial T^*}{\partial t^*} = -\frac{\partial T u^*_j}{\partial x^*_j} + \lambda^* \frac{\partial^2 T^*}{\partial x^*_j \partial x^*_j}. \tag{2.8}$$

2.2 Reynolds decomposition and Reynolds averaging

To analyze the turbulent phenomena, the time-averaged governing equations are helpful. The Reynolds-averaging is based on Reynolds decomposition firstly proposed by Reynolds (1895) which decomposes the quantities as

$$f = F + f', \tag{2.9}$$

where f is the instantaneous value of an arbitrary quantity, H stands for time-averaged value, and f' means the fluctuating component.

After applying this procedure, the continuity equations for time-averaged and fluctuating velocity components are obtained as follows:

$$\frac{\partial U^*_i}{\partial x^*_i} = 0, \quad \frac{\partial u^{*\prime}_i}{\partial x^*_i} = 0. \tag{2.10}$$

In the same manner, the Reynolds Averaged Navier-Stokes (RANS) equation can be obtained from Navier-Stokes equation (2.2):

$$\rho^* \left(\frac{\partial U^*_i}{\partial t^*} + U^*_j \frac{\partial U^*_i}{\partial x^*_j} \right) = -\frac{\partial P^*}{\partial x^*_i} + \frac{\partial^*}{\partial x^*_j} \left(\mu^* \frac{\partial U^*_i}{\partial x^*_j} - \rho^* \overline{u^{*\prime}_i u^{*\prime}_j} \right). \tag{2.11}$$

The additional Reynolds stress term is found in the right hand side of the momentum equation (2.11). The Reynolds stress term represents the momentum transport by turbulence.

The transport equation of the Reynolds stress is obtained from the Navier-Stokes equation:

$$
\begin{aligned}
\underbrace{\frac{\partial \overline{u_i^{*\prime} u_j^{*\prime}}}{\partial t^*}}_{\text{Unsteady}} + \underbrace{U_k^* \frac{\partial \overline{u_i^{*\prime} u_j^{*\prime}}}{\partial x_k^*}}_{\text{Convection: } C_{ij}} &= \underbrace{-\overline{u_j^{*\prime} u_k^{*\prime}} \frac{\partial U_i^*}{\partial x_k^*} - \overline{u_i^{*\prime} u_k^{*\prime}} \frac{\partial U_j^*}{\partial x_k^*}}_{\text{Production: } P_{ij}} \underbrace{-2\nu^* \overline{\frac{\partial u_j^{*\prime}}{\partial x_k^*} \frac{\partial u_i^{*\prime}}{\partial x_k^*}}}_{\text{Dissipation: } \varepsilon_{ij}} \\
&\underbrace{-\frac{1}{\rho^*} \frac{\partial}{\partial x_k^*} \left(\rho^* \overline{u_i^{*\prime} u_j^{*\prime} u_k^{*\prime}} + \overline{p^* u_j^{*\prime}} \delta_{ik} + \overline{p^* u_i^{*\prime}} \delta_{jk} \right)}_{\text{Turbulent Diffusion: } D_{ij}^t + \text{Pressure Diffusion: } D_{ij}^p} \\
&\underbrace{+\frac{1}{\rho^*} \overline{p^* \left(\frac{\partial u_i^{*\prime}}{\partial x_j^*} + \frac{\partial u_j^{*\prime}}{\partial x_i^*} \right)}}_{\text{Re-distribution: } \phi_{ij}} \underbrace{+\nu^* \frac{\partial}{\partial x_k^*} \left(\frac{\partial \overline{u_i^{*\prime} u_j^{*\prime}}}{\partial x_k^*} \right)}_{\text{Viscous Diffusion: } D_{ij}^\nu}
\end{aligned}
\tag{2.12}
$$

Terms in the Reynolds stress transport equation are classified according to their physical interpretation. Among these terms, the re-distribution and the pressure-diffusion terms which originally come from the velocity-pressure-gradient term contain the fluctuating pressure.

The transport equation of the turbulent kinetic energy, $k = \overline{u_i'^* u_i'^*}/2$, can be obtained by taking the trace of the Eq. (2.12) and divided by 2.

$$
\frac{\partial k^*}{\partial t^*} + \underbrace{U_j^* \frac{\partial k^*}{\partial x_j^*}}_{C_k} = \underbrace{-\frac{1}{\rho^*} \frac{\partial \overline{u_i' p'}^*}{\partial x_i^*}}_{D_k^p} \underbrace{-\frac{\partial u_j'^* (\overline{u_i'^* u_i'^*}/2)}{\partial x_j^*}}_{D_k^t} + \underbrace{\nu^* \frac{\partial^2 k^*}{\partial x_i^* \partial x_i^*} x_i}_{D_k^\nu} \underbrace{- \frac{\partial U_i^*}{\partial x_j^*} \overline{u_i' u_j'}}_{P_k} \underbrace{- \nu^* \overline{\left(\frac{\partial u_i^{*\prime}}{\partial x_j} \right)^2}}_{\varepsilon_k} .
\tag{2.13}
$$

The re-distribution term in Eq. (2.12) mathematically turns to be zero. The the rolls of each term in the transport equations are expressed in Fig. 2.1

2.3 Friction coefficient

Skin friction drag, τ_w, is denoted as

$$
\tau_w^*(x) = \rho^* \left. \frac{\partial U^*(x,y)}{\partial y^*} \right|_w . \tag{2.14}
$$

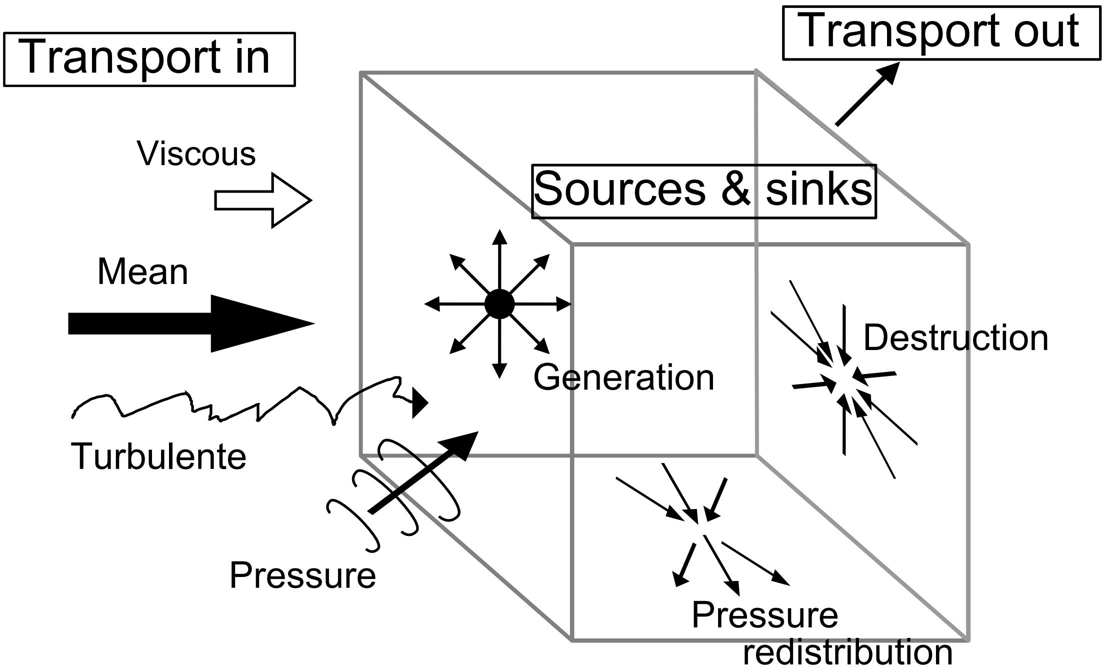

Figure 2.1: Control volume for transport equations in turbulent flow (Bradshaw, 1978)

By non-dimensionalization by kinetic pressure, a friction coefficient, $c_f(x)$, is given as

$$c_f(x) = \frac{\tau_w^*(x)}{\frac{1}{2}\rho^* U_\infty^{*2}} \ . \tag{2.15}$$

The global skin friction drag on the plate with streamwise length l, $D(l)$, is expressed as

$$D(l)^* = b^* \int_0^{l^*} \tau_w(x) \ dx \ , \tag{2.16}$$

where b denotes a width of the plate. $D(l)$ is non-dimensionalized by kinetic pressure and an area of plate as global friction coefficient, C_f;

$$C_f = \frac{D^*(l^*)}{\frac{1}{2}\rho^* U_\infty^{*2}} \ . \tag{2.17}$$

Therefore, the relation between the friction coefficient and the global friction coefficient is expressed as following;

$$C_f = \frac{1}{l} \int_0^l c_f(x) \ dx. \tag{2.18}$$

2.4 The 'thicknesses' of the boundary layers

The thickness of the boundary layer is expressed by three forms in this thesis; the 99% boundary layer thickness, δ, the displacement thickness, δ_d, and the momentum thickness, θ or δ_m. The 99% boundary layer thickness is the distance from the wall where the velocity reaches 99% of the free-stream velocity. The displacement thickness and the momentum thickness are define as

$$\delta_d(x) = \int_0^\infty [1 - U(x,y)]\ dy \tag{2.19}$$

$$\tag{2.20}$$

and

$$\theta(=\delta_m) = \int_0^\infty [U(x,y)\,(1 - U(x,y))]\ dy, \tag{2.21}$$

respectively. The brief schematic of these thickness are shown in Fig. 2.2. Because of the various definition of the thickness, Reynolds number of boundary layer are composed with free-stream velocity, kinematic viscosity and different reference length: 99% boundary layer thickness δ^*, displacement thickness δ_d^*, momentum thickness θ^* , a distance from leading edge x^* and whole streamwise length of the plate l, as $Re_\delta(=Re)$, Re_{δ_d}, Re_θ, Re_x, and Re_l.

2.5 Von Kàrmàn momentum equation

By order-evaluation, the streamwise momentum equation of a plane boundary layer is reduced to

$$\frac{\partial u^*}{\partial t^*} + u^* \frac{\partial u^*}{\partial x^*} + v^* \frac{\partial u^*}{\partial y^*} = -\frac{1}{\rho^*}\frac{\partial p^*}{\partial x^*} + \nu^* \frac{\partial^2 u^*}{\partial y^* \partial y^*}. \tag{2.22}$$

Integrating in wall-normal direction from $y = 0$ to ∞ and using continuity equation, we get von Kàrmàn momentum equation as

$$\frac{\partial U_\infty^* \delta_d^*}{\partial t^*} + \frac{\partial U_\infty^{*2} \theta^*}{\partial x^*} + \delta_d^* U_\infty^* \frac{\partial U_\infty^*}{\partial x^*} = \frac{\tau_w^*}{\rho^*}\ . \tag{2.23}$$

With the conditions of

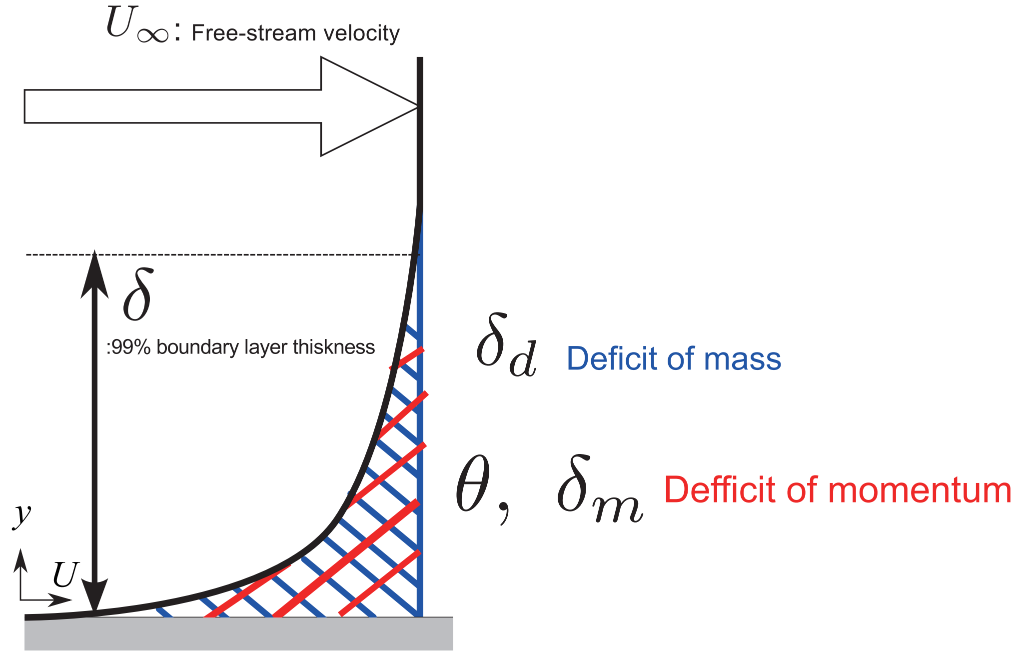

Figure 2.2: Thickness of boundary layers

- time averaged equation,
- constant free-stream velocity,
- no steramwise pressure gradient,
- non-dimensionalization by U_∞^* and δ_0^* ,

the equation is reduced to

$$\frac{\partial\theta(x)}{\partial x} = \frac{c_f(x)}{2}. \tag{2.24}$$

This relation indicates that the skin friction drag in STBL and the streamwise developing rate of the momentum thickness are equivalent. Adding the condition of constant wall-normal velocity, V_w, as blowing/suction in integration of continuity equation, the equation becomes

$$\frac{\partial\theta(x)}{\partial x} = \frac{c_f(x)}{2} + V_w, \tag{2.25}$$

which indicates the skin friction drag can balances the streamwise developing rate of the momentum thickness substituted by blowing or suction velocity.

2.6 Empirical equations for skin friction drag

An n th-power law can be assumed for the profile of streamwise mean velocity as

$$\frac{U(x,y)^*}{U_\infty^*} = \left(\frac{y^*}{\delta^*}\right)^{1/n} . \tag{2.26}$$

For a smooth flat plate, $n = 7$ ($Re_\delta = U_\infty^* \delta^*/\nu^* = 3000 \sim 70000$). From the Eq. 2.26, the Blasius equation for spatially developing boundary layers is given as

$$c_f(x) = 0.01125 \left(\frac{U_\infty^* \delta^*(x)}{\nu^*}\right)^{-1/4} . \tag{2.27}$$

Moreover, the relationship among the 99% boundary layer thickness, δ^*, the displacement thickness, δ_d^*, and the momentum thickness, θ^* are

$$\delta_d^* = \frac{\delta^*}{n+1} = \frac{\delta^*}{8} , \tag{2.28}$$

$$\theta^* = \frac{\delta^*}{(n+1)(n+2)} = \frac{7}{72}\delta^* . \tag{2.29}$$

Substituting Eq. 2.29 into von Kármán equation Eq. 2.24, we get

$$\frac{c_f}{2} = \frac{7}{72}\frac{d\delta^*(x)}{dx^*} . \tag{2.30}$$

From Eq. 2.27 and 2.30, by integrating,

$$\delta^*(x) = 0.38 \left(\frac{U_\infty^* x^*}{\nu^*}\right)^{-1/5} x^* = 0.38 Re_x^{-1/5} x^* \; (Re_x < 10^7) . \tag{2.31}$$

From Eq. 2.24, the global friction $D(l)$ is expressed as

$$\begin{aligned} D(l)^* &= b^* \int_0^{l^*} \tau_w(x)^* \, dx^* \\ &= b^* \rho^* U_\infty^{*2} \int_0^{l^*} d\theta^* \\ &= b^* \rho^* U_\infty^{*2} \theta^*(l^*) . \end{aligned} \tag{2.32}$$

Substituting Eq. 2.29 and 2.31 into Eq. 2.32, we get

$$\begin{aligned} D(l)^* &= 0.036 \rho^* U_\infty^{*2} b^* l^* \left(\frac{U_\infty^* l^*}{\nu^*}\right)^{-1/5} \\ &= 0.036 \rho^* U_\infty^{*2} b^* l^* Re_l^{-1/5} \; (5 \times 10^5 < Re_l < 10^7) . \end{aligned} \tag{2.33}$$

By using equations above, the global friction coefficient and friction coefficient are expressed as

$$C_f = 0.072 Re_l^{-1/5} \; (5\times10^5 < Re_l < 10^7)\;, \tag{2.34}$$

$$c_f(x) = 0.059 Re_x^{-1/5} \; (Re_x < 10^7)\;. \tag{2.35}$$

As a deferent empirical relationship between a friction coefficient and a Reynolds number, Schoenherr (1932) suggested introduced following equation based on the power-law;

$$c_f \approx 0.31 \left[\ln^2(2Re_\theta) + 2\ln(2Re_\theta)\right]^{-1}\;. \tag{2.36}$$

Moreover, the relation between the Reynolds numbers are expressed as following, [1]

$$Re_\delta = 0.38\; Re_x^{4/5}\;, \tag{2.37}$$

$$Re_\tau = 0.041\; Re_\delta^{-1/4}\;. \tag{2.38}$$

2.7 Physical decomposition of skin friction drag

Fukagata et al. (2002a) found an identity which decomposes the skin friction drag into four different physical contributions. In the fully developed simple internal flow such as turbulent channel flows or pipe flows, the terms are only two terms, viz., laminar contribution and turbulence contributions. For instance, in fully developed channel flows, it is lead from following time-averaged Navier-Stokes equation of fully developed turbulent channel flow,

$$0 = -\frac{\partial P}{\partial x} - \frac{\partial \overline{u'v'}}{\partial y} + \frac{1}{Re_b}\frac{\partial^2 U}{\partial y \partial y}\;, \tag{2.39}$$

where Re_b denote a bulk Reynolds number defined as

$$Re_b = \frac{2U_b^* \delta_h^*}{\nu^*} \tag{2.40}$$

[1] It is assumed that the region of laminar boundary layer at upstream is much shorter than the region of turbulent one.

where Re_b is the Reynolds number consisted of a doubled bulk streamwise mean velocity, u_b^*, the half width of the channel, δ_h and kinematic viscosity. Here, (a) constant flow rate, (b) homogeneity in the streamwise and spanwise direction, (c) symmetry with respect to the center plane, and (d) no slip condition condition on the wall are assumed. By integrating Eq. 2.39 in wall-normal direction from the bottom wall to the center, following relation is obtained,

$$-\frac{\partial P}{\partial x} = \frac{1}{8} C_f \tag{2.41}$$

and the skin friction coefficient here is defined as

$$C_f = \frac{\tau_w^*}{\frac{1}{2}\rho^* U_b^{*2}} = \frac{8}{Re_b} \left. \frac{dU}{dy} \right|_{y=0} . \tag{2.42}$$

By substituting Eq. 2.41 into Eq. 2.39,

$$\frac{1}{8} C_f = \frac{\partial}{\partial y} \left(\overline{u'v'} - \frac{1}{Re_b} \frac{\partial U}{\partial y} \right) . \tag{2.43}$$

By applying triple integration, $\int_0^1 dy \int_0^y dy \int_0^y dy$ to Eq. 2.43 and using the definition of the bulk mean velocity, $\int_0^1 U dy = 1/2$, following equation is obtained,

$$\frac{1}{2} = Re_b \left[\frac{C_f}{24} - \int_0^1 (1-y)(-\overline{u'v'}) \right] , \tag{2.44}$$

or, equivalently,

$$C_f = \frac{12}{Re_b} + 12 \int_0^2 2(1-y)(-\overline{u'v'}) \, dy . \tag{2.45}$$

The one important feather that FIK identity does not contain the terms involving spatially development, viz., only from Reynolds shear stress.

For incompressible spatially developing turbulent boundary layer, the beginning equation is mean boundary layer equation as

$$0 = -\frac{\partial P}{\partial x} - \frac{\partial UU}{\partial x} - \frac{\partial UV}{\partial y} - \frac{\partial \overline{u'u'}}{\partial x} - \frac{\partial \overline{u'v'}}{\partial y} + \frac{1}{Re} \frac{\partial^2 U}{\partial x \partial x} + \frac{1}{Re} \frac{\partial^2 U}{\partial y \partial y} . \tag{2.46}$$

Here, (a) constant free-stream velocity, (b) homogeneity in the spanwise direction, (c) $\partial U/\partial y = 0$ at $y = 1$, and (d) $u = w = 0$ on the wall are assumed.

By applying triple integration, following identity is obtained,

$$c_f(x) = \underbrace{\frac{4(1-\delta_d)}{Re_\delta}}_{c^\delta(x)} \underbrace{+4\int_0^1 (1-y)(-\overline{uv})\ dy}_{c^T(x)}$$
$$\underbrace{+4\int_0^1 (1-y)(-UV)\ dy}_{c^C(x)} \underbrace{-2\int_0^1 (1-y)^2 \left(\frac{\partial UU}{\partial x} - \frac{1}{Re_\delta}\frac{\partial^2 U}{\partial x \partial x}\right) dy}_{c^D(x)}, \tag{2.47}$$

The terms in the right hand side denote the contributions from the boundary layer thickness, the Reynolds shear stress, mean convection and spatially development, respectively. The character of these terms are following,

- Boundary layer thickness term, $c^\delta(x)$
  - The contribution from a volumetric rate in streamwise direction. Since c^δ is inversely proportional to the Reynolds number, this contribution becomes small as Reynolds number increases. In practical in present target such as airplane or trains, Reynolds number is quite high, so it can be omitted.
- Reynolds shear stress term, $c^T(x)$
  - The contribution from a Reynolds shear stress caused by the turbulent vortices near the wall. In previous investigation of the friction drag reduction in internal flow, this term is targeted to reduce the friction drag.
- Mean convection, $c^C(x)$
  - The contribution from a mean convection of the streamwise momentum to wall-normal direction. Since both of mean streamwise velocity, U, and wall-normal velocity, V, are positive in plane boundary layer, the production of these callosity components are positive. Therefore this term works as reducing factor of the skin friction drag, while other terms work as enhancing factors.
- Spatial development, $c^D(x)$

– The contribution from a spatially development. All terms own the differentiation in streamwise direction. Since the boundary layer grows proportionally to $Re_x^{4/5}$ in turbulent boundary layer, a variation in streamwise direction of boundary layer becomes small. Therefore, Spatial development term can be omitted in high Reynolds number flow.

2.8 Control efficiency

The drag reduction rate of the friction draft reduction control, R, is calculated as

$$R = \frac{C_{f,nc} - C_{f,ctr}}{C_{f,nc}}\,, \tag{2.48}$$

where $C_{f,nc}$ and $C_f f, ctr$ demote the global friction coefficient calculated as

$$C_f = \frac{1}{L_{ctr}} \int_0^{L_{ctr}} c_f(x)\, dx. \tag{2.49}$$

In practical applications, however, it is not enough to consider only the level of friction drag reduction. One must also consider the efficiency of control. Considering only an ideal control input (viz., neglecting any mechanical energy loss in actuators/sensors), the drag reduction rate, R, gain, G, and net energy saving rate, S can be defined as (see Kasagi et al., 2009a)

$$R = \frac{W_0 - W}{W_0}, \tag{2.50}$$

$$G = \frac{W_0 - W}{W_{in}}, \tag{2.51}$$

and

$$S = \frac{W_0 - (W + W_{in})}{W_0}, \tag{2.52}$$

where W_0 and W are the pumping powers in the uncontrolled and controlled cases, respectively and W_{in} denotes the power of the (ideal) control input. A schematic of the relationship between R and S is illustrated in figure 2.3.

For the channel flow or pipe flow, the flow is driven by the streamwise pressure gradient. In the STBL, the free stream velocity is constant and net skin friction drag on the wall is equivalent to the drive force of the flow; it is easy to imagine that the moving plate in the flow against the skin friction drag. Fukagata et al. (2009) presented the mathematical definition of the driving force of the flow, W_p and input power of the actuators W_a. In the STBL, the driving force of the flow is calculated as

$$W_p^* = \int_{S^*} \tau_w^* \, dS^* \,, \tag{2.53}$$

where A denotes the area where the control input is applied. Moreover, input power of the actuators are expressed as

$$W_a^* = \int_S^* \left[\frac{1}{2}\overline{\phi^{*3}} + \overline{p'^*\phi^*} + \nu^*(\nabla^* \cdot \mathbf{n})\overline{\phi^{*2}} \right] dS^* + \int_{V^*} \overline{\mathbf{u}^* \cdot \mathbf{b}^*} \, dV^* \,, \tag{2.54}$$

where ϕ, $\mathbf{b}$ denote, blowing/suction velocity on the wall and body force applied in the flow, respectively.

For the uniform blowing/suction case, Eqs. 2.54 is reduced to

$$W_a^* = \int_{S^*} \frac{1}{2} \overline{V_w^{*3}} \, dS^* \,, \tag{2.55}$$

where V_w denotes wall-normal velocity on the wall. The input power of the buoyant force is calculated from the second term in the right hand side of Eq. 2.54. However, since the buoyancy is driven by the thermal gradient on the wall, the input power of the uniform heating/cooling is calculated as

$$W_a^* = \int_{S^*} \lambda^* \left. \frac{\partial T^*}{\partial y^*} \right|_w dS^*. \tag{2.56}$$

2.9 Visualization of the vortices

To visualize the vortex structure in the flow field, the 2nd invariant of deformation tensor, Q, is introduced. The incompressible Navier-Stokes equation is arranged to

$$-\frac{1}{\rho^*}\frac{\partial p^*}{\partial x_i^*} = u_j^* \frac{\partial u_i^*}{\partial x_j^*} - \nu^* \frac{\partial^2 u_i^*}{\partial x_j^* \partial x_j^*} \,. \tag{2.57}$$

Taking a divergence of the incompressible Navier-Stokes equation by $\frac{\partial^*}{\partial x_i^*}$, we get

$$-\frac{1}{\rho^*}\frac{\partial}{\partial x_i^*}\left(\frac{\partial p^*}{\partial x_i^*}\right) = \frac{\partial}{\partial x_i}\left(u_j^* \frac{\partial u_i^*}{\partial x_j^*}\right) - \frac{\partial}{\partial x_i}\left(\nu^* \frac{\partial^2 u_i^*}{\partial x_j^* \partial x_j^*}\right) \,. \tag{2.58}$$

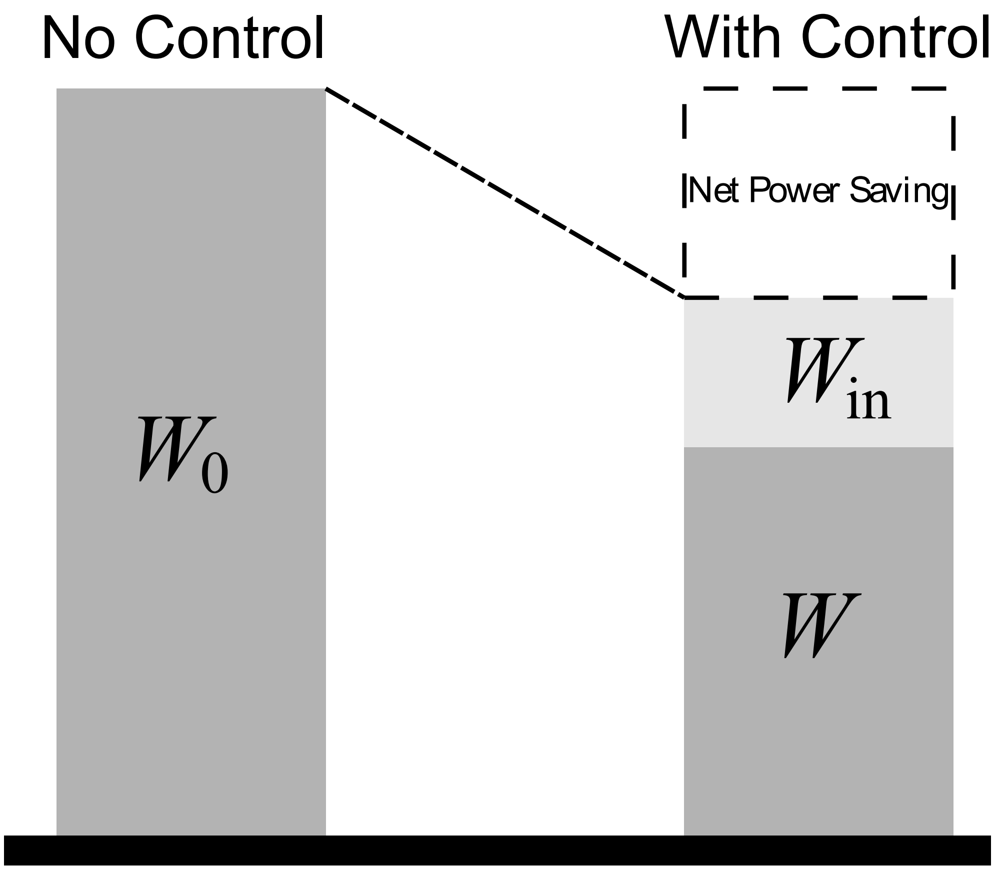

Figure 2.3: Efficiency

By using continuity equation, we can obtain

$$-\frac{1}{\rho^*}\frac{\partial^2 p^*}{\partial x_i^* \partial x_i^*} x_i^* = \frac{\partial u_i^*}{\partial x_j^*}\frac{\partial u_j^*}{\partial x_i^*} = Q^* \ . \tag{2.59}$$

In present study, an iso-surface of the Laplacian of pressure is used for visualization of the vortex structures.

Chapter 3

Direct numerical simulation of incompressible turbulent boundary layer

A direct numerical simulation of the low Reynolds number STBL is performed here. Low Reynolds number indicates comparably viscous-dominant turbulent flow. In this chapter, the details of numerical schemes are shown and the code is verified by comparing the present statistics with those of Wu and Moin (2009).

3.1 Numerical procedure

The governing equations of a fluid motion in Chap. 2 (Eqs. 2.6−2.8) are used for the direct numerical simulation of STBL. The non-dimensionalized governing equations are incompressible continuity, Navier-Stokes and energy equations as follows;

$$\frac{\partial u_i}{\partial x_i} = 0, \tag{3.1}$$

$$\frac{\partial u_i}{\partial t} = -\frac{\partial u_i u_j}{\partial x_j} - \frac{\partial p}{\partial x_i} + \frac{1}{Re}\frac{\partial^2 u_j}{\partial x_j \partial x_j} + f_i\ , \tag{3.2}$$

$$\frac{\partial T}{\partial t} = -\frac{\partial T u_i}{\partial x_i} + \frac{1}{Re\ Pr}\frac{\partial^2 T}{\partial x_i \partial x_i}. \tag{3.3}$$

All variables are non-dimensionalized by the free-stream velocity U_∞^* and the 99% boundary layer thickness at the inlet of the computational domain δ_0^*. The Reynolds

Table 3.1: Speficication of the DNS code

Time integration	Low storage 3rd order RK scheme
Advection term	Energy conservative second order finite difference method
Diffusion term	Second order Crank-Nikolson method
Poisson solver for pressure	homogeneous direction: fast Foulier transform
	wall-normal direction: tridiagonal matrix solver
Coupling method for velocity and pressure	SMAC

number is defined as $Re = U_\infty^* \delta_0^* / \nu^*$, where ν^* is the kinematic viscosity.

The direct numerical simulation code is based on a channel flow code developed by Fukagata et al. (2006), which was itself adapted from a pipe flow code (Fukagata et al., 2002a). The spatial discretization uses the energy-conservative second-order finite difference scheme (e.g., Ham et al., 2002). The time integration uses the low-storage third-order Runge-Kutta/Crank-Nicolson scheme (e.g., Spalart et al., 1991). The scheme adapted to present code is listed in Table 3.1. The flow chat of the present code is shown in Fig. 3.1.

3.1.1 Spatial descretizations

The staggered grid is used for the present code. The relationship between velocities and pressure is shown in Fig. 3.2. The velocities and there pressure are defined at the cell surface and the cell center, respectively. The first and second derivatives are discretized, e.g., as

$$\left[\frac{\delta v}{\delta y}\right]_{i,j,k} = \frac{v_{i,j+1/2,k} - v_{i,j+1/2,k}}{\Delta y_j}, \tag{3.4}$$

$$\left[\frac{\delta^2 v}{\delta y \delta y}\right]_{i,j+1/2,k} = \frac{1}{\Delta y_{j+1/2}} \left(\frac{v_{i,j+3/2,k} - v_{i,j+1/2,k}}{\Delta y_{j+1}} - \frac{v_{i,j+1/2,k} - v_{i,j-1/2,k}}{\Delta y_{j+1}} \right), \tag{3.5}$$

where the subscripts i, j, and k denote the stencils in x, y, z directions, respectively. The external force is denoted by f. These advection terms are discretized by the second-order energy conservative FDM (Bewley, 1999; Ham et al., 2002; Kajishima, 1999a).

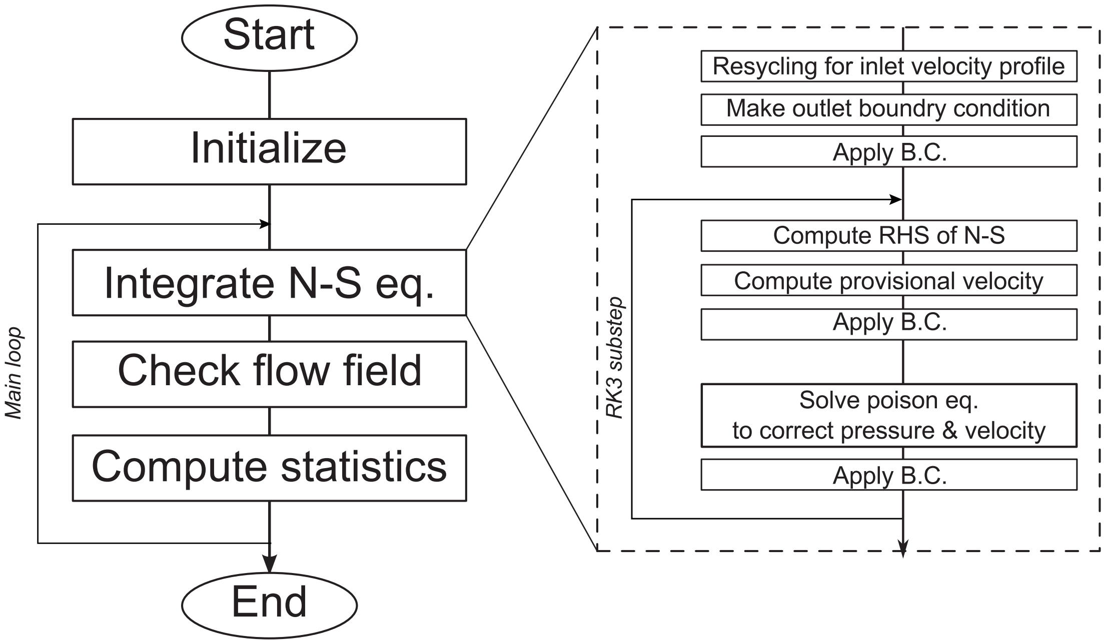

Figure 3.1: Flow chart of the present simulation.

The continuity and Navier-Stokes equations are expressed as

$$\frac{\delta u_n}{\delta x_n} = 0, \tag{3.6}$$

$$\frac{\delta u_n}{\delta t} = -\frac{\delta \{u_k\}^{x_n} \overline{u_n}^{x_n}}{\delta x_k} - \frac{\delta p}{\delta x_n} + \frac{1}{Re}\frac{\delta^2 u_n}{\delta x_k\, \delta x_k}, \tag{3.7}$$

where $\bar{\cdot}$ and $\{\cdot\}$ demote the arithmetic and volume-flux averages (Kajishima, 1999a), respectively which are calculated as

$$\overline{u}^{y}_{i+1/2,j+1/2,k} = \frac{u_{i+1/2,j,k} - u_{i-1/2,j,k}}{2}, \tag{3.8}$$

$$\{u\}^{x}_{i+1,j,k} = \frac{u_{i+1/2,j,k} - u_{i-1/2,j,k}}{2}, \tag{3.9}$$

$$\{u\}^{y}_{i+1/2,j+1/2,k} = \frac{\Delta y_{j+1} u_{i+1/2,j+1,k} - \Delta y_j u_{i+1/2,j,k}}{\Delta y_{j+1} + \Delta y_j}, \tag{3.10}$$

where superscripts (x, y, z) denote the direction of interpolation.

The low-Storage 3rd-order Runge-Kutta/Crank-Nikolson scheme uses for the time integration (Dukowicz and Dvinsky, 1992). The discretized continuity and Navier-

Stokes equations are expressed as following by using differential operators as

$$\vec{\mathcal{D}} \cdot \vec{u} = 0, \tag{3.11}$$

$$\frac{\partial \vec{u}}{\partial t} = \vec{f} - \vec{\mathcal{D}} p + \frac{1}{Re} \vec{\mathcal{L}} \vec{u}, \tag{3.12}$$

where the differential operators denotes

$$\vec{u} = \begin{pmatrix} u \\ v \\ w \end{pmatrix}, \vec{f} = \begin{pmatrix} h_x \\ h_y \\ h_z \end{pmatrix}, \vec{\mathcal{D}} = \begin{pmatrix} \frac{\partial}{\partial x} \\ \frac{\partial}{\partial y} \\ \frac{\partial}{\partial z} \end{pmatrix}, \tag{3.13}$$

$$\vec{\mathcal{L}} = \frac{\partial}{\partial x} + \frac{\partial}{\partial y} + \frac{\partial}{\partial z}. \tag{3.14}$$

where, h_x, h_y, h_z denote advection terms of streamwise, wall-normal, and spanwise velocities, respectively.

The variables at next time-step, $\ell + 1$, is calculated as

$$\vec{u}^{\ell+1} = \vec{u}^{\ell} + \Delta t \left[\gamma^{\ell} \vec{f}^{\ell} + \zeta^{\ell} \vec{f}^{\ell-1} - \alpha^{\ell} \vec{\mathcal{D}} p^{\ell+1} + \alpha^{\ell} \frac{1}{Re} \frac{\mathcal{L}\vec{u}^{\ell} + \mathcal{L}\vec{u}^{\ell+1}}{2}. \right] \tag{3.15}$$

where γ^{ℓ}, ζ^{ℓ} and α^{ℓ} denotes the coefficient of the integration, described in Table 3.2. For the pressure, $p^{\ell+1}$ is unknown in this stage, i.e., the continuity equation is not satisfied. Satisfying the Poisson equations of the pressure, the velocity is modified as

$$\vec{u}^{*} = \vec{u}^{\ell} + \Delta t \left[\gamma^{\ell} \vec{f}^{\ell} + \zeta^{\ell} \vec{f}^{\ell-1} - \alpha^{\ell} \vec{\mathcal{D}} p^{\ell} + \alpha^{\ell} \frac{1}{Re} \frac{\mathcal{L}\vec{u}^{\ell} + \mathcal{L}\vec{u}^{*}}{2} \right]. \tag{3.16}$$

This is equivalent to

$$\vec{u}^{*} = \vec{u}^{\ell} + \Delta \vec{u}, \tag{3.17}$$

where

$$\Delta \vec{u} = \Delta t \left[\gamma^{\ell} \vec{f}^{\ell} + \zeta^{\ell} \vec{f}^{\ell-1} - \alpha^{\ell} \vec{\mathcal{D}} p^{\ell} + \alpha^{\ell} \frac{1}{Re} \left(\mathcal{L}\vec{u}^{\ell} + \frac{\mathcal{L}\Delta\vec{u}}{2} \right) \right]. \tag{3.18}$$

The modification of velocity is done as

$$\vec{u}^{\ell+1} = \vec{u}^{*} - \alpha^{\ell} \Delta t \vec{\mathcal{D}} \Phi, \tag{3.19}$$

Table 3.2: Integration coefficients for RK3/CN scheme.

substep, ℓ	1	2	3
γ	8/15	5/12	3/4
ζ	0	-17/60	-5/12
α	8/15	2/15	1/3

Table 3.3: Boundary conditions

	Velocities (DRV)	Pressure (DRV)	Velocities (CTR)	Pressure(CTR)
Inlet	Recycle method	NSCBC	Recycle method	NSCBC
Outlet	Convective	NSCBC	Convective	NSCBC
Upper	$\frac{\partial u}{\partial y} = \frac{\partial v}{\partial y} = 0,\, w = 0$	$\frac{\partial p}{\partial y} = 0$	u, v,: $\frac{\partial u}{\partial y} = \frac{\partial v}{\partial y} = 0,\, w = 0$	$\frac{\partial p}{\partial y} = 0$
Bottom	$u = v = w = 0$	$\frac{\partial p}{\partial y} = 0$	$u = w = 0,\ v = v_{ctr}$	$\frac{\partial p}{\partial y} = 0$

where

$$p^{\ell+1} - p^{\ell} = \Phi. \tag{3.20}$$

Due to above, the Poisson equation of the pressure,

$$\mathcal{L}\Phi = \frac{1}{\alpha^{\ell}\Delta t}\mathcal{D} \cdot \vec{u}^{*} \tag{3.21}$$

is satisfied.

The discretized advection term has been verified (Bewley, 1999; Ham et al., 2002; Kajishima, 1999a) to be momentum-and energy-conservative given that the discretized continuity equation is satisfied. Thus the discretized equation Eqs. (3.6) and (3.7) conserve not only the mass and momentum but also the total kinetic energy in the inviscid limits.

3.1.2 Time integration

The Crank-Nicolson scheme is applied only in wall-normal direction, y. This iteration is solved by the tridiagonal matrix algorithm (TDMA) method. The Fourier transfor-

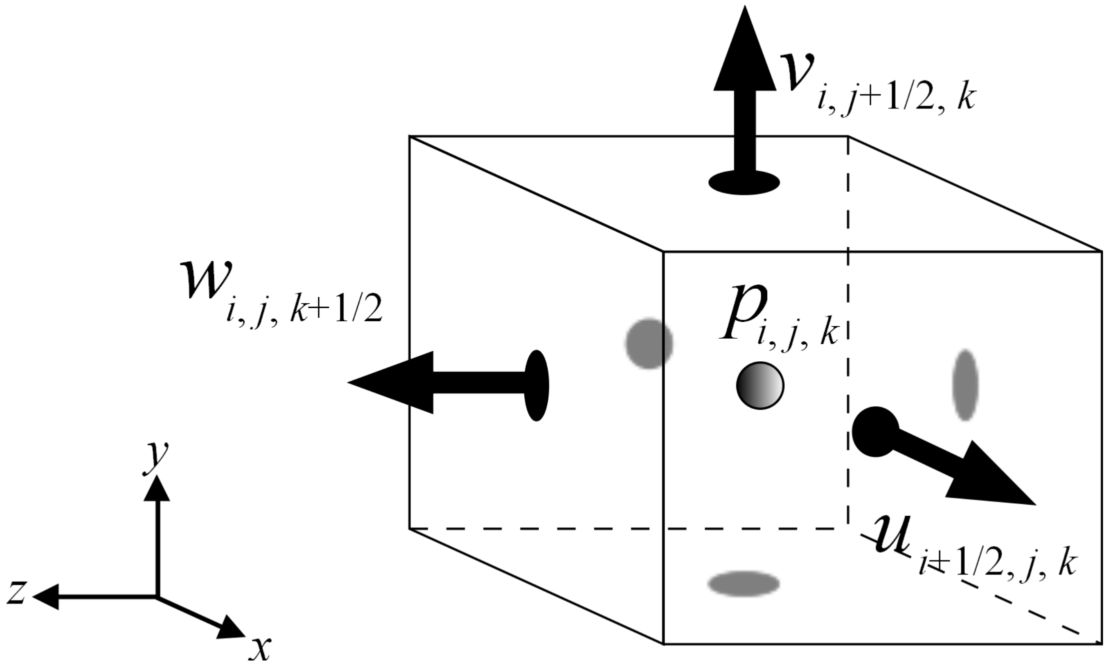

Figure 3.2: Computational grid: locations where the velocity components and the pressure are defined on the staggered grid system.

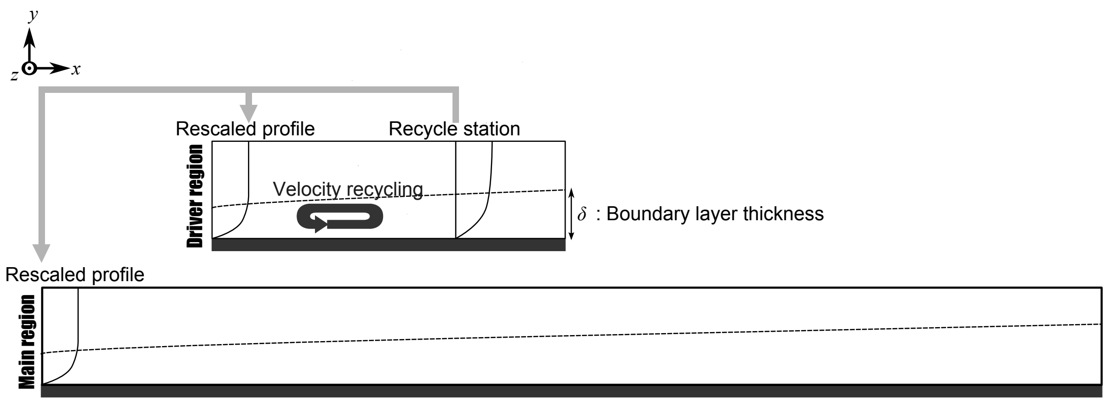

Figure 3.3: Computational geometry

mation is applied in streamwise and spanwise directions to solve the Poisson equation of the pressure and TDMA method is used in wall-normal direction.

The computational domain is composed of two regions: a driver region and a main region, as shown in Fig. 3.3. The recycle method of Lund et al. (1998) is used in the driver region to generate the inflow condition.

In both the driver and main regions, the upper boundary conditions for the streamwise velocity, u, the wall-normal velocity, v and the spanwise velocity, w, are set to be $\partial u/\partial y = \partial v/\partial y = 0$ and $w = 0$. On the wall, the no-slip condition is applied in the driver region, while in the main region uniform blowing or suction velocity $v = V_{ctr}$ is added.

The convective boundary condition is applied at the downstream end of each computational domain, i.e.,

$$\frac{\partial u_i}{\partial t} + \overline{u}(y)\frac{\partial u_i}{\partial x} = 0, \tag{3.22}$$

where $\bar{\cdot}$ denotes the average in the homogeneous (i.e., spanwise) direction. The pressures at the inlet and outlet boundaries are given by the Navier-Stokes characteristic boundary condition (NSCBC) of Miyauchi et al. (1996),

$$\frac{\partial p}{\partial t} + U_\infty \frac{\partial p}{\partial x} = \frac{1}{2Re}\omega_z^2, \tag{3.23}$$

where ω_z denotes the spanwise vorticity. It is known that this boundary condition considerably suppresses the unphysical pressure near the inlet and outlet that appears when an ordinary Neumann condition is used.

The streamwise, wall-normal and spanwise lengths of the driver and main regions are $(L_x^D, L_y^D, L_z^D) = (3\pi, 3, \pi)$ and $(L_x, L_y, L_z) = (9\pi, 3, \pi)$, respectively, where the superscript D denotes the driver region. The corresponding numbers of grid points are $(N_x^D, N_y^D, N_z^D) = (128, 96, 128)$ and $(N_x, N_y, N_z) = (512, 96, 128)$, respectively. The recycle station is located at $x^D = 2\pi$. In this study, the Reynolds number $Re = U_\infty^* \delta_0^* / \nu^*$ is set to be 3000, which corresponds to an inlet friction Reynolds number of $Re_{\tau 0} = u_\tau^* \delta_0^* / \nu^* \simeq 160$, where u_τ is the friction velocity. The grid spacing in the streamwise and spanwise directions (in wall units) are $\Delta x^{+0} = 8.83$ and $\Delta z^{+0} = 3.93$, respectively, where the superscript $^{+0}$ denotes the wall unit based on the friction velocity at the inlet of the main part. The minimum grid spacing in the wall-normal direction is $\Delta y^{+0} = 0.47$ and the maximum spacing is $\Delta y^{+0} = 6.67$.

The statistics are gathered over a time period of $T^{+0} \approx 4000$. The start of this time period is well after a statistical steady state has been reached.

3.1.3 Recycling method

For the DNS of the STBL, the inlet turbulent conditions of velocity components have to be made. The recycling method was introduced by Lund et al. (1998). The inlet data is made by rescaling the velocity profiles at the recycling station set at downstream. For the rescaling, first-order interpolation is used. The rescaling is done by decomposition each velocity component into an inner region and an outer region. Streamwise mean velocity profile are decomposed as

$$U^{\mathrm{inner}\,*} = u_\tau^*(x^*) f_1(y^+) \,, \tag{3.24}$$

$$U_\infty^* - U^{\mathrm{outer}\,*} = u_\tau^*(x^*) f_2(\eta) \,, \tag{3.25}$$

where $y^+ = u_\tau^* y^*/\nu^*$ and $\eta = y^*/\delta^*$. Denoting the inlet profiles and profiles at recycle station by subscript inlt and recy, respectively, the non-dimensionalized streamwise mean velocities on each position are

$$U_{\mathrm{inlt}}^{\mathrm{inner}} = \alpha U_{\mathrm{recy}}(y_{\mathrm{inlt}}^+) \tag{3.26}$$

$$U_{\mathrm{recy}}^{\mathrm{outer}} = \alpha U_{\mathrm{recy}}(\eta_{\mathrm{inlt}}) + (1-\alpha) U^\infty \,, \tag{3.27}$$

where α is calculated as

$$\alpha = \frac{u_{\tau,\mathrm{inlt}}}{u_{\tau,\mathrm{recy}}} \,. \tag{3.28}$$

The rescaling for wall-normal mean velocity is assumed to follow

$$V^{\mathrm{inner}*} = U_\infty^* f_3(y^+) \tag{3.29}$$

$$V^{\mathrm{outer}*} = U_\infty^* f_4(\eta). \tag{3.30}$$

The non-dimensionalized wall-normal mean velocity profile at the inlet and the recycle station is

$$V_{\mathrm{inlt}}^{\mathrm{inner}} = \alpha V_{\mathrm{recy}}(y_{\mathrm{inlt}}^+) \tag{3.31}$$

$$V_{\mathrm{recy}}^{\mathrm{outer}} = \alpha V_{\mathrm{recy}}(\eta_{\mathrm{inlt}}) \,. \tag{3.32}$$

The spanwise mean velocity profile is assume to be zero. Velocity fluctuation components are expressed by the function g_i and h_i as

$$(u_i'^*)^{\mathrm{inner}} = u_\tau^* g_i(x^*,\, y^+, z^*,\, t^*) \,, \tag{3.33}$$

$$(u_i'^*)^{\mathrm{outer}} = u_\tau^* h_i(x^*,\, \eta,\, z^*,\, t^*) \,, \tag{3.34}$$

where $i = 1,\ 2,\ 3$ denote the directions. These fluctuation components are rescaled as

$$(u_i)^{\text{inner}}_{\text{inlt}} = \alpha (u')_{\text{recy}}(y^+, z^*,\ t^*)\ , \tag{3.35}$$

$$(u_i)^{\text{outer}}_{\text{inlt}} = \alpha (u')_{\text{recy}}(\eta, z^*,\ t^*)\ , \tag{3.36}$$

The inner components and outer components are merged as

$$(u_i)_{\text{inlt}} = \left[(U_i)^{\text{inner}}_{\text{inlt}} + (u'_i)^{\text{inner}}_{\text{inlt}}\right][1 - W(\eta_{\text{inlt}})] + \left[(U_i)^{\text{outer}}_{\text{inlt}} + (u'_i)^{\text{outer}}_{\text{inlt}}\right] W(\eta_{\text{inlt}})\ , \tag{3.37}$$

where W denotes a weighting function defined as

$$W(\eta) = \frac{1}{2}\left\{1 + \tanh\left[\frac{a(\eta - b)}{(1-2b)\eta + b}\right] / \tanh(a)\right\}\ , \tag{3.38}$$

here, $a = 4$ and $b = 0.2$, respectively. In the computation, α is calculated by using the momentum thickness as following;

$$\alpha = \frac{u_{\tau,\text{inlt}}}{u_{\tau,\text{recy}}} = \left(\frac{\theta_{\text{inlt}}}{\theta_{\text{recy}}}\right)^{1/[2(n-1)]}\ ,\ n = 5. \tag{3.39}$$

3.2 Computational setup

The setup used for the present computation is listed in Table 3.4. The coding of the present code was done with Intel Fortran (Intel Corporation). The post-processing of the data from the computation is done with the application softwares: Matlab (MathWorks Inc.), Gnuplot 4.2 and Open DX 4.4.4.

3.3 Computation in a channel flow

For the verification of the present code, at first, DNS of turbulent channel flow with the present code was performed. The friction Reynolds number was set to be $Re_\tau = 180$. Figure 3.4 shows the streamwise velocity U. The profile collapse on the one from Moser et al. (1999) solved by a spectral method. The gap between the profiles and log-law-profile is supposed to be due to the low Reynolds number. Fig. 3.5 shows the shear stresses as the Reynolds shear stress (RSS) and the viscous shear stress. Total of the RSS and VSS agree with the theoretical linear equation of the shear stress. These results verified the present code. The statistics are calculated from the data in$0 \leq T^+ \leq 2000$.

Table 3.4: Computational setup

Manufacturer	User's Side
CPU	Core i7-950 3.0GHz
Number of core	4
Memory	8GB
Operation system	Debian 2.6.26-2-amd64
Fortran version	ifort 11.1
Post processing	Matlab 2010 (MathWorks Inc.), Gnuplot 4.2, Open DX 4.4.4

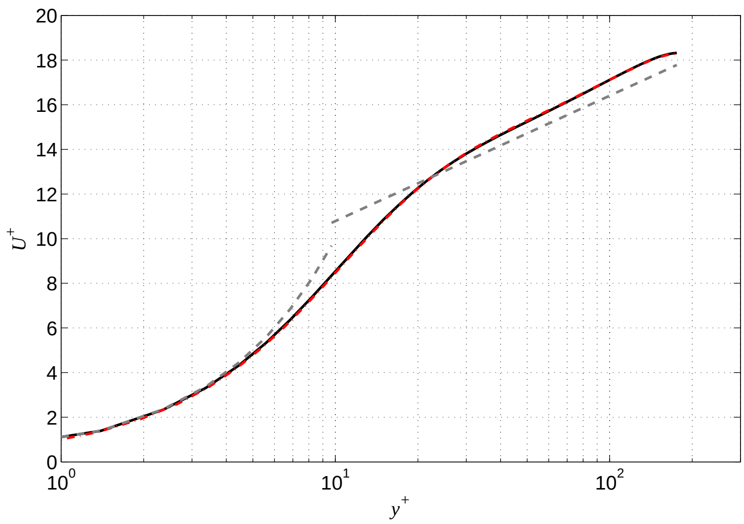

Figure 3.4: Mean streamwise velocity in the channel flow. Black, simulation in this paper; red, Moser et al. (1999) with a spectral method; gray chain lines, linear-law and log-law.

3.4 Base flow computation

The spatial development of the boundary layer is presented in Fig. 3.6. Fig. 3.6(a) shows the spatial development of the momentum thickness Reynolds number $Re_\theta = U^*_\infty \theta * / \nu^*$; the displacement thickness $Re_d = U^*_\infty \delta^*_d / \nu^*$, and the shape factor H in the uncontrolled turbulent boundary layer. The momentum thickness and the displacement thickness are both developing in the downstream direction. Moreover, a negative gra-

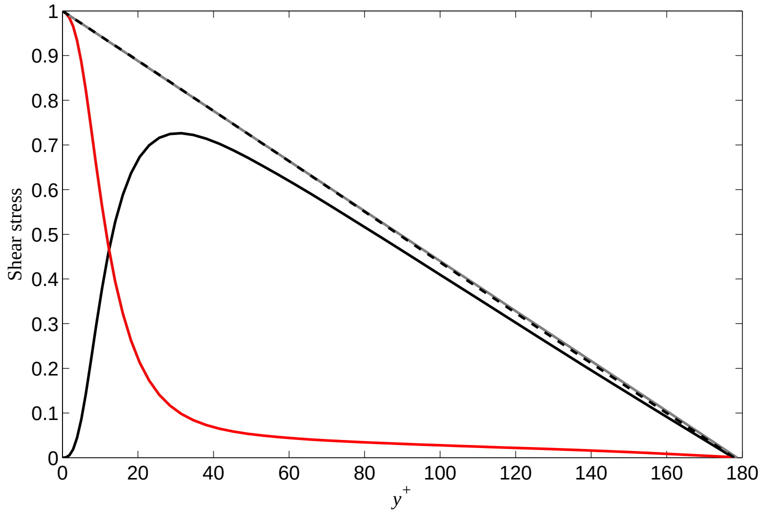

Figure 3.5: Sear stress in the channel flow. Black solid , Reynolds shear stress (RSS); red solid, viscous shear stress (VSS); black chain, RSS + VSS; gray solid, $\tau^+ = 1 - y^+/Re_\tau$

dient of for the shape factor indicates that the momentum toward the wall due to the turbulent transport increases as the Reynolds number increases. The boundary layer thickness develops from δ_0^* at the inlet to about $1.5\delta_0^*$ at the downstream end. The development of the local skin friction coefficient, $c_f = 2\tau_w^*/\rho^* U_\infty^{*2}$, is presented in Fig. 3.6(b) as a function of Re_θ. A slight deviation from the power law-based formula (Schoenherr 1932),

$$c_f \approx 0.31 \left[\ln^2(2Re_\theta) + 2\ln(2Re_\theta)\right]^{-1}, \tag{3.40}$$

is found, and this is likely due to the low Reynolds number. A similar deviation has also been reported in Kong et al. (2006).

The velocity statistics at several streamwise locations are presented in Fig. 3.7. Fig. 3.7(a) shows the mean velocity profile at $Re_\theta = 530$ and 700. In the regions near the wall, the profile is in reasonable agreement with the DNS result of Wu and Moin (2009) at $Re_\theta = 700$. Fig. 3.7(b) shows the root-mean-square (RMS) velocity fluctuation. The strongest fluctuation appears in the streamwise component u_{rms}. The peak of u_{rms} is found at $y^+ \approx 15$ regardless of the Reynolds number within the present Reynolds number range. The peaks of v_{rms} and w_{rms} are found to shift away from the

(a)

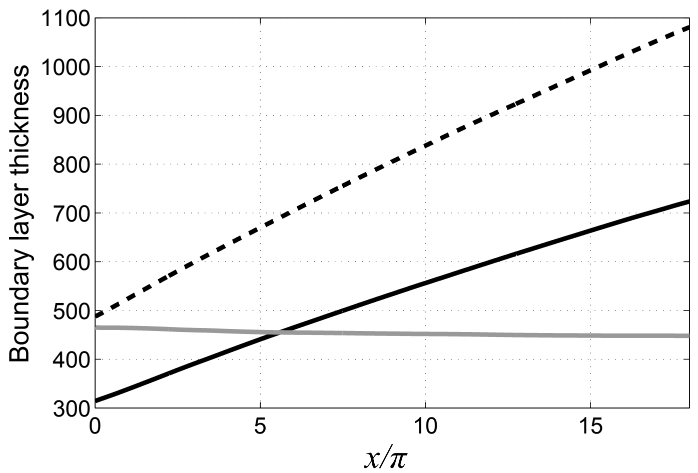

(b)

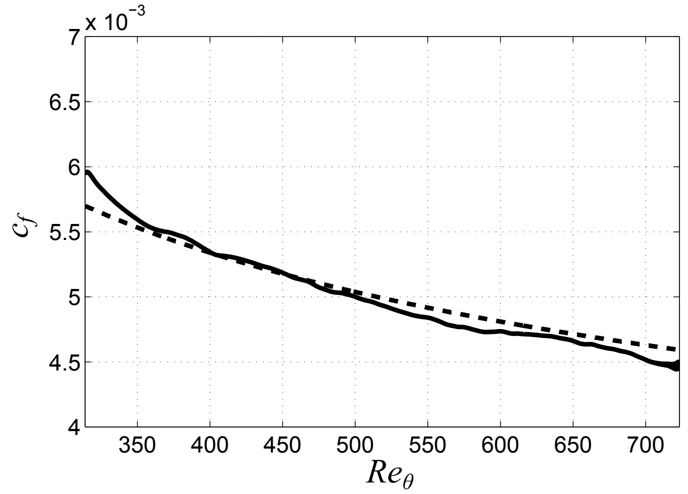

Figure 3.6: Spatial development of the boundary layer. (a) Boundary layer thickness and shape factor as a function of x: solid black line, Re_θ; dashed black line, Re_{δ_d}; solid gray line, shape factor $300H$. (b) Local friction coefficient c_f: solid line, c_f computed from wall shear stress; dashed line, c_f of empirical formula.

wall as the Reynolds number increases. The viscous shear stress (VSS) $\partial U^*/\partial y^*$ and the Reynolds shear stress (RSS) $-\overline{u'v'}^*$ are shown in Fig. 3.7(c). As the Reynolds number increases, the peak value of RSS becomes larger and the location of the peak shifts away from the wall, while there is almost no difference in the VSS profiles.

Some difference can be found between the present results and those of Wu and

Moin (2009). Namely, U, u_{rms} and $-\overline{u'v'}$ are slightly larger in the present simulation. These differences may be attributed to the difference in the upstream conditions. The recycle method is used in the present simulation, which assumes a fully developed turbulence. In Wu & Moin (2009), in contrast, a transition from laminar boundary layer is reproduced, due to which the flow at this Re_θ appears still transitional. In addition, the difference may also be attributed to the difference in the grid resolution: $\Delta x^{+0} = 8.83$ and $\Delta z^{+0} = 3.93$ in the present simulation, while $\Delta x^{+0} = 5.91$ and $\Delta z^{+0} = 11.13$ in Wu and Moin (2009). It is known that low resolution in the spanwise direction causes an underestimation of redistribution from u' to v' and w' components (Kajishima 2003).

There are two major differences between the present and Wu and Moin (2009)'s simulations, which might have caused the difference in the statistics at $Re_\theta = 700$: the upstream condition and the resolution in the spanwise direction. As for the upstream condition, Wu and Moin (2009) reproduce the transition in the upstream region, while the present study adopts the recycle method assuming a fully-developed turbulence. The friction coefficient shown in Fig. 3.8 suggests that Wu and Moin (2009)'s flow is under transitional regime in the Re_θ range considered in our simulation (i.e., up to $Re_\theta = 700$). The dependency on the spanwise resolution has also been examined. The turbulent intensity at $\Delta z^{+0} = 4$ (fine grid used in the present simulation) and 16 (coarse grid) shown in Fig. 3.9 cleary indicates that u_{rms} increases and v_{rms} and w_{rms} decrease as the spanwise grid becomes coarser. Considering the two differences above, it can be easily understood that the present results with $\Delta z^{+0} = 16$ agree better with Wu and Moin (2009)'s at $Re_\theta = 800$ (at which the flow is considered to be fully developed). There are still some differences in the region away from the wall, which might be due to the artificial techniques used in both methods and the difference in the wall-normal extent of the computational domain.

(a)

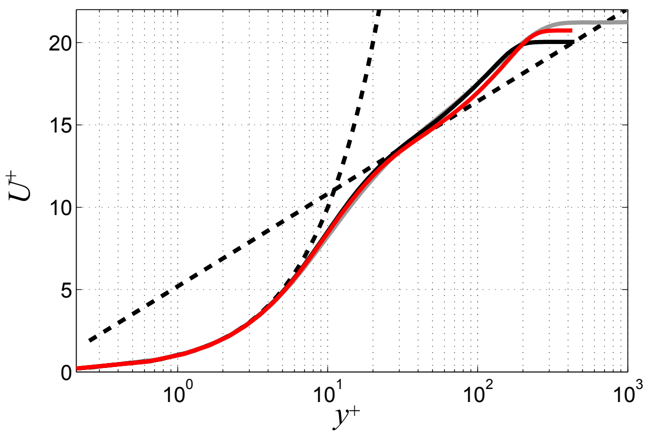

(b)

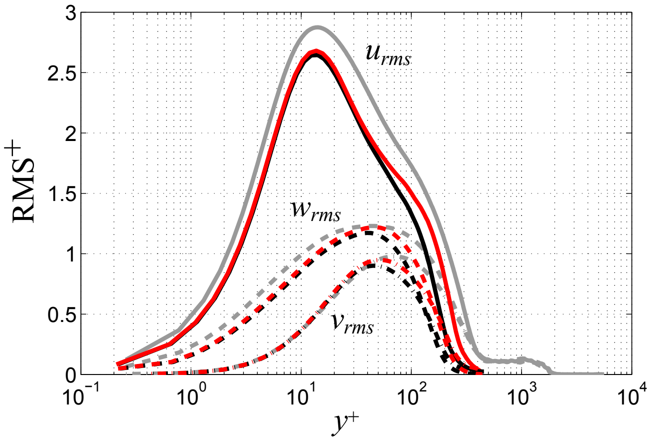

(c)

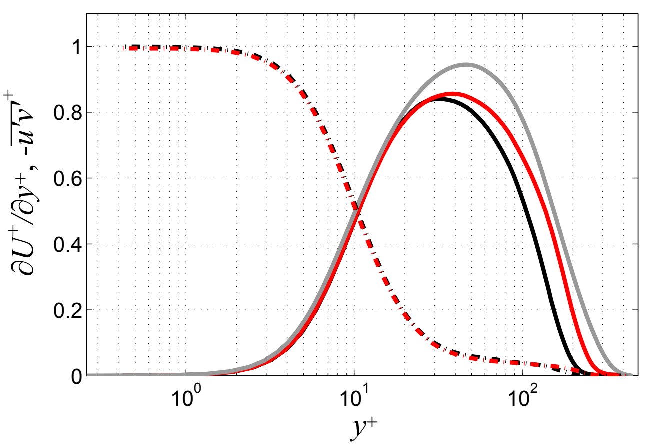

Figure 3.7: Base flow statistics: black lines, $Re_\theta = 530$; red lines, $Re_\theta = 700$; gray lines, Wu and Moin (2009) at $Re_\theta = 700$. (a) Mean streamwise velocity, U (dashed lines represent the law of the wall). (b) Turbulent intensities: solid, u_{rms}; dashed, v_{rms}; chain, w_{rms}. (c) Shear stresses: solid, Reynolds shear stress; dashed viscous shear stress.

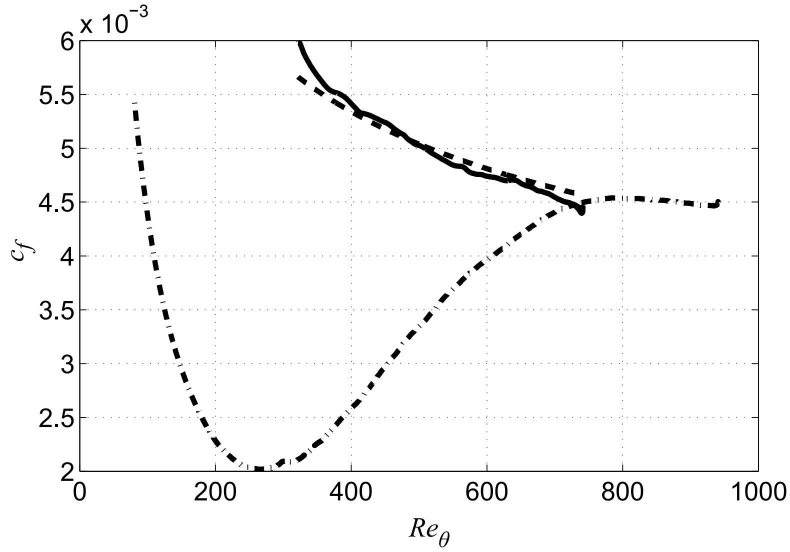

Figure 3.8: Friction coefficient in whole computational domain: Solid line, simulation in this paper; dashed line, empirical formula from momentum thickness in this paper; chain line, Wu and Moin (2009).

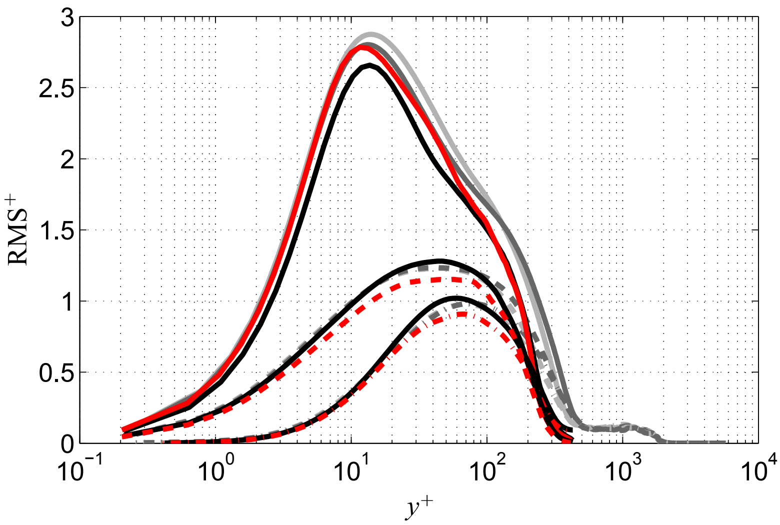

Figure 3.9: Turbulent intensities: black, $Re_\theta = 700$ (present); red, $Re_\theta = 700$ (coarse); light gray, $Re_\theta = 700$ (Wu and Moin, 2009); dark gray, $Re_\theta = 800$ (Wu and Moin, 2009). Solid, u_{rms}; dashed, v_{rms}; chain, w_{rms}.

Chapter 4

Uniform blowing/suction

The direct numerical simulation of the STBL with uniform blowing or suction aiming at skin friction drag reduction is performed. As mentioned in §1.2.5.1, it was confirmed that uniform blowing can reduce the friction drag in the channel flow. Moreover, the uniform suction works for suppress the turbulent transition, viz., the Reynolds shear stress can be reduced.

4.1 Uniform blowing

The uniform blowing or suction is applied by constant wall-normal velocity on the wall, V_w, in the control part of the computational domains. In the present study, the magnitude of uniform blowing (UB) or suction (US) is set to be 0.1%, 0.5%, or 1.0% of free-stream velocity. A transition zone is placed at $0 \leq x \leq \pi$, in which the control amplitude is gradually increased by using a hyperbolic tangent function as shown in Fig. 4.1.

4.2 Result

[t]

The effect of UB/US on the spatial development is presented in Fig. 4.2. It is found from the development of momentum thickness in Fig. 4.2(a) that UB thickens the boundary layer, while US thins it. The magnitude of both effects depends on the

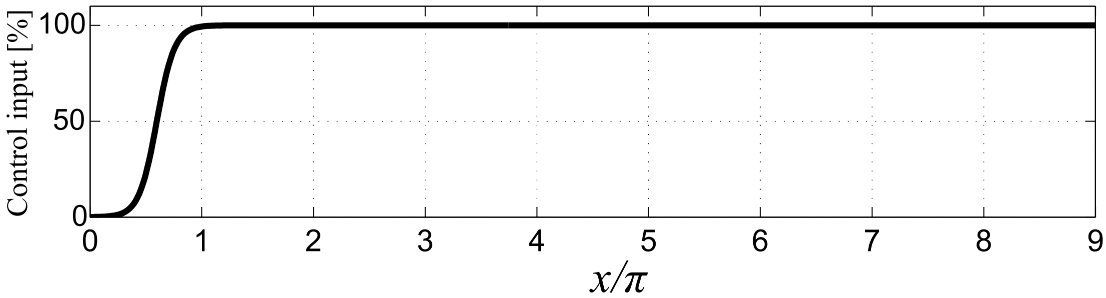

Figure 4.1: Control input profile

amplitude of UB/US. The shape factor H shown in Fig. 4.2(b) indicates that UB increases H and US decreases it. The large shape factor, H, indicates the flow separation. In the turbulent wall bounded flow such as diffusers, the flow separation can occur by an adverse pressure gradient at

$$H \approx 2.4\ . \tag{4.1}$$

in the turbulent boundary layer (White, 2005). From Fig. 4.2 (b), the blowing at 1% of free-stream velocity dramatically increases the shape factor. At the end of the computational domain, H still has positive gradient. This means that the strong blowing increase the possibility of the flow separation in the practical application with curved surfaces. It may causes an increases of the pressure drag.

The uniform blowing (suction) works to push (pull) the mean velocity profile away from (toward) the wall, leading to the effects observed above as if the Reynolds number is increased by UB and decreased by US. An interesting observation in the UB case is that the shape factor increases in the downstream region, since the shape factor usually decreases as the Reynolds number increases.

The local friction coefficient c_f shown in Fig. 4.2(c) clearly indicates that UB reduces the friction drag, while US enhances it. This is basically due to the modification of the mean velocity profile as shown in Fig. 4.3(a); it is shifted away from the wall by UB, but shifted toward the wall by US. Note that the quantities shown in Fig. 4.3 are non-dimensionalized by the local friction velocity of the uncontrolled flow at the same streamwise position (denoted by the superscript $+nc$). Profiles of the viscous and Reynolds shear stresses shown in Fig. 4.3(b) indicate that UB (US) reduces (enhances)

(a)

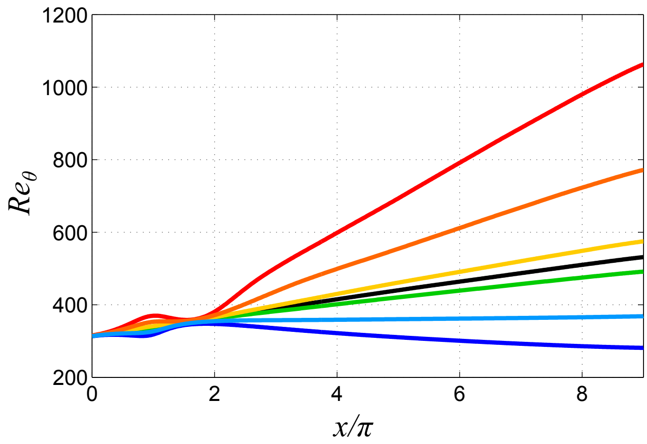

(b)

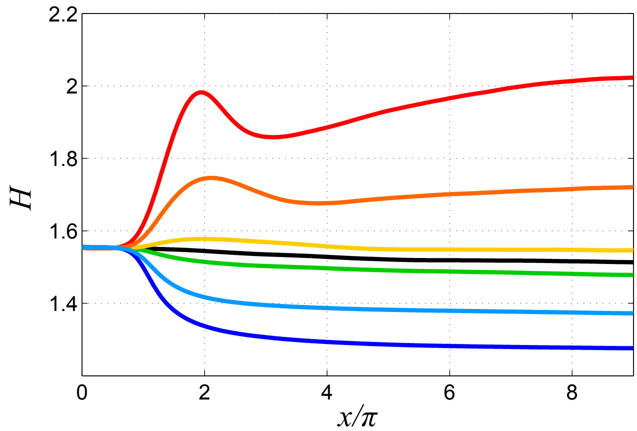

(c)

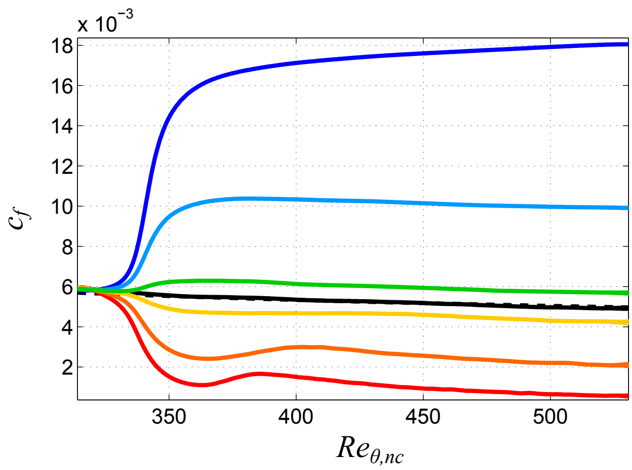

Figure 4.2: Effect of UB/US on spatial development of the boundary layer: black, no control; yellow, 0.1% UB; orange, 0.5% UB; red, 1% UB; green, 0.1% US; light blue, 0.5% US; blue, 1% US. (a) Momentum thickness Re_θ. (b) Shape factor H. (c) Local friction coefficient.

the viscous shear stress, but enhances (reduces) the Reynolds shear stress. This opposite effect, which is counterintuitive, is similar to that observed in a channel flow with UB on one wall and US on the other wall (Sumitani and Kasagi, 1995).

Here, the global skin friction drag coefficients, C_f, is defined as

$$C_f = \frac{1}{L_{ctr}} \int_0^{L_{ctr}} c_f \, dx. \tag{4.2}$$

The drag reduction rate, R, as introduced in §2.8 is expressed by using the global friction coefficients as

$$R = \frac{C_{f,nc} - C_{f,ctr}}{C_{f,nc}}, \tag{4.3}$$

where $C_{f,nc}$, $C_{f,ctr}$ and L_{ctr} denote the friction coefficients of the flow with and without blowing/suction and the streamwise length of the computational domain, respectively. Figure 4.4 shows the drag reduction rate, R, as a function of wall-normal velocity applied on the wall, V_{ctr}. It is found that increasing the amplitude of uniform blowing or suction results in larger drag reduction or drag augmentation, respectively. In addition, the relationship between the drag reduction rate, R, and the control amplitude is found to be nonlinear.

The instantaneous flow structures are shown in Fig. 4.5 by the the second invariant of the deformation tensor Q^{+0} and the wall shear stress τ_w^{+0}. Compared to the uncontrolled case, vortices are enhanced in the UB case in spite of the reduced wall shear stress, while in the US case vortices are suppressed despite the increase of wall shear stress.

4.3 Discussion

4.3.1 Analysis using the FIK identity

In order to quantitatively investigate different dynamical effects of UB/US on the friction drag, the local friction coefficient c_f is decomposed into four different dynamical components as defined in Eq. (2.48). Each component computed from the statistics is shown in Fig. 5.16. In the upstream region, some discrepancy is found between c_f directly computed from the wall shear (dashed line) and that using Eq. (2.48) (black solid line), especially in the UB and US cases. This may be due to the non-zero mean pressure gradient caused by the sudden application of blowing/suction, while the mean pressure gradient is assumed to be zero in the derivation of Eq. (2.48): in fact such non-zero pressure gradient is observed in the statistics. In the following, a discussion is made of the downstream (i.e., fully-developed) region where this discrepancy is reasonably small.

In spatially developing boundary layers, some terms in the FIK identity act to increase friction drag, while others act reduce it. In the base flow (Fig. 5.16a), the contributions from the Reynolds stress (c^T) and the streamwise development (c^D) work to increase friction drag (i.e., $c^T > 0$, $c^D > 0$), while the contribution from the mean convection (c^C) works to reduce it (i.e., $c^C > 0$). In the UB case (Fig. 5.16b) all the components except for c^δ are increased while keeping their signs. In the US case, in contrast, the mean convection term c^C changes to a strong drag augmentation factor and the spatial development term c^D works as a weak reduction factor. From these analyses, we can conclude that the mean convection term c^C which includes $-UV$ has a very important role in determining whether drag reduction or augmentation occurs by UB/US. This argument is more clearly illustrated by the decomposition of the global friction coefficient C_f, i.e.,

$$\begin{aligned}
C_f &= \frac{1}{L_{ctr}} \int_0^{L_{ctr}} c_f \, dx \\
&= \frac{1}{L_{ctr}} \int_0^{L_{ctr}} c^\delta \, dx + \frac{1}{L_{ctr}} \int_0^{L_{ctr}} c^T \, dx + \frac{1}{L_{ctr}} \int_0^{L_{ctr}} c^C \, dx + \frac{1}{L_{ctr}} \int_0^{L_{ctr}} c^D \, dx \\
&= C^\delta + C^T + C^C + C^D. \qquad (4.4)
\end{aligned}$$

Figure 4.7 clearly illustrates that in the UB case the negative contribution from the mean convection term C^C is greater than the positive contribution of Reynolds stress C^T, while in the US case the positive contribution from C^C is larger than the decrease in C^T.

4.3.2 Control efficiency

The control efficiency is briefly discussed here in terms of the drag reduction rate, R, gain, G, and net energy saving rate, S as introduced in §2.8. These measures can be expanded by using the global skin friction coefficients, as

$$G = \frac{C_{f,nc} - C_{f,ctr}}{W_{in}/L_{ctr}}, \quad (4.5)$$

$$S = \frac{C_{f,nc} - \left(C_{f,ctr} + W_{in}/L_{ctr}\right)}{C_{f,nc}}, \quad (4.6)$$

where $C_{f,nc}$ and $C_{f,ctr}$ denote the friction coefficients of the flow with and without blowing/suction, respectively, and and L_{ctr} is the streamwise length of the computational domain. Note that the driving powers for the flows with control W and without control W_0 are equivalent to $C_{f,ctr}L_{ctr}$ and $C_{f,nc}L_{ctr}$, respectively. The input power W_{in} for UB/US is computed as

$$W_{in} = \int_0^{L_{ctr}} \left[(P_w - P_{w-})\, V_{ctr} + \frac{1}{2} V_{ctr}^3 \right] dx, \quad (4.7)$$

where P_{w-} denotes the mean pressure on the opposite side of the wall where the blowing device is connected. Hereafter, the first term on the right hand side is neglected by assuming no pressure difference between P_w and P_{w-}. This is the most optimistic definition.

In Fig. 4.8, G and S computed from the wall shear are shown as an $S-G$ map. The values reported in the previous studies on internal flows are also presented for comparison. As compared to the values in the active control of internal flow, UB gives much higher efficiency.

From more practical viewpoint, the pressure difference between P_w and P_{w-} should be considered. For example, if we apply this blowing for a high-speed train with an intake placed on the front, the pressure loss in the duct leading to the blowing device may become extremely large (in fact, how supply the air itself is a formidable engineering issue). Therefore, the actual control efficiency should be much less than the ideal value presented here.

4.3.3 Effects of uniform blowing/suction on starting position

In the present simulation, uniform blowing or suction is switched on in the control part. Although the magnitude of blowing/suction is gradually changed as shown in Fig. 4.1, it may affect the upstream flow, too. Therefore, dependency on the position where the blowing/suction starts, x_s, has been examined by using 1% uniform blowing/suction.

Figure 4.9 shows the streamwise development of local skin friction coefficient, c_f, for different x_s. The change of boundary condition is observed to affect c_f in the region up to π upstream. In the case of $x_s = 4\pi$, for instance, c_f is found to deviate from the uncontrolled value in the region of $x > 3\pi$, but the profile in further upstream region well collapses with the uncontrolled profile. In the downstream region, the development of c_f is found to be similar unless the blowing region is too short. Judging from these results, we set $x_s = 0$ in the main simulations, since it is desirable to take the statistically steady region as large as possible.

4.3.4 Reynolds number effect

While the present study deals with low Reynolds number turbulence, control effect at high Reynolds number should be a crucial concern toward practical applications. The present analysis enables us to make a rough estimation of the Reynolds number effect. As clearly observed above, the Reynolds stress term (c^T) contributes to increase the drag and the mean convection term (c^C) reduces the drag in the blowing case; the stronger effect of the latter eventually leads to the drag reduction. Since these two terms are considered dominant also at high Reynolds number, the ratio of $-UV$ to $-\overline{u'v'}$ (i.e., integrands of c^C and c^T) should be a good indicator whether the drag reduction effect becomes stronger or weaker. The log-low of wall turbulent flow with uniform blowing/suction is expressed as Stevenson (1963),

$$\frac{2}{V_{ctr}^{+}}\left(\sqrt{1+V_{ctr}^{+}U^{+}}-1\right) \approx \frac{1}{\kappa}\ln\left(y^{+}\right)+B\,, \tag{4.8}$$

where κ and B are constants. By using this, the ratio of $-UV$ to $-\overline{u'v'}$ can be estimated as

$$\frac{-UV|_{ctr}}{-\overline{u'v'}} = \frac{-U^{+}V^{+}|_{ctr}}{-\overline{u'v'}^{+}} \sim \frac{U_{\infty}^{+}V_{ctr}^{+}}{1} = \frac{V_{ctr}}{U_{\infty}}U_{\infty}^{+2} \sim \frac{V_{ctr}}{U_{\infty}}\ln^{2}\left(Re_{\tau}\right)\,. \tag{4.9}$$

This estimate suggests that if the blowing amplitude is constant with respect to the freestream velocity, i.e., $V_{ctr}/U_{\infty} = const.$, the drag reduction effect is stronger at higher Reynolds number.

Considering the practical application in social transports, there are some concerns to examine. The experimental approach and the DNS of compressible turbulent boundary layer with uniform blowing are performed in the appendices A and B.

4.4 Closure

Direct numerical simulations of a spatially developing boundary layer with uniform blowing (UB) or uniform suction (US) were performed. It was found that UB reduces friction drag and enhances turbulence, while US enhances friction drag and suppress turbulence, similarly to blowing/suction slot and UB and US applied in channel flow previously studied. Quantitative analysis using the FIK identity revealed that the mean convection term works as a drag reduction factor in the uncontrolled spatially developing boundary layer, while the Reynolds shear stress term and the spatial development term work as drag augmentation factors. The mean convection term has a very important role in determining whether drag reduction or drag augmentation occurs by UB/US: the drag reduction in the UB case is attributed to the negative contribution from the mean convection term; likewise, the drag augmentation in the US case is due to the positive contribution from the mean convection term. In fully developing internal flows, the suppression of turbulence is a major strategy to reduce drag, as is mathematically implied by the FIK identity. In spatially developing boundary layers, in contrast, use of the mean convection term is considered as the efficient way of reducing the friction drag, even if it increases turbulence away from the wall.

An order-of-magnitude analysis suggests that the drag reduction effect may be stronger at higher Reynolds number if the blowing amplitude relative to the freestream velocity is fixed. Details in high Reynolds number flows including the effect of very large-scale motion (see e.g., Marusic et al., 2010a), however, should be investigated further. There also remains another practical issue: how to get mass for uniform blowing. This issue is highly dependent on the geometrical shape of control target. For an airfoil, for instance, it may be possible to apply suction near the leading edge to suppress the transition and to apply blowing near the trailing edge to reduce the friction of developed turbulence; but it might be more difficult for the object like bullet trains. These practical issues remain open for the future work.

(a)

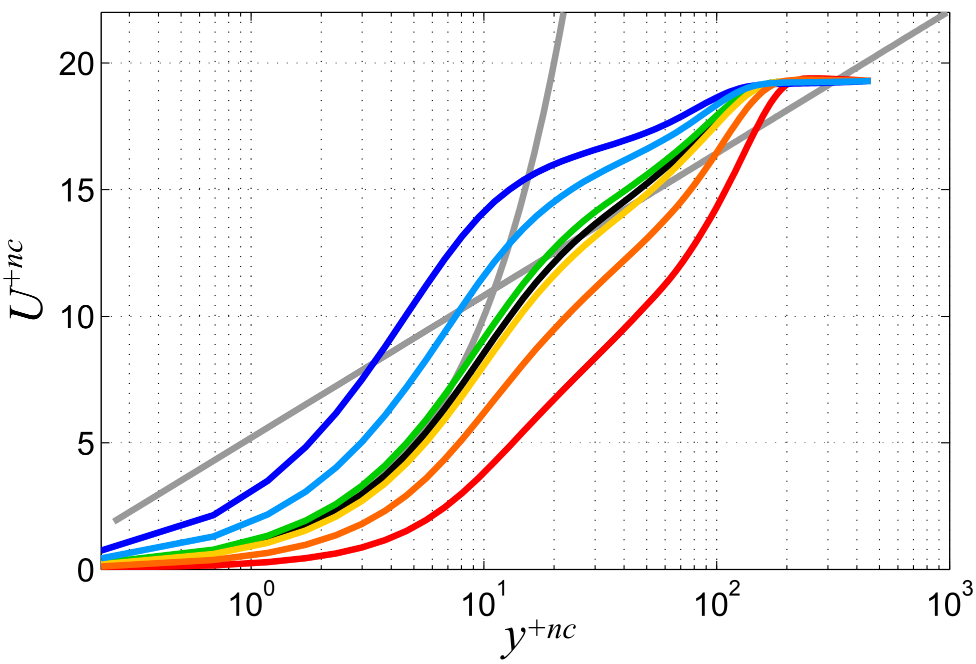

(b)

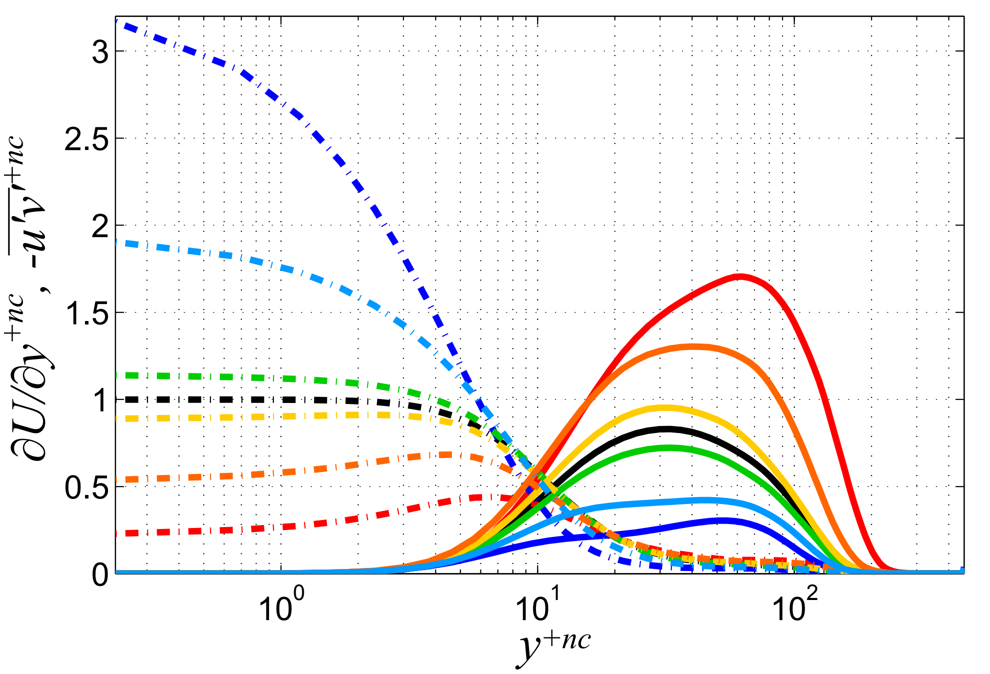

Figure 4.3: Effect of UB/US on statistics as a function of y^{+nc} at the location of $Re_{\theta,nc} = 430$: black, no control; yellow, 0.1% UB; orange, 0.5% UB; red, 1% UB; green, 0.1% US; light blue, 0.5% US; blue, 1% US. (a) Streamwise mean velocity. (b) Shear stresses: solid, Reynolds shear stress; dashed, viscous shear stress.

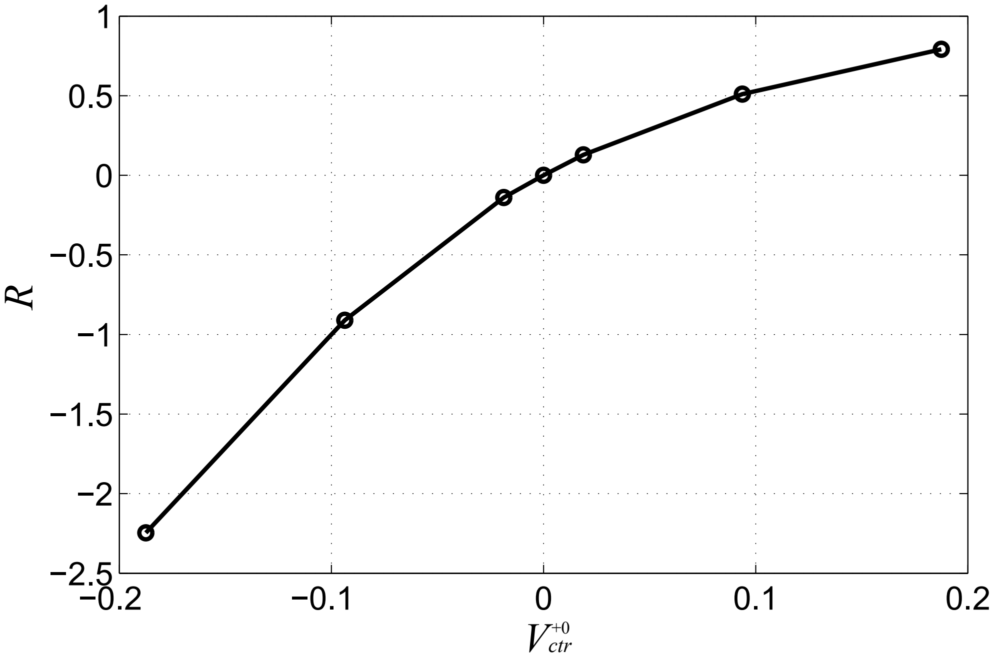

Figure 4.4: Drag reduction rate as a function of control amplitude.

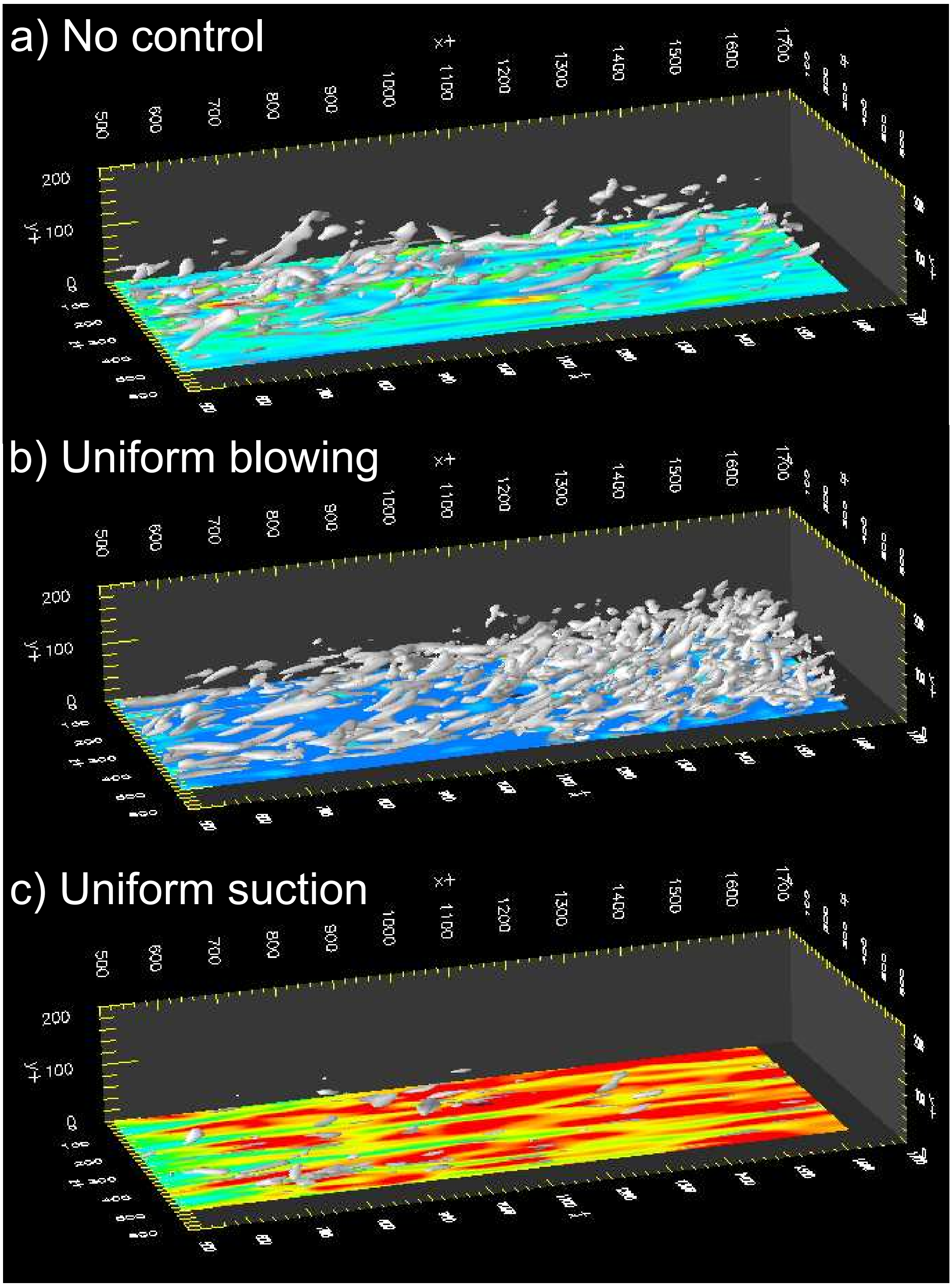

Figure 4.5: Visualization of flow in the control region using the 2nd invariant of the deformation tensor Q^{+0} and contours of the wall shear stress τ_w^{+0}: a) no control, b) 1% UB, c) 1% US.

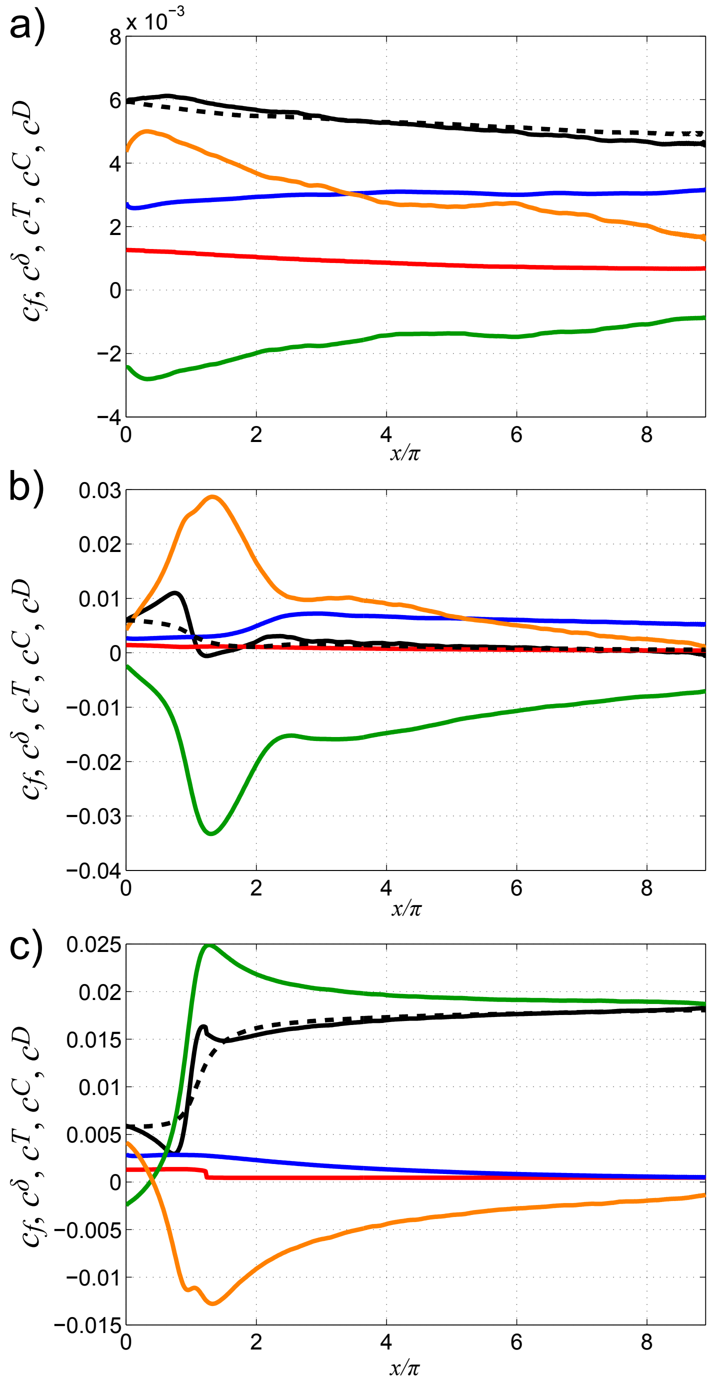

Figure 4.6: Each term of the FIK identity affected by UB/US control: a) no control, b) 1% UB, c) 1% US. Black, FIK total; red, c^{δ}; blue, c^{T}; green, c^{C}; orange, c^{D}; dashed line, c_f from $\partial U/\partial y$ on the wall.

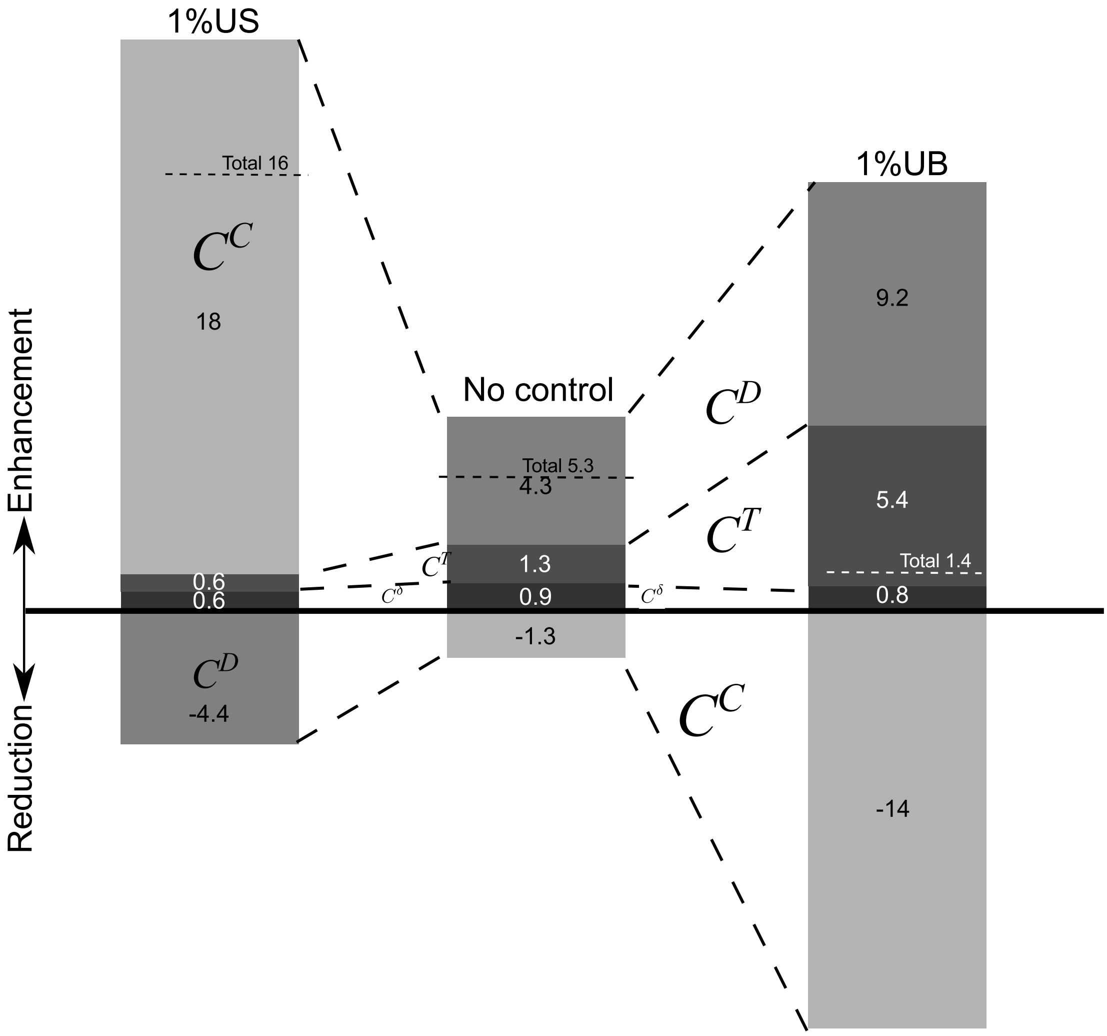

Figure 4.7: Different dynamical contributions to the global friction drag coefficient ($\times 10^{-3}$)

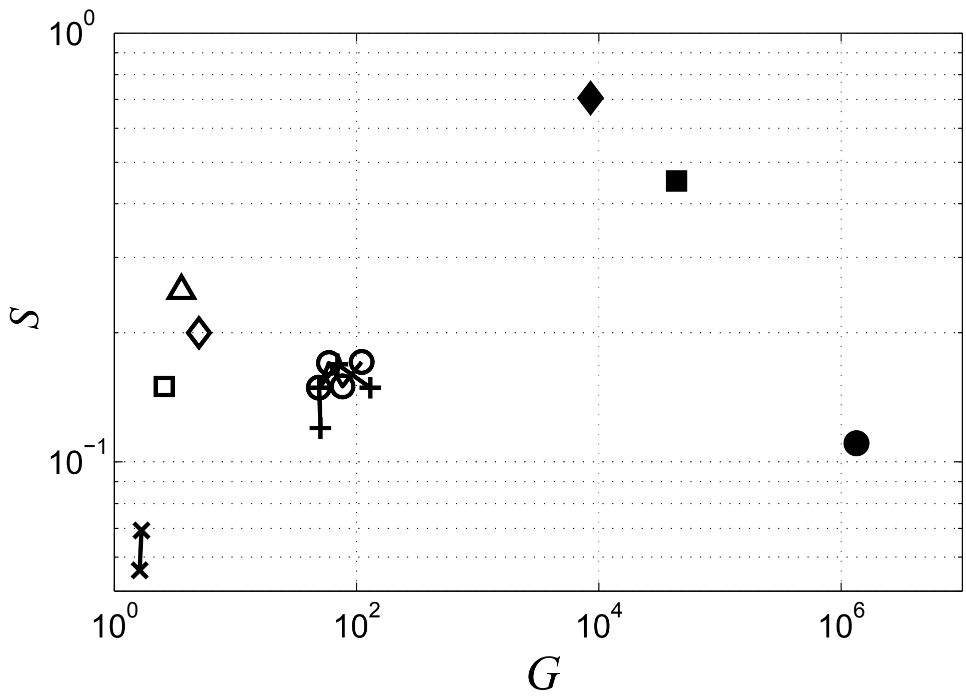

Figure 4.8: Net energy saving rate achieved by different active control schemes: $\circ$, Choi et al. (1994)'s opposition control (computed by Iwamoto et al. (2002) at a different Reynolds number); $+$, Lee et al. (1998)'s suboptimal control (Iwamoto et al., 2002); $\times$, temporally-periodic spanwise wall-oscillation (Quadrio and Ricco, 2004); $\diamond$, streamwise traveling wave (Min et al., 2006); $\square$, steady streamwise forcing (Xu et al., 2007); $\triangle$, spatially-periodic spanwise oscillation (Yakeno et al., 2009). Solid markers denote UB in the present simulation: ♦, 1% UB; ■, 0.5% UB; ●, 0.1% UB.

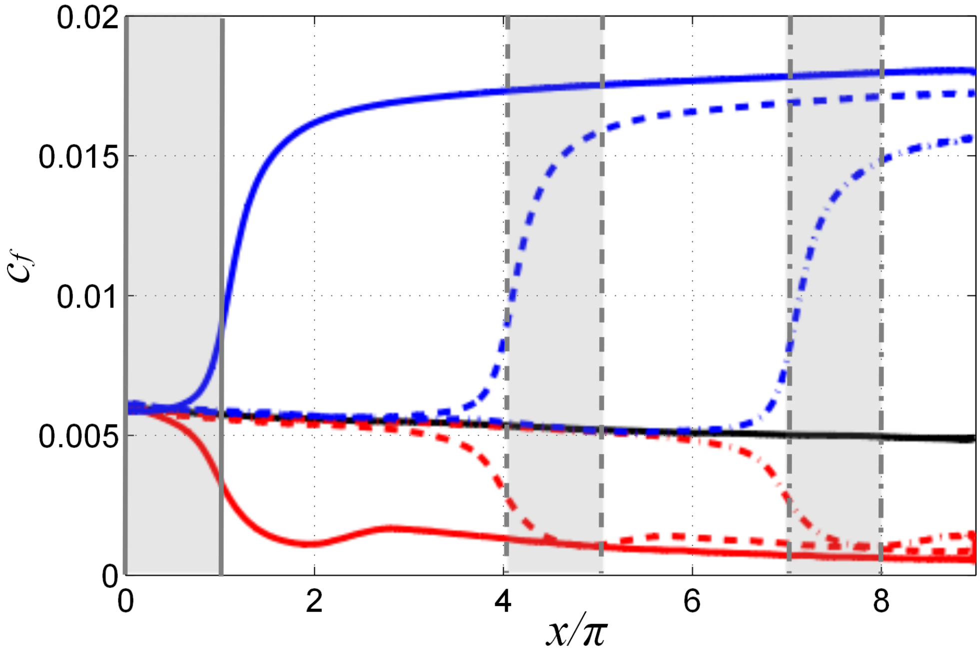

Figure 4.9: Effect of positions of control starting zone: Black, no control; red,UB; blue, US. Solid,$0 \leq x_s/\delta_0 \leq \pi$; dashed, $4\pi \leq x_s/\delta_0 \leq 5\pi$; chain, $7\pi \leq x_s/\delta_0 \leq 8\pi$. Gray mask, control starting zone.

Chapter 5

Uniform cooling/heating

In the previous chapter, it was found that uniform blowing achieves the skin friction drag reduction. The exact 'uniform' blowing is still difficult to realize. Instead, here, the body force is focused. The buoyancy is generated by the wall surface-cooling or heating without a roughness due to the devices on wall-surface. In this chapter, analysis of the effect of uniform heating/cooling is performed. In this chapter, an instantaneous temperature, a mean temperature and its fluctuation components are denoted as θ, Θ, and θ', respectively.

5.1 Wall surface-heating/cooling

The buoyancy is calculated by Boussinesque approximation as following;

$$f_i = Ri\theta\delta_{2i} \ . \tag{5.1}$$

The temperature is non-dimensionalized by a thermal gap between free-stream and wall, $\Delta\theta$. The Richardson number Ri is defined as

$$Ri = \frac{g^*\beta^*\Delta\theta^*\delta_0^*}{U_\infty^{*2}} \ , \tag{5.2}$$

where g, β, $\Delta\theta$ denote a gravitational acceleration, thermal expansion coefficient, and Thermal gap, respectively. The Boussinesque approximation can be adapted when the density is a function of only temperature, viz., the small temperature variation and constant thermal expansion coefficient is assumed. In order to use the buoyant

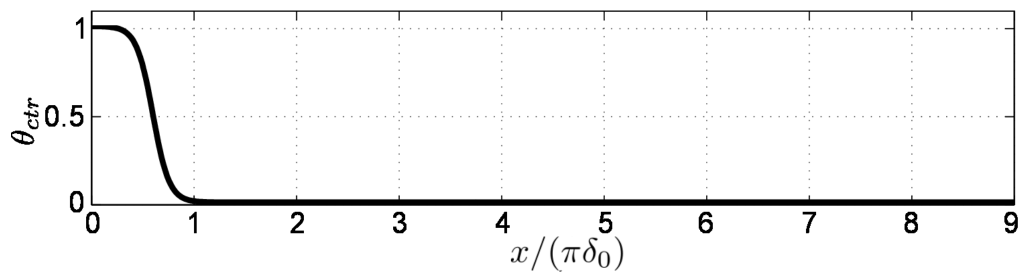

Figure 5.1: Profile of control input.

force as a control medium, uniform wall-heating (UH) or cooling (UC) is applied. The buoyancy is taken into account by the Boussinesq approximation and driven by the thermal difference between the free-stream and wall. In the present study, the magnitude of UH and US is set to be Ri $(Gr) = \pm 0.01$ (0.9×10^5), ± 0.02 (1.8×10^5), ± 0.1 (9×10^5), where positive sign denotes heating and negative sign denotes cooling. The corresponding Grashof number is given by $Gr = Ri\, Re^2$. Hattori et al. (2007) performed DNS with the thermal rescaling method of Kong et al. (2006) to create the inlet profile of temperature. In the present study, in contrast, we aim at using buoyancy as a control medium; therefore, uniform temperature is introduced at the inlet and a different wall-temperature is set in the main region. For smooth transition from the freestream temperature ($\theta = 1$) to the wall temperature ($\theta = 0$), a transition zone is located at $0 \leq x \leq \pi$, in which the temperature is gradually varied using a hyperbolic tangent function, as shown in Fig. 5.1.

5.2 Result

The effects of wall-heating/cooling on the spatial development of boundary layer thickness are shown in Fig. 5.2 as Reynolds numbers. Here, the momentum thickness δ_m and the enthalpy thickness δ_Δ are defined as

$$\delta_m = \int_0^\infty U(1-U)dy \tag{5.3}$$

$$\delta_\Delta = \int_0^\infty U(1-\Theta)dy\,, \tag{5.4}$$

where U and Θ denote the mean velocity and temperature, respectively. These profiles show that the momentum thickness is thickened by wall heating, while thinned by cooling. Similar trends appears in the development of thermal boundary layer, viz. the development of the thermal boundary layer is promoted by wall heating, while suppressed by cooling. The magnitude of both effects depends on the Richardson number. The iso-surface of instantaneous temperature is presented in Fig. 5.3. It is found that UH increases the thermal fluctuations by forming unstable stratification, while UC decreases it by forming stable stratification: the turbulence behaves as if its effective Reynolds number were increased (decreased) by the UH (UC) control. These trends are in accordance with the observation by Hattori et al. (2007).

Figure 5.4 shows the local friction coefficient c_f as a function of streamwise distance x from the inlet, defined as

$$c_f = \frac{\tau_w^*}{\frac{1}{2}\rho^* U_\infty^{*2}}, \tag{5.5}$$

where $\tau_w^* = \mu(\partial U^*/\partial y^*)_w$. It is found that the skin friction drag is reduced by UC, while enhanced by UH. The amplitude of buoyancy, $|Ri|$, affects on the profiles: the large amplitude results in larger reduction/enhancement of skin friction drag. Figure 5.5 presents the local Stanton number, defined as

$$St = \frac{q_w^*}{\rho^* c_p^* U_\infty^* \Delta\theta^*}, \tag{5.6}$$

where c_p denotes specific heat and $q_w = \lambda^*(\partial\Theta^*/\partial y^*)_w$. Since the thermal boundary layer forms from the starting point of control, the Stanton number is quite large at the upstream location, i.e., $Re_{\delta_m,nc} < 360$ (where the subscript nc denotes the value in the uncontrolled case). In the downstream region, a similar trend to that for the local friction coefficient is noticed. These trends in c_f and St are basically similar to those previously reported for a channel flow Iwamoto et al. (2002) and a spatially developing boundary layer (although the Reynolds number assumed by Hattori et al. (2007) is higher than the present study).

Figures 5.4 and 5.5 also show that friction coefficient reaches a curve of fully-heated/cooled turbulent boundary layer around $Re_{\delta_m,nc} \geq 430$ $(x \geq 13)$. Small oscillation observed near the downstream end of present computational domain, $Re_{\delta_m,nc} \geq 530$, especially in the UH cases is likely to be due to numerical instability. The Reynolds analogy factor $2St/c_f$ is shown in Fig. 5.6. Although the analogy factor is around unity in fully-developed flow, it is larger than unity in the present cases.

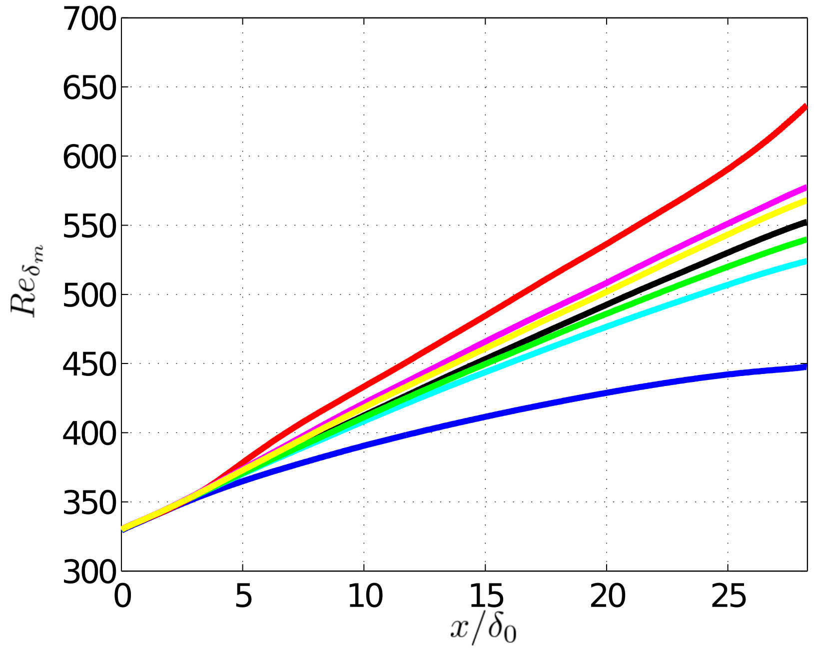

(a)

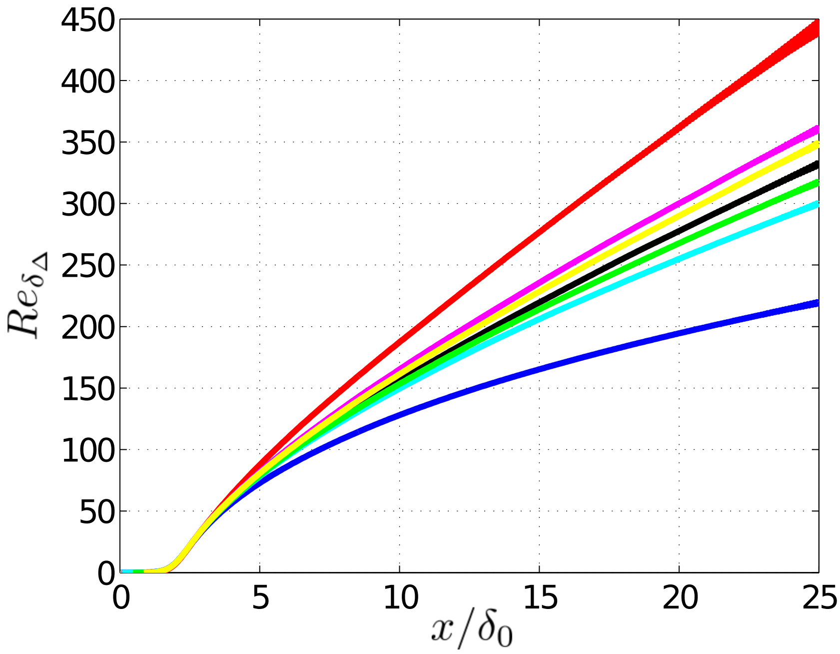

(b)

Figure 5.2: Control effects on the boundary layer thicknesses: (a) momentum thickness; (b) enthalpy thickness. Black, no control; red, $Ri = 0.1$; magenta, $Ri = 0.02$; yellow, $Ri = 0.01$; green, $Ri = -0.01$; light blue, $Ri = -0.02$; blue, $Ri = -0.1$.

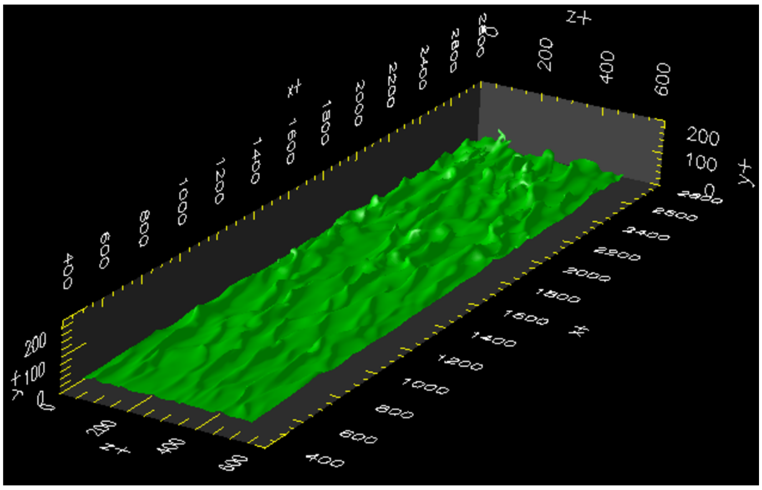

(a)

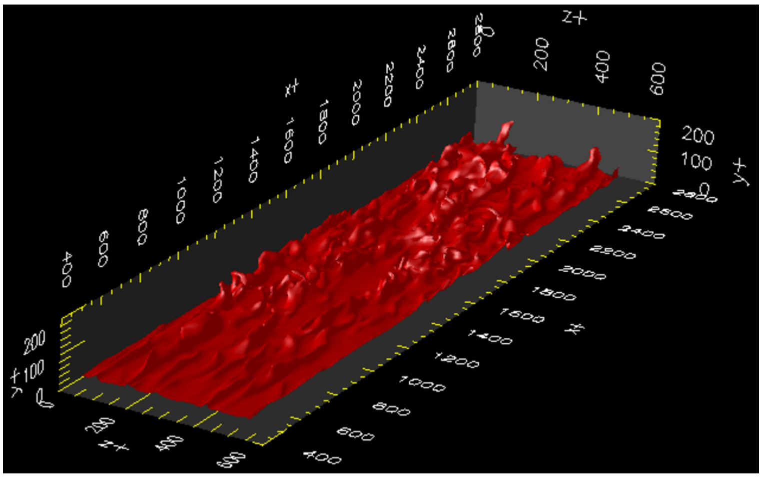

(b)

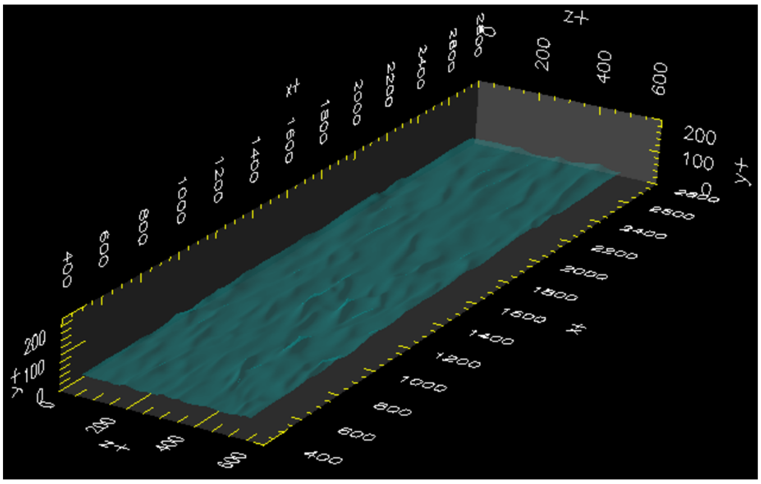

(c)

Figure 5.3: Iso-surfaces of temperature $\theta = 0.7$: (a) no control; (b)$Ri = 0.1$; (c) $Ri = -0.1$.

This is because in the present simulations the onset of thermal boundary layer is more downstream than that of the velocity boundary layer, and the thermal boundary layer is always thinner than the velocity boundary layer. As compared to the uncontrolled case, the analogy factor is found to be slightly smaller in UH cases and larger in UC cases.

Figure 5.7 shows the drag reduction rate R calculated by using the global friction coefficient, as

$$R = \frac{C_{f,nc} - C_{f,ctr}}{C_{f,nc}} \,, \tag{5.7}$$

where

$$C_f = \frac{1}{L_{ctr}} \int_0^{L_{ctr}} c_f(x)\, dx \tag{5.8}$$

with the subscripts of nc and ctr denoting the uncontrolled and controlled cases, respectively, and L_{ctr} being the streamwise length of the controlled region. This indicates that larger amplitude of control achieves higher drag reduction (enhancement) by UC (UH). In the present study, $R \approx 65\%$ is achieved in UC case at $Ri = -0.1$, while $R \approx -30\%$ in UH at $Ri = 0.1$. In the range between $-0.02 \leq Ri \leq 0.02$, the figure suggests that there is a nearly linear relationship between the control amplitude and the drag reduction rate.

The mean streamwise velocity profiles at the location of $Re_{\delta_{m,nc}} = 430$ are shown in Fig. 5.8. The mean velocity is also nondimensionalized by the wall units of the uncontrolled case. As compared to the uncontrolled case, the profiles are shifted away from the wall by UC and toward the wall by UH.

The root-mean-square (rms) of each velocity component at $Re_{\delta_{m,nc}} = 430$ is shown in Figs. 5.9(a)-(c). Obviously, the turbulence is suppressed by UC and enhanced by UH. The streamwise velocity fluctuations are more significantly influenced by the strong cooling. The peaks shift to the wall by UH, while away from the wall by UC. A second peak appears at $60 \leq y^{+nc} \leq 110$ for UH at $Ri = 0.1$. This second peak becomes clearer as the Reynolds number is increased (not shown). The wall-normal fluctuations are directly influenced by the buoyancy for its direction. Therefore, UH and UC with the same magnitude augment and suppress it almost equally. The peaks remain in the log-law region ($40 \leq y^{+nc} \leq 100$). The trend for the spanwise fluctuations is found to be similar to that for the wall-normal fluctuations. In addition, the spanwise fluctuations are observed to be influenced by UH/UC in the region closer to the wall than that for the wall-normal fluctuations.

The Reynolds shear stress and viscous shear stress are shown in Fig. 5.10. It can be seen that UC reduces the viscous shear stress, while UH enhances it. The Reynolds shear stress is also reduced by UC, while increased by UH. In UC at $Ri = -0.1$, the flow is almost relaminarized and the viscous shear stress is dominant. These results suggest that the vortical motion in vicinity of the wall is suppressed and the flow is stabilized by UC, while UH destabilizes the flow. Namely, as is well known, UC forms stable density stratification, while UH does unstable one.

The mean and rms temperatures are shown in Figs. 5.11 and 5.12, respectively. Since the thermal boundary layer begins to form in the upstream region of the computational domain, its thickness is thin compared to the momentum thickness; therefore, log-law region is not clearly observed in the mean temperature profile. Apart from that difference, similar trends to those for the streamwise mean velocity are observed: the profiles are shifted toward the wall by UH and away from the wall by UC. Similarly, the thermal fluctuations are promoted by UH, while suppressed by UC. Figure 5.13 shows the turbulent heat flux: the streamwise, $\overline{-u'\theta'}$, and the wall-normal, $\overline{-v'\theta'}$, components. The intensities are affected by UH/UC similarly to those of the streamwise velocity fluctuations. In the log-law region of mean velocity, however, the temperature fluctuations rapidly vanish. This is, again, because in the present simulations the thermal boundary layer is always thinner than the velocity boundary layer. The streamwise turbulent flux takes negative value, while the wall-normal flux takes positive value. With UC (UH), their magnitudes are decreased (increased). These results also support the argument that turbulence is suppressed (enhanced) by UC (UH). The peaks of the streamwise turbulent heat flux shift toward wall by UH and away from the wall by UC in the buffer layer, while those of wall-normal flux almost remain in the log-law layer. In the budget of the Reynolds shear stress, an additional term, $-Ri\overline{u'\theta'}$, appears. In UH cases, i.e., positive Richardson numbers, this term works as a gain for the Reynolds shear stress (as mentioned in Hattori et al., 2007, too), while the opposite in UC cases. These modifications of streamwise turbulent heat flux and the shift of its peak indirectly affects the change in skin friction drag via the change of the Reynolds shear stress.

Figure 5.14 shows the budgets of turbulent kinetic energy:

$$0 = C_k + P_k + D_k^p + D_k^\mu + D_k^T + \varepsilon_k + B_k, \tag{5.9}$$

where terms in right hand side denote the convection term, the production term, pressure diffusion term, the viscous diffusion term, the turbulent diffusion, the dissipation and the buoyancy term, in order. For the computation of budgets, the consistent scheme by Mamori and Fukagata Mamori and Fukagata (2010) is used. In the uncontrolled case, the convection term is quite small, which indicates that the contribution from each term is similar to that in a channel flow. The buoyancy term appears as a gain factor in UH case ($Ri = 0.1$), and a loss factor in UC case ($Ri = -0.1$). Accordingly, the turbulent kinetic energy is increased in UH case, while decreased in UC case. In the UC case, all terms are much smaller than those of uncontrolled flow, which leads toward relaminarization especially near the wall ($y^{+nc} \leq 10$).

5.3 Discussion

5.3.1 Analysis by using FIK identity

Dynamical decomposition of skin friction coefficient is performed by using the FIK identity Fukagata et al. (2002a) in order to clarify the contributions of different effects on the change of skin friction. In this chapter, the local skin friction coefficient c_f is decomposed into five different dynamical contributions: the contributions from boundary layer thickness, c^δ, the Reynolds shear stress, c^T, mean convection, c^C, spatial development, c^D, and pressure gradient (due to buoyancy, as explained below), c^P, shown as

$$c^P(x) = -2\int_0^1 (1-y)^2 \left(-\frac{\partial P}{\partial x}\right) dy. \tag{5.10}$$

By integrating local friction coefficient in the streamwise direction, the global friction coefficient C_f is also decomposed as

$$\begin{aligned} C_f = \frac{1}{L_{ctr}}\int_0^{L_{ctr}} c_f(x)dx &= \frac{1}{L_{ctr}}\int_0^1 \left(c^\delta(x) + c^T(x) + c^C(x) + c^D(x) + c^P(x)\right) dx \\ &= C^\delta + C^T + C^C + C^D + C^P \ . \end{aligned} \tag{5.11}$$

These equations indicate two main directions to reduce the skin friction drag: suppression of the Reynolds stress term and enhancement of the mean convection term. An example of the former is a turbulence control aiming at suppression of quasi-streamwise vortices, such as the opposition control Choi et al. (1994); Fukagata et al. (2002a). On the other hand, an example of the latter is a spatially developing turbulent boundary layer with uniform blowing from the wall performed in Chap. 4.

Figure 5.15 presents the decomposed local skin friction coefficient in the uncontrolled and controlled cases at $Ri = \pm 0.02$. All cases have a similar balance, except for the pressure gradient term: c^{δ}, c^{T}, and c^{D} are the enhancement factors for the skin friction drag, while c^{C} is the reduction factor. In the uncontrolled case, the pressure gradient term c^{P} is zero. The small deviation near the inlet and outlet is due to the boundary condition. However, non-zero c^{P} is generated by UC and UH. In UC case, the cooled bulk fluid is accelerated downward due to gravity. This nearly homogeneous downward acceleration should mostly be canceled by the wall-normal pressure gradient. Thus, the pressure near the wall increases to generate negative c^{P}. The positive c^{P} in UH case can also be explained likewise. Note that, unlike the cases of uniform blowing or suction, the mean wall-normal velocity should hardly be affected directly by UC or UH due to the impermeable condition on the wall and the incompressibility constraint.

The contributions to the global friction coefficient for the uncontrolled, uniform heating (UH) and cooling (UC) cases at $Ri = \pm 0.02$ are compared in Fig. 5.16. It is clearly shown that UC reduces friction drag by reducing the Reynolds stress term C^{T} and enhancing the mean convection term C^{C}. It is also clear that C^{C} has a negative contribution; namely, it works as a drag reduction factor. The pressure gradient term is smallest in each case, but it grows as the control amplitude becomes higher. The summation of the mean convection term C^{C} and the spatial development term C^{D} (which is originally defined as *the spatially development term* in Fukagata, Iwamoto, and Kasagi, 2002a), are almost equal in both UH and UC cases. Therefore, the effect of drag reduction or enhancement mostly comes from the change in the Reynolds stress term C^{T}. This is clearly different from the cases of uniform blowing (suction), where the major contributor to the friction drag reduction (enhancement) is the negative (positive) mean convection term.

5.3.2 Control efficiency

In the present cases, the driving powers for the flows with control W and without control W_0 are equivalent to $C_{f,ctr}L_{ctr}$ and $C_{f,nc}L_{ctr}$, respectively. The input power, W_{in}, for the uniform heating/cooling is computed as

$$W_{in} = \frac{1}{Re\ Pr}\int_0^{L_{ctr}} \left| \left. \overline{\frac{\partial \theta}{\partial y}} \right|_w \right| dx\ . \tag{5.12}$$

Figure 5.17 shows the relationship between G and S computed using the DNS data. The values reported in the previous studies for channel flows and uniform blowing (UB) control in spatially developing boundary layer are also shown for comparison. It is clearly seen that the net energy saving rate is largely negative in all uniform cooling (UC) cases examined in the present study; namely, the control requires more power than it can save the driving power.

In order to clarify the reason for this low efficiency, the kinetic energy generated by the buoyancy, W'_{in}, is calculated as Fukagata et al. (2009)

$$W'_{in} = \int_{\mathcal{V}} |Ri|\ \overline{v(1-\theta)}\ d\mathcal{V}\ , \tag{5.13}$$

where $\mathcal{V}$ denotes the computational domain. Figure 5.18 shows the conversion ratio W'_{in}/W_{in} at different Richardson numbers. The conversion ratio is found to be very small and mildly increases with the Richardson number. Even at $Ri = 0.1$, only 13.5% of thermal energy is converted into kinetic energy and the rest is simply convected away.

Richardson number is expressed as

$$Ri = \frac{g^* \beta^* \Delta\theta^* \delta_0^*}{U_\infty^{*2}} = \frac{Gr}{Re^2}\ , \tag{5.14}$$

where Gr is Grashof number which shows ratio of the buoyancy to the viscosity as

$$Gr = \frac{g^* \beta^* \Delta\theta^* \delta_0^{*3}}{\nu^{*2}}. \tag{5.15}$$

To set higher Richardson number to produce the stronger buoyant force, the higher Grashof number is needed, viz., large temperature gap, $\Delta\theta$. However, this operation may break the Boussinesque approximation for the buoyancy and the investigation in compressible flow should be done.

5.3.3 Reynolds number effect

From Eq. 5.14, the buoyancy is inversely proportional to Re^2. Therefore, to gain the buoyancy in high Reynolds number flow, higher Grashof number is necessary. However, as mentioned above, it is not possible to adapt the Boussinesque approximation for the buoyancy anymore. It is supposed to be difficult the friction drag reduction by the Buoyancy in high Reynolds number flow.

5.4 Closure

We performed DNS of zero-pressure-gradient turbulent plane boundary layer flow at $Re_{\tau,0} \approx 160$ with uniform cooling/heating aiming at reduction of skin friction drag. In this low Reynolds number flow, the uniform cooling achieved 65% friction drag reduction, while heating resulted in 30% drag increment.

From the shear stress profiles, it is found that uniform cooling reduces both of the viscous shear stress and the Reynolds shear stress, while uniform heating has the opposite trend.

The mechanism of skin friction drag reduction by uniform cooling is found to be different from that by uniform blowing. The cooling control achieves drag reduction by reducing the vortices near the wall, i.e., reducing the Reynolds stress term in the FIK identity, while the uniform blowing does it by blowing the vortices away from the wall, i.e., enhancing the mean convection term.

Although skin friction drag is reduced by uniform cooling, the net energy saving rate is found to be largely negative; namely, net energy saving is not achieved. This is because only a small portion of thermal input is used to generate the buoyant force and the rest is convected away unused. The situation is considered more severe in practical high Reynolds number flows because an extremely large temperature difference will be required according to the definition of Richardson number ($Ri = Gr/Re^2$).

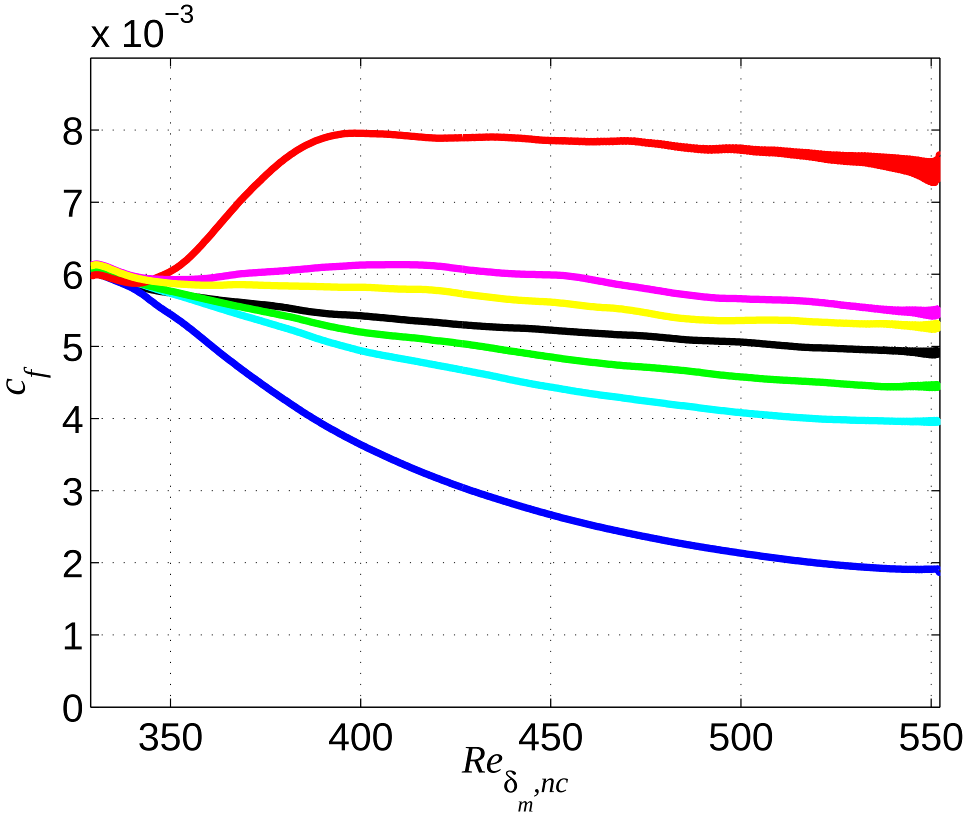

Figure 5.4: Control effects on friction coefficient. Black, no control; red, $Ri = 0.1$; magenta, $Ri = 0.02$; yellow, $Ri = 0.01$; green, $Ri = -0.01$; light blue, $Ri = -0.02$; blue, $Ri = -0.1$.

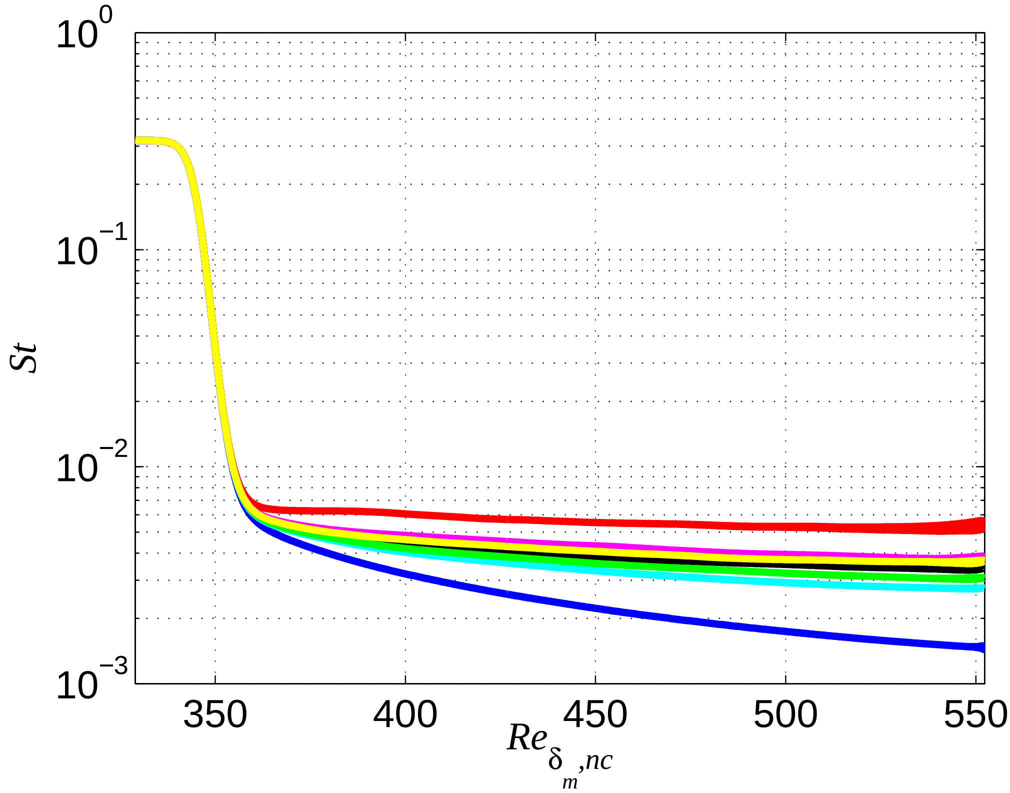

Figure 5.5: Control effects on Stanton number. Black, no control; red, $Ri = 0.1$; magenta, $Ri = 0.02$; yellow, $Ri = 0.01$; green, $Ri = -0.01$; light blue, $Ri = -0.02$; blue, $Ri = -0.1$.

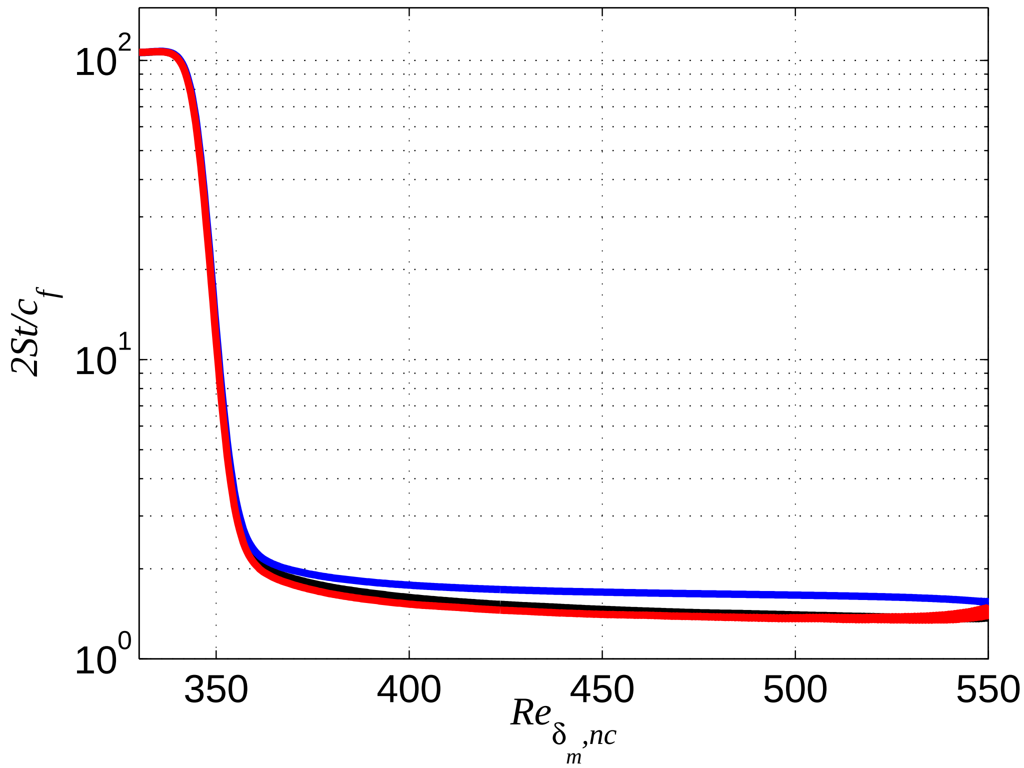

Figure 5.6: Control effects on analogy factor, $2St/c_f$. Black, no control; red, $Ri = 0.1$; magenta, $Ri = 0.02$; yellow, $Ri = 0.01$; green, $Ri = -0.01$; light blue, $Ri = -0.02$; blue, $Ri = -0.1$.

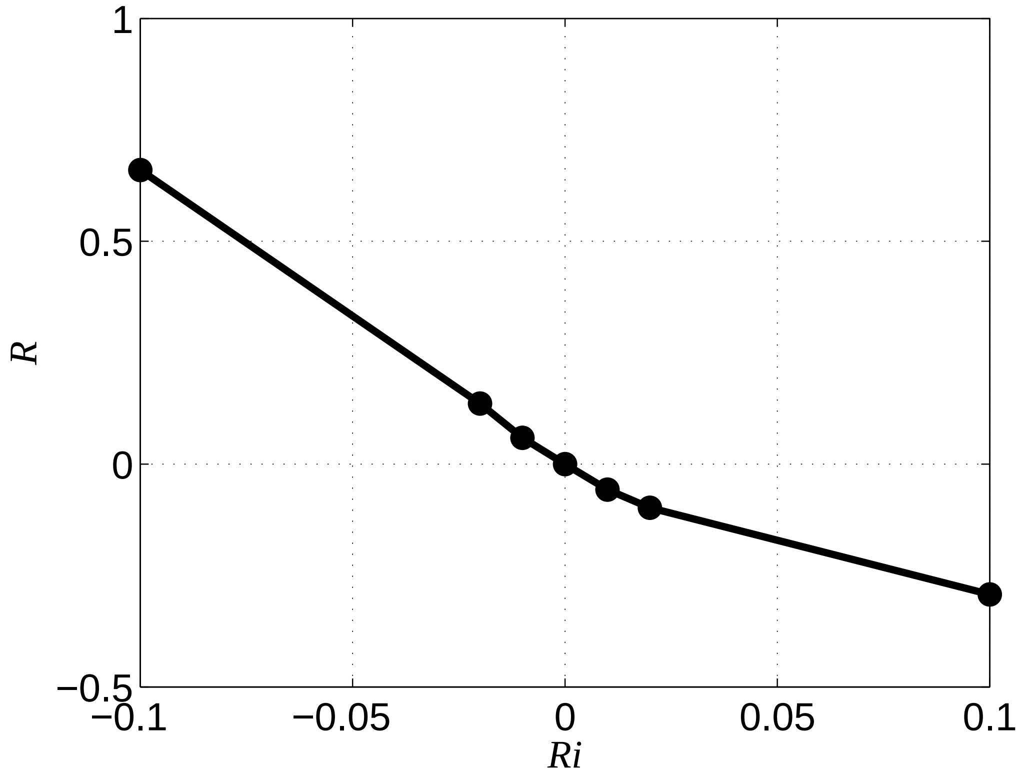

Figure 5.7: Drag reduction rate as a function of Richardson number at $Re_{\delta_m,nc} = 430$.

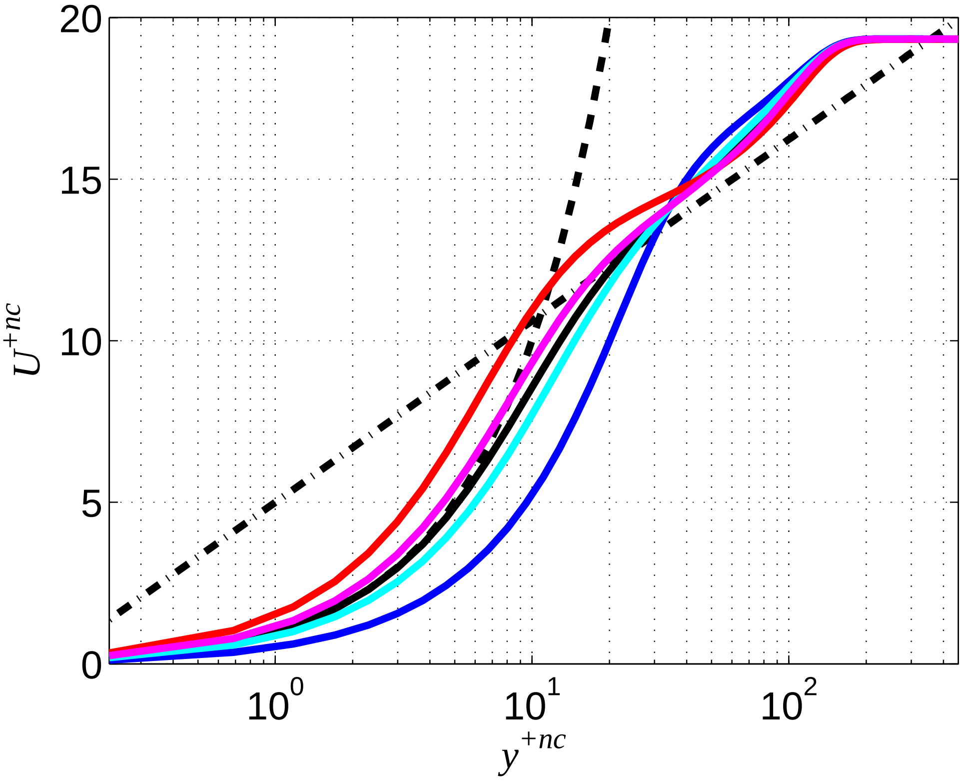

Figure 5.8: Streamwise mean velocity at $Re_{\delta_m,nc} = 430$. Colors are the same as those in Fig. 5.2

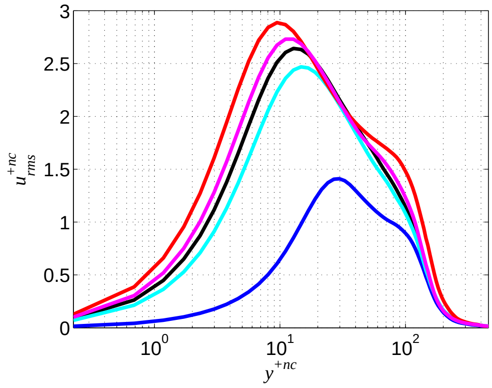

(a)

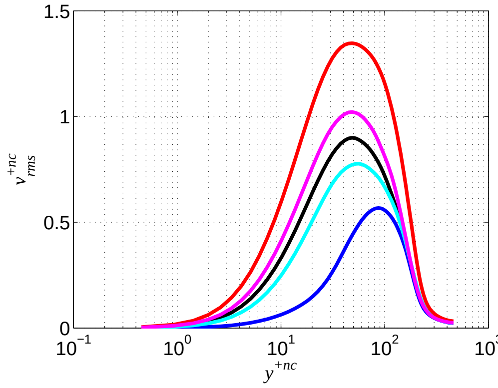

(b)

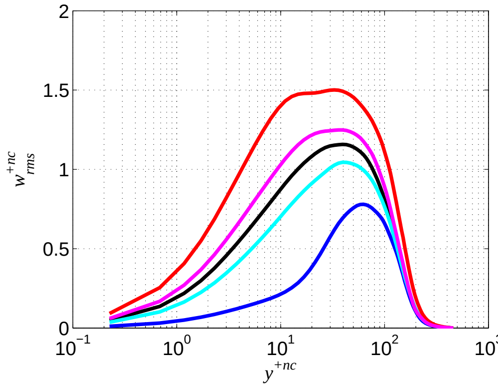

(c)

Figure 5.9: (a) Streamwise velocity fluctuation; (b) Wall-normal fluctuation, (c) Spanwise fluctuation at $Re_{\delta_m,,nc} = 430$. Colors are the same as those in Figure 5.2.

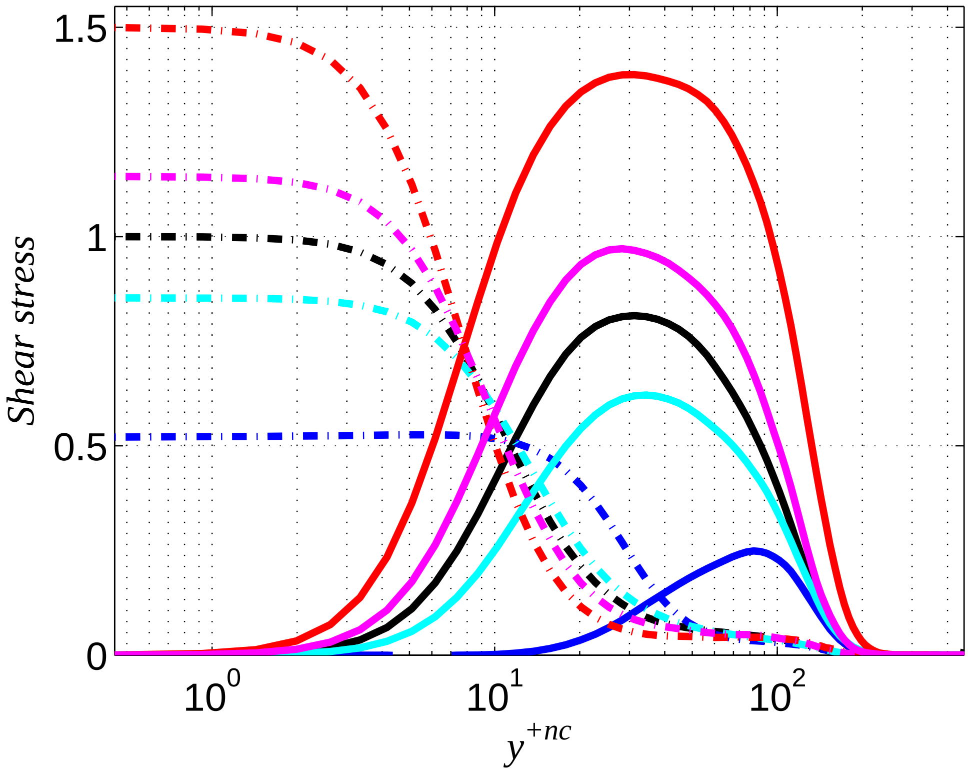

Figure 5.10: Shear stress at $Re_{\delta_{m},nc} = 430$: solid, Reynolds shear stress; dashed, viscous shear stress. Colors are the same as those in Figure 5.2.

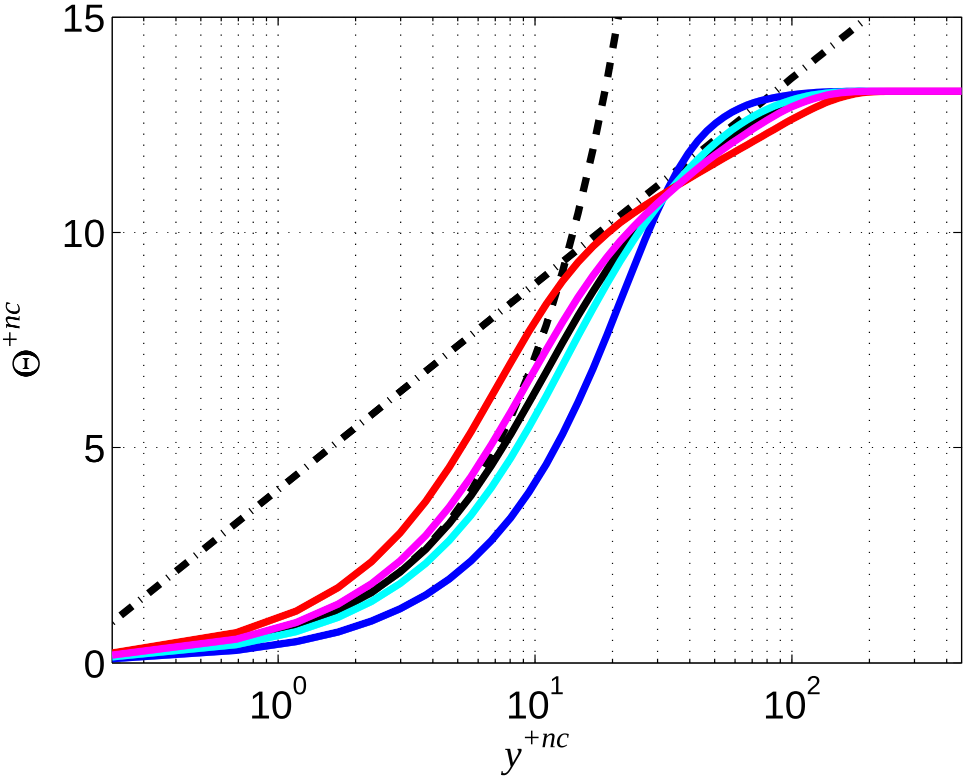

Figure 5.11: Mean temperature at $Re_{\delta_{m,},nc} = 430$. Colors are the same as those in Fig. 5.2.

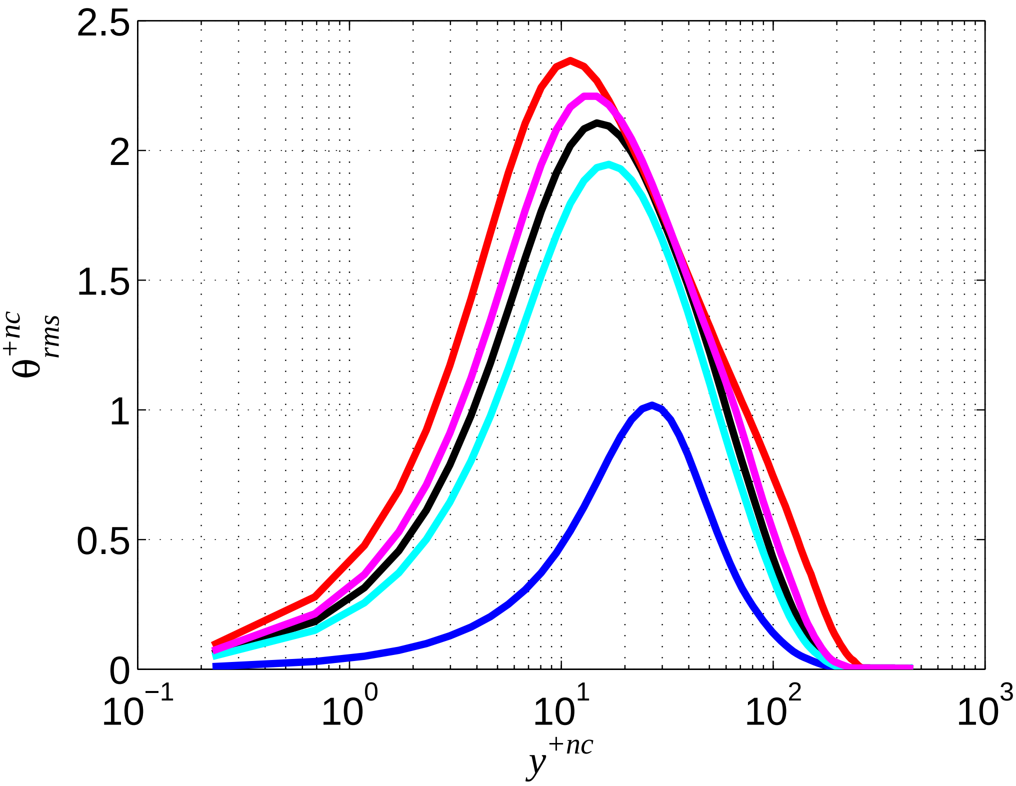

Figure 5.12: Root-mean-square of tempurature fluctuations at $Re_{\delta_{m,},nc} = 430$. Colors are the same as those in Fig. 5.2.

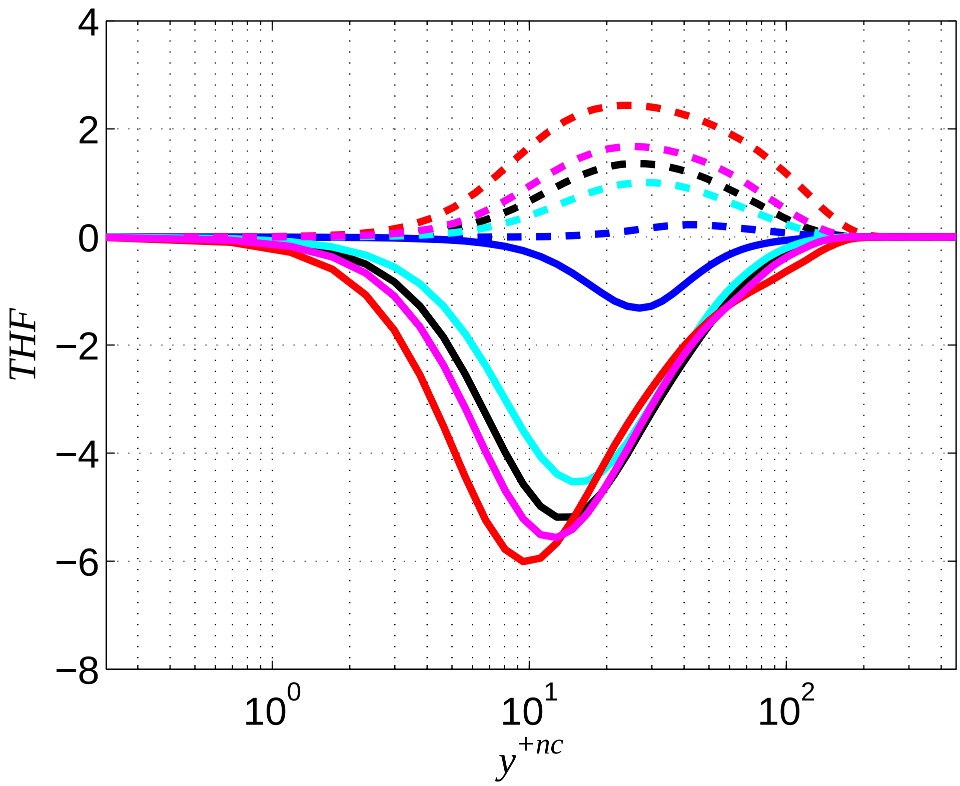

Figure 5.13: Turbulent heat fluxes (THF); solid, $-\overline{u'\theta'}$; dashed, $-\overline{v'\theta'}$ at $Re_{\delta_{m},,nc}$ = 430. Colors are the same as those in Fig. 5.2.

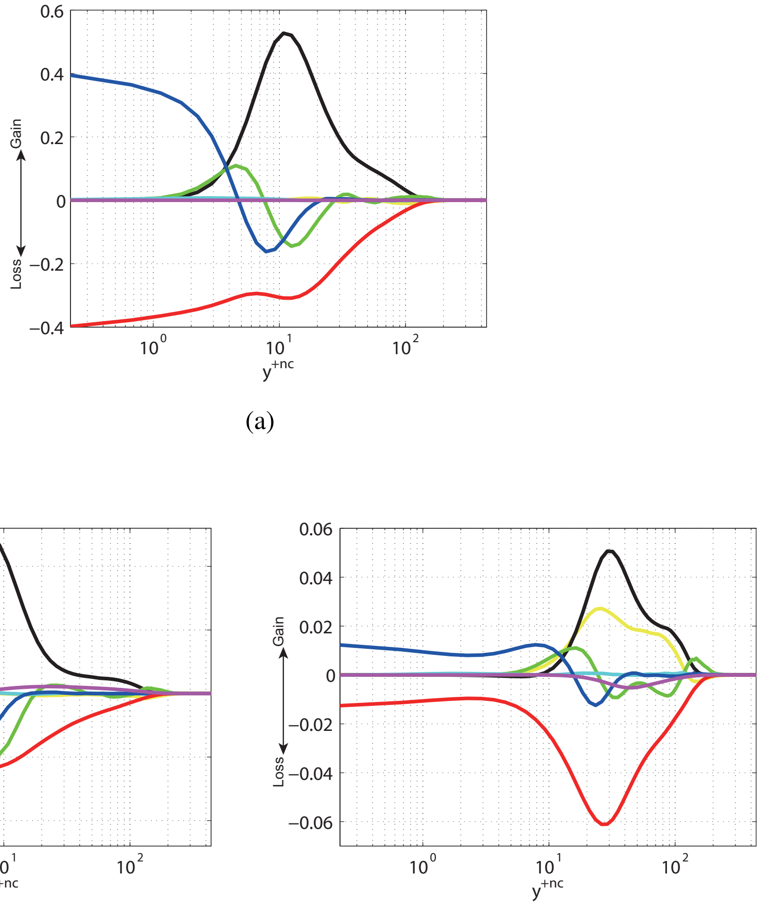

(a)

(b)

(c)

Figure 5.14: Budget of turbulent kinetic energy: (a) no control; (b) UH case ($Ri = 0.1$); (c) UC case ($Ri = -0.1$). Black, production; red, dissipation; blue, viscous diffusion; yellow, convection; light blue, pressure diffusion; green, turbulent diffusion; magenta, buoyancy.

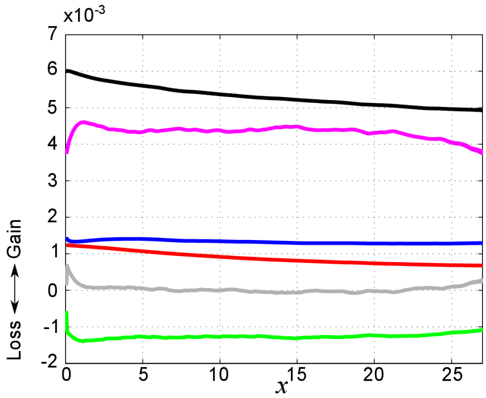

(a)

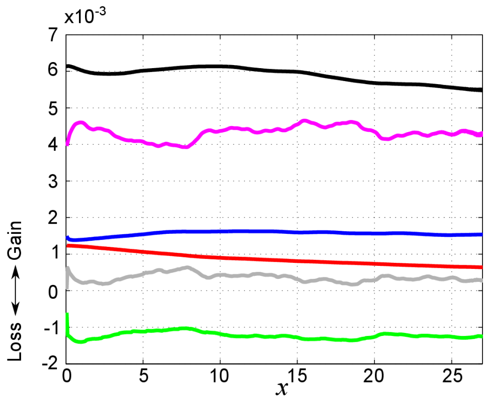

(b)

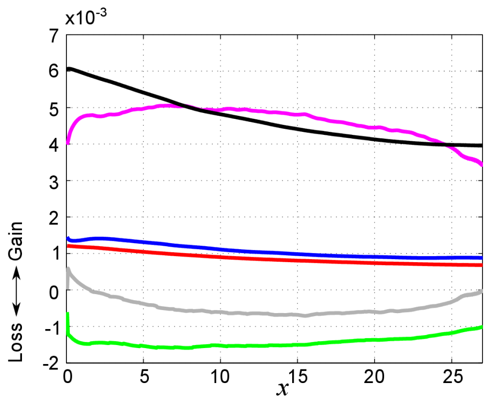

(c)

Figure 5.15: Each term of the FIK identity: (a) no control, (b) $Ri = 0.1$, (c) $Ri = -0.1$. Black, c_f calculated from the mean streamwise velocity gradient on the wall; red, c^{δ}; blue, c^T; green, c^C; magenta, c^D; gray, c^P $(= c_f - c^{\delta} - c^T - c^C - c^D)$.

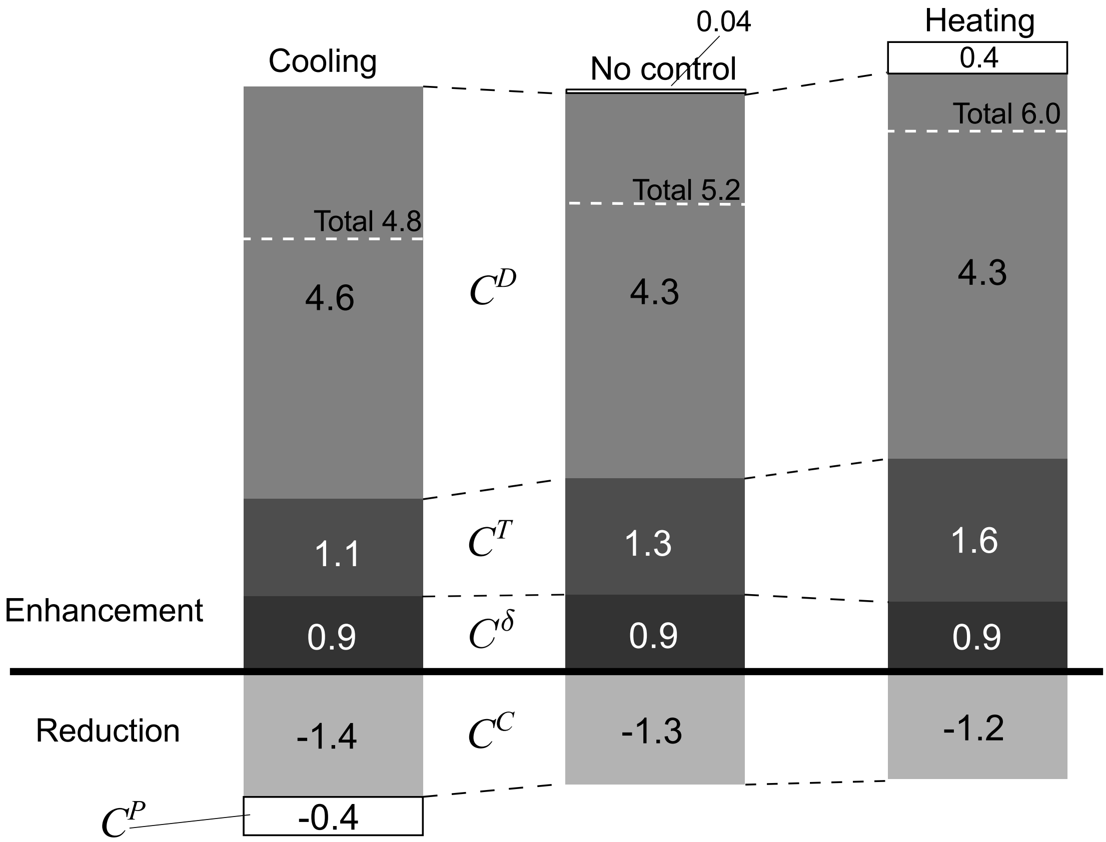

Figure 5.16: Decomposed global friction coefficient by FIK identity ($\times 10^{-3}$).

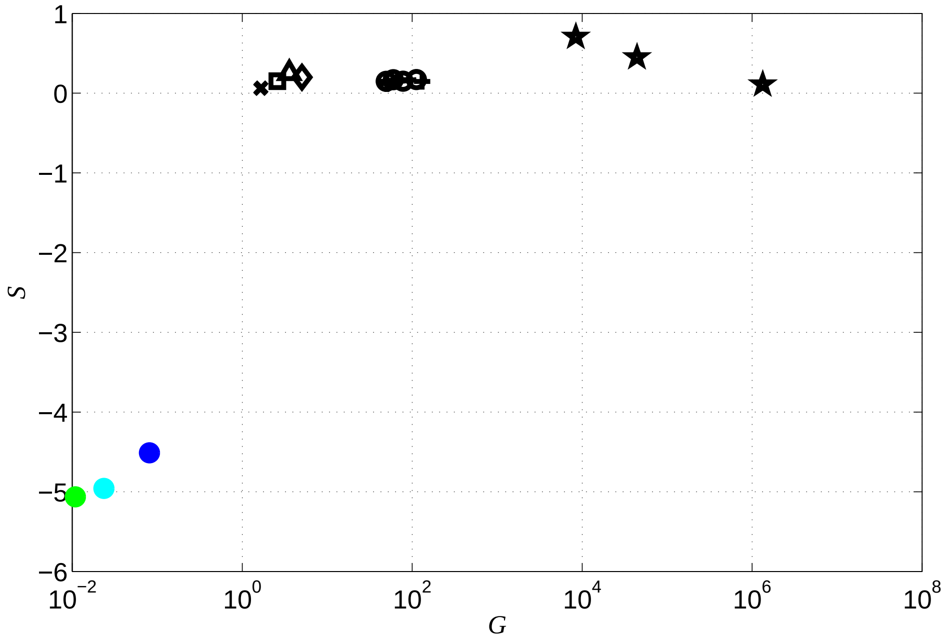

Figure 5.17: Net energy saving rate achieved by different active control schemes: $\star$, uniform blowing in § 4 at a different blowing amplitude; $\circ$, Choi et al. (1994)'s opposition control Choi et al. (1994) (computed by Iwamoto et al., 2002) at different Reynolds numbers ; $+$, Lee et al. (1998) (Iwamoto et al., 2002); $\times$, temporally-periodic spanwise wall-oscillation (Quadrio and Ricco, 2004); $\diamondsuit$, streamwise traveling wave (Min et al., 2006); $\square$, steady streamwise forcing (Xu et al., 2007); $\triangle$, spatially-periodic spanwise oscillation (Yakeno et al., 2009). Solid circle markers denote UC in the present simulation: green, $Ri = -0.01$; light blue, $Ri = -0.02$; blue, 0.1% $Ri = -0.1$.

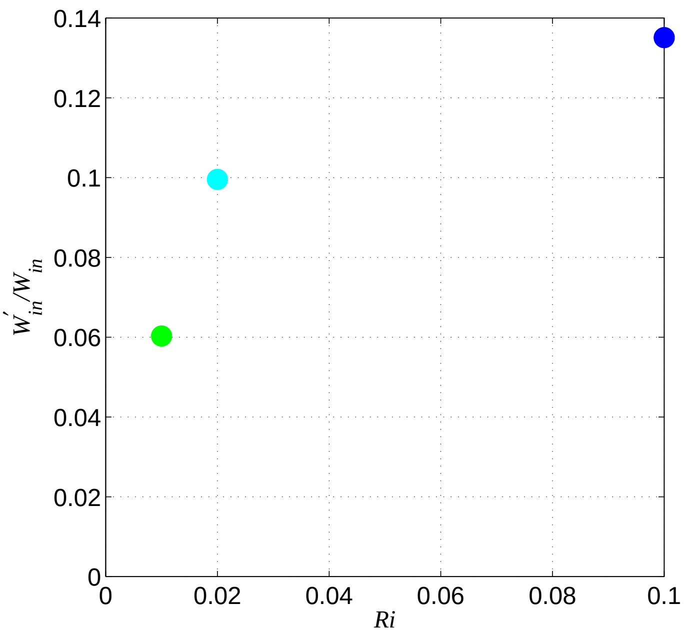

Figure 5.18: The power conversion ratio, W'_{in}/W_{in}.

Chapter 6

Summary and conclusions

A series of direct numerical simulation of skin friction drag reduction control in the incompressible spatially developing turbulent boundary layer is presented. The friction Reynolds number at the inlet was set to be $Re_\tau \approx 160$. As a control method, the uniform blowing/suction and heating/cooling were chosen to examine respectively. Here, the important findings and major contributions of the present study is summarized.

6.1 Achievements and findings

6.1.1 Uniform blowing/suction

Skin friction drag reduction was achieved by the uniform blowing (UB) from the wall, while its enhancement was achieved by uniform suction (US). The UB reduces the viscous shear stress near the wall and enhances the Reynolds shear stress (RSS) away from the wall, while the US has opposite trends. By the decomposition of the skin friction drag, the important factor of the drag reduction is enhanced mean convection term which works for reducing factor in the boundary layers. The effect of the enhancement of mean convection term overwhelmed the increase of the Reynolds shear stress. On the other hand, by the uniform suction, the mean convection term is weakened and turned into the positive value by the induced mass flux, i.e., enhancement factor of the skin friction. Due to this effect, although the Reynolds shear stress is suppressed by the suction, the skin friction is enhanced. The skin friction drag reduction by mass flux from the wall indicates different control strategies from those numerically examined in internal flows, i.e., drag reduction by suppressing RSS. With 1% of the blowing velocity, about 70% of drag reduction was achieved. Although the input is simple and classic, the UB achieved the higher gain net energy-saving rate than other methods examined in internal flows. In this thesis, the higher amplitude of blowing achieves higher net energy saving rate, while weaker blowing achieve higher gain.

6.1.2 Uniform heating/cooling

Skin friction drag reduction was achieved by the uniform cooling (UC) on the wall, while its enhancement was achieved by the heating (UH). The US reduces the both VSS and RSS, while the UH has enhances both. This tendency is similar to the skin friction drag reduction in the internal flows, viz., the skin friction drag reduction by suppressing turbulence near the wall. Moreover, the pressure gradient caused by the buoyancy can not be omitted. Due to the adverse pressure gradient reduces the skin friction drag in cooling cases, while favorable pressure gradient enhances friction drag in heating cases.

The US generates the stable stratification by the buoyancy directed to wall and the turbulence near the wall is reduced. On the other hand, the uniform heating makes unstable stratification and the turbulence near the wall are enhanced. Setting Richardson numbers at $Ri = -0.1$, the around 60% of drag reduction was achieved.

Although it can achieve the skin friction drag reduction, the net energy-saving by the uniform cooling is hopeless to realize. From the control efficiency analysis, it is found to be impossible to convert entire heat input into the buoyancy. In present research, it was concluded that skin friction drag reduction by UC is not effective.

6.2 Conclusion

In this thesis, skin friction drag reduction was achieved by uniform blowing and cooling, respectively. As for the efficiency of the control, only uniform blowing was achieved net energy-saving rate and gain. For the practical issue, the uniform blowing is supposed to be possible to apply to the practical applications.

6.3 Direction for future research

It is found that the uniform blowing can reduce the skin friction drag by the incompressible direct numerical simulation at low Reynolds number. To consider the application of the uniform blowing, the following issues are inevitable to investigate;

1. The investigation in the high Reynolds number flow is necessary. It is known that the turbulent structures in high Reynolds number turbulence like around transports is different from that in the low Reynolds number one(a series works of Marusic; Marusic 2001; Marusic and Kunkel 2003; Marusic et al. 2010a,b) and the control effect on such structures are still unknown. The investigation with DNS is desirable because physical effects of turbulent models themselves and effects of controls on the flow are difficult to separate.

2. The experimental approaches is necessary to realize the uniform blowing in practical applications. The uniform blowing performed in the present thesis is done with the ideal conditions; the wall-normal velocity on the wall applied uniformly and the no-slip condition is applied to the streamwise velocity. Although these conditions can not be achieved perfectly, the blowing devices is possible to work for drag reduction. The preliminary experiment of the uniform blowing was performed as shown in appendix A.

3. The dependency of the skin friction drag reduction on the Mach numbers need to be investigated. The compressibility appears at $Ma \approx 0.3$. The new type bullet trains; a Linear Shinkansen being developed in Japan now travels at 500 km/h, i.e., the Mach number reaches 0.4. The preliminary DNS of the compressible STBL with the uniform blowing was done as shown in appendix B.

Bibliography

Abe, H., Kawamura, H., Matsuo, Y., 2004. Surface heat-flux fluctuations in a turbulent channel flow up to $Re_\tau = 1020$ with $Pr = 0.025$ and 0.71 . Int. J. Heat Fluid Flow 25, 404–419.

Adams, N. A., 1998. Direct numerical simulation of turbulent compression ramp flow. Theor. Comput. Fluid Dyn. 12, 109–129.

Bagheri, S., Brandt, L., Henningson, D. S., 2003. Input-output analysis, model reduction and control of the flat-plate boundary layer. J. Fluid Mech. 478, 11–34.

Banister, D., Anderton, K., MBonilla, D. Givoni, M., Schwanen, T., 2011. Transportation and the environment. Annu. Rev. Environ. Resour. 36, 247–270.

Bellettre, J., Bataille, F., Rodet, J. C. Lallemand, A., 2000. Thermal behaviour of porous plate subjected to air blowing. AIAA J. 14, 523–532.

Bewley, T. R., 1999. Optimal and robust control and estiation of transition, convection, and turbbulence. Ph.D. thesis, Stanford University.

Bewley, T. R., 2009. A fundamental limit on the balance of power in a transpiration-controlled channel flow. J. Fluid Mech. 632, 443–446.

Bradshaw, P., 1978. Topic in applied physics 12 Turbulence. Springer Verlag.

Brillant, G., Bataille, F., Ducros, F., 2004. Large eddy simulation of a turbulent boundary layer with blowing. Theor. Comput. Fluid Dyn. 17, 433–443.

Choi, H., Jeon, W. P., Kim, J., 2008. Control of flow over a bluff body. Annu. Rev. Fluid Mech. 40, 113–139.

Choi, H., Moin, P., Kim, J., 1994. Active turbulence control for drag reduction in wall-bounded turbulence. J. Fluid Mech. 262, 75–110.

Coleman, G. N., Kim, J., Moser, R. D., 1995. A numerical study of turbulent supersonic isothermal-wall channel flow. J. Fluid Mech. 305, 159–183.

Deadorff, J. W., 1970. A numerical study of 3 dimensional turbulent channel flow at large Reynolds numbers. J. Fluid Mech. 41, 453–480.

Desjardins, O., Blanquart, G., Balarac, G., Pitsch, H., 2008. High order conservative finite difference scheme for variable density low Mach number turbulent flows. J. Comput. Phys. 227, 7125–7159.

Dukowicz, J. K., Dvinsky, A. S., 1992. Approximate factorization as a higer order splitting for impricit imcompressible equations. J. Comput. Phys. 102, 336–347.

Frohnapfel, B., Hasegawa, Y., Quadrio, M., 2012. Money versus time: evaluation of flow control in termas of energy consumption and convinience. J. Fluid Mech. 700, 406–418.

Fukagata, K., Iwamoto, K., Kasagi, N., 2002a. Contribution of Reynolds stress distribution to the skin friction in wall-bounded flows. Phys. Fluids 14, L73–L76.

Fukagata, K., Kasagi, N., 2002b. Highly energy-conservative finite difference method for the cylindrical coordinate system. J. Comput. Phys. 181, 478–498.

Fukagata, K., Kasagi, N., Koumoutsakos, P., 2006. A theoretical prediction of friction drag reduction in turbulent flow by superhydrophobic surfaces. Phys. Fluids 18.

Fukagata, K., Sugiyama, K., Kasagi, N., 2009. On the lower bound of net driving power in controlled duct flows. Physica D 238, 1082–1086.

Gad-el Hak, M., 1996. Modern development in flow control. Vol. 49. Cambridge press.

Ganapathisubramani, B., Longmire, E., Marusic, I., 2003. Characteristics of vortex packets in turbulent boundary layers. J. Fluid Mech. 478, 35–46.

Garcia-Mayoral, R., Jiménez, J., 2011. Drag reduction by riblets. Phil. Trans. R. Soc. A 369, 1412–1427.

Gomez, T., Flutet, V., Sagaut, P., 2009. Contribution of Reynolds stress distribution to the skin friction in compressible turbulent channel flows. Phys. Rev. E 79.

Ham, F. E., Lien, F. S., Strong, A. B., 2002. A fully conservative second-order finite difference scheme for incompressible flow on nonuniform grids. J. Comput. Phys. 177, 117–133.

Hamilton, J. M., Kim, J., Waleffe, F., 1994. Regeneration mechanism of near-turbulence structures. J. Fluid Mech. 287, 317–348.

Harlow, F. H. Welch, J. E., 1965. Numerical calculation of time-dependent viscous incompressible flow of with free surface. Phys. Fluids 8, 2182–2189.

Hattori, H., Houra, T., Nagano, Y., 2007. Direct numerical simulation of stable and unstable turbulent thermal boundary layers. J. Heat Fluid Flow 28, 1262–1271.

Hoyas, S., Jimenez, J., 2006. Scaling of the velocity fluctuations in turbulent channels up to $Re_\tau = 2003$. Phys. Fluids 18, 011702.

Huang, P. G., Coleman, G. N., Bradshaw, P., 1995. Compressible turbulent channel flows: DNS results and modelling. J. Fluid Mech. 305, 185–218.

Hutchins, N., Monty, J. P., Ganapathisubramani, B., Ng, H. C. H., Marusic, I., 2011. Three-dimensional conditional structure of a high-Reynolds-number turbulent boundary layer. J. Fluid Mech. 673, 255–285.

Iida, O., Kasagi, N., 1997. Direct numerical simulation unstratified turbulent channel flow. J. Heat Transfer 119-1, 53–61.

Iida, O., Kasagi, N., 2002. Direct numerical simulation of turbulent channel flow under stable density stratification. Int. Heat Mass Transfer 45-8, 1693–1703.

Iwamoto, K., Fukagata, K., Kasagi, N., Suzuki, 2004. DNS of turbulent channel flow at $Re_\tau = 1160$ and evaluation feedback control at practical Reynolds numbers. In: Proc. 5th Symp. on Smart Control of Turbulence.

Iwamoto, K., Kasagi, N., Suzuki, 2005. Direct numerical simulation of turbulent channel at $Re_\tau = 2320$. In: Proc. 6th Symp. on Smart Control of Turbulence.

Iwamoto, K., Suzuki, Y., Kasagi, N., 2002. Reynolds number effect on wall turbulence: toward effective feedback control. Int. J. Heat Fluid Flow 23, 678–689.

Jimenez, J., Moin, P., 1991. The minimal flow unit in near wall turbulence. J. Fluid Mech. 225, 213–240.

Kajishima, T., 1999a. Finite-difference method for convective terms using nin-uniform grid. Trans. JSME/B 633, 1607–1623 (in Japanese).

Kasagi, N., Hasegawa, Y., Fukagata, K., 2009a. Toward Cost-effective Control of Wall Turbulence for Skin Friction Drag Reduction. In: Proc. 12th EUROMECH European Turbulence Conference.

Kasagi, N., Sumitani, Y., Suzuki, Y., Iida, O., 2004. Kinematics of the quasi-coherent vortical structure in near-wall turbulence. Int. Heat Fluid Flow 16, 2–10.

Kasagi, N., Suzuki, Y., Fukagata, K., 2009b. Microelectromechanical Systems-Based Feedback Control of Turbulence for Skin Friction Reduction. Annu. Rev. Fluid Mech. 41, 231–251.

Kim, J., 2003. Control of turbulent boundary layers. Phys Fluids 15, 1093–1105.

Kim, J., Bewley, T. R., 2007. A linear systems approach to flow control. Annu. Rev. Fluid Mech. 39, 383–417.

Kim, J., Kim, K., Sung, H., 2003. Wall pressure fluctuations in a turbulent boundary layer after blowing or suction. AIAA J. 41, 1697–1704.

Kim, J., Moin, P., Moser, R., 1987. Turbulence statistics in fully-developed channel flow at low Reynolds-number. J. Fluid Mech. 177, 133–166.

Kim, K., Sung, H., 2006. Effects of unsteady blowing through a spanwise slot on a turbulent bounsary layer. J. Fluid Mech. 557, 423–450.

Kim, K., Sung, H. J., Chung, M. K., 2002. Assessment of local blowing and suction in a turbulent boundary layer. AIAA J. 40, 175–177.

Kong, H., Choi, H., Lee, J. S., 2006. Direct numerical simulation of turbulent thermal boundary layers. Phys. Fluids 12, 2555–2568.

Lagha, M., Kim, J., Eldredge, J. D., Zhong, X., 2011a. A numerical study of compressible turbulent boundary layers. Phys. Fluids 23, 015106.

Lagha, M., Kim, J., Eldredge, J. D., Zhong, X., 2011b. Near-wall dynamics of compressible boundary layers. Phys. Fluids 23, 065109.

Lee, C., Kim, J., Choi, H., 1998. Suboptimal control of turbulent channel flow for drag reduction. J. Fluid Mech. 358, 245–258.

Lögdberg, O., Fransson, J. H. M., Alfredson, P. H., 2009. Streamwise evolution of longitudinal vortices in a turbulent boundary layer. J. Fluid Mech. 623, 27–58.

Lund, T. S., Wu, X., Squires, K. D., 1998. Generation of turbulent inflow data for spatially-developing boundary layer simulations. J. Comput. Phys. 140, 233–258.

Mamori, H., Fukagata, K., 2010. Consistent scheme for computation of reynolds stress and turbulent kinetic energy budgets for energy-conservative finite difference method. J. Comput. Sci. Technol. 4, 64–75.

Marusic, I., 2001. On the role of large-scale structures in wall turbulence. Phys. Fluids 13, 735–743.

Marusic, I., Kunkel, G. J., 2003. Streamwise turbulence intensity formulation for flat-plate boundary layers. Phys. Fluids 15, 2461–2464.

Marusic, I., Mathis, R., Hutchins, N., 2010a. High Reynolds number effects in wall turbulence. Int. J. Heat Fluid Flow 31, 418–428.

Marusic, I., Mathis, R., Hutchins, N., 2010b. Predictive Model for Wall-Bounded Turbulent Flow. Science 329, 193–196.

Min, T., Kang, S. M., Speyer, J. L., Kim, J., 2006. Sustained sub-laminar drag in a fully developed channel flow. J. Fluid Mech. 558, 309–318.

Miyauchi, T., Tanahashi, M., Suzuki, M., 1996. Inflow and outflow boundary conditions for direct numerical simulations. JSME Int. J. Ser. B 39, 305–314.

Monty, J. P., Hutchins, N., Ng, H. C. H., Marusic, I., Chong, M. S., 2009. A comparison of turbulent pipe, channel and boundary layer flows. J. Fluid Mech. 632, 431–442.

Morinishi, Y., Lund, T., Vasilyev, O., Moin, P., 1998. Fully conservative higher order finite difference schemes for incompressible flow. J. Comput. Phys. 143, 90–124.

Morinishi, Y., Tamano, S., Nakabayashi, K., 2004. Direct numerical simulation of compressible turbulent channel flow between adiabatic and isothermal walls. J. Fluid Mech. 502, 273–308.

Moser, R. D., Kim, J., Mansour, N. N., 1999. Direct numerical simulation of turbulent channel flow up to $Re_\tau = 590$. Phys. Fluids 11, 943–945.

Nakanishi, R., Mamori, H., Fukagata, K., 2012. Relaminalization of turbulent channel flow using traveling wave-like wall deformation. Int. J. Heat Fluid Flow 35, 152–159.

Nikitin, N., 2006. Finite difference method for incompressible navier Stokes equations in arbitrary . J. Comput. Phys. 217, 759–791.

Pamiès, M., Garnier, E., Merlen, A., Sagaut, P., 2007. Response of a spatially developing turbulent boundary layer to active control strategies in the framework of opposition control. Phys. Fluids 19, 108102.

Park, J., Choi, H., 1999. Effects of uniform blowing or suction from a spanwise slot on a turbulent boundary layer flow. Phys. Fluids 11, 3095–3105.

Peet, Y., Sagaut, P., 2009. Theoretical prediction of turbulent skin friction on geometrically complex surfaces. Phys. Fluids 21, 105105.

Piacsek, S. A., Williams, G. P., 1970. Conservation propaties of convection difference scheme. J. Comput. Phys. 6, 392–405.

Quadrio, M., Ricco, P., 2004. Critical assessment of turbulent drag reduction through spanwise wall oscillations. J. Fluid Mech. 521, 251–271.

Reynolds, O., 1895. On the dynamizal theory of incompressible viscous fluids and the determination of the ctriterion. Philos. Trans. R. Soc. Ser. A. 186, 123–164.

Robinson, S. K., 1991. Coherent motions in the turbulent boundary layer. Annu. Rev. Fluid Mech. 23, 601–639.

Scherader, L., Brandt, L., Henningson, D. S., 2009. Receptivity mechanisms in three-dimensional boundary layers. J. Fluid Mech. 618, 209–241.

Schlatter, P., Örlü, R., 2010. Assesment of direct numerical simualation data of turbulent boundary layers. J. Fluid Mech. 659, 116–126.

Schumann, U., 1975. Subgrid scale model model for finite difference simulation of turbulent flows in plane channels and annuli. J. Comput. Phys. 18, 376–404.

Simpson, R. L., Moffat, R. J., Kays, W. M., 1969. The turbulent boundary layer on a porous plate: experimental skin friction with variable injection and suction. Int. J. Heat Mass Transfer 12, 771–789.

Smagorinsky, J., 1963. General circulation experiments with the primitive equations. Mon. Wheather Rev. 91, 99–164.

Smith, C. R., Metzler, S. P., 1983. The characteristics of low-speed streaks in near -wall region of a turbulent boundary layer. J. Fluid Mech. 129, 27–54.

Spalart, P. R., Moser, R. D., Rogers, M. M., 1991. Spectral methods for the Navier-Stokes equations with one inifinite and 2 periodic directions. J. Comput. Phys. 96, 297–324.

Stevenson, T. N., 1963. A law of the wall for turbulent boundary layers with suction and injection. Aero. Rep. 166. Cranfield College.

Sumitani, Y., Kasagi, N., 1995. Direct Numerical-simulation of turbulent transport with uniform wall injection and suction. AIAA J. 33, 1220–1228.

Vigdorovich, I. I., 2005. Turbulent boundary layer over a flat plate with uniform wall suction. J. Exp. Theor. Phys. 101, 741–759.

White, C. M., Mungal, M. G., 2008. Mechanics and prediction of turbulent drag reduction with polymer additives. Annu. Rev. Fluid Mech. 40, 235–256.

White, F. M., 2005. Fluid Mechanics, 5th Edition. Mc Graw Hill.

Wu, X., Moin, P., 2009. Direct numerical simulation of turbulence in a nominally zero-pressure-gradient flat-plate boundary layer. J. Fluid Mech. 630, 5–41.

Xu, J., Dong, S., Maxey, M. R., Karniadakis, G. E., 2007. Turbulent drag reduction by constant near-wall forcing. J. Fluid Mech. 582, 79–101.

Yakeno, A., Hasegawa, Y., Kasagi, N., 2009. In: Proc. 6th symp. on turbulence and shear flow phenomena.

Appendix A

Preliminary wind-tunnel experiments of drag reduction by uniform blowing

A.1 Motivation

By the direct numerical simulation of the spatial developing turbulent boundary layer with uniform blowing, the possibility of the skin friction drag reduction was found. Although it achieved drag reduction, a uniform blowing device is considered difficult to fabricate in practice. In this study, measurements of streamwise and wall-normal velocity components are performed with single and dual sensor hotwire anemometry.

This experimental work was supported by Japan Aerospace Exploration Agency (JAXA). The measurement was performed in the low disturbance the wind tunnel of the Aviation Program Group at Chofu Aerospace Center, JAXA.

A.2 Experimental apparatus

A.2.1 Making turbulent boundary layer

To make a spatially developing turbulent boundary layer, a flat plate for the transition region was prepared in the upstream region of blowing device, as shown Fig. A.1. The boundary layer starts to form at the upstream edge of the plate. To make the boundary layer into turbulent one, a sandpaper (#60) whose streamwise length is 200 mm is attached in the upstream region as shown in Figs. A.1 (a) and (b). The upstream

Table A.1: Flow condition in wind tunnel

U^*_∞	9 m/s
99% boundary layer thickness at $x = 0$ mm, δ^*_0	40 mm
Kinematic viscosity, ν^*	1.5×10^{-5} m^2/s
Friction velocity, u^*_τ	0.032 m/s
Friction Reynolds number at $x = -50$ mm, $Re_{\tau,0}$	1100

plate for the turbulent transition and the blowing device are bridged by a thin plate to avoid a blockage caused by the blowing device located downstream. The origin of the coordinates is located on the upstream edge of the blowing device, i.e., -800 mm $\leq x^* \leq 0$ mm is on the solid plate and 0 mm $\leq x^* \leq 595$ mm is on the blowing device.

A.2.2 Hotwire anemometry (HWA)

The measurements of the streamwise and wall-normal velocities are performed by using I-type and X-type hotwire probes (Dantec 55P01 and 55P63, respectively). The calibration of signals from the HWA sensors was performed by a resolution of 1 m/s between 1 m/s and 10 m/s. The resolution of angles was 4.2 degree, covering from -42 to 42 degrees with respect to the free stream direction. The relationship among the voltage obtained by sensors, the angle of attack (AOA), and the velocity is expressed by a polynomial equation. A fifth-order polynomial equation was used to fit the curves of the velocity on the plane of the voltages obtained from a pair of X-wire sensors. The conditions of the oncoming flow measured at $x^* = -50$ mm are listed in Table A.1. The diameter and length of the sensor are 5 μm and 1.25 mm, respectively. The distance between each wire is 1mm. In this experiment, the statistics were calculated from 240,000 samples with a sampling rate of 20 kHz and a sampling time of 120 seconds.

A.2.3 Blowing device

Blowing from the wall is performed by the blowing plate manufactured by the Seika industry shown in Fig. A.1(c). The size of the blowing plate is shown in Fig. A.2.

The streamwise length and the spanwise width of the blowing area are 595 mm and 395 mm, respectively. The depth of the air-chamber is 40 mm and the volume of the air-chamber for blowing is 9.4×10^{-3} m^3. As shown in Fig. A.3, the holes of 1mm-diameter are prepunched on the stainless-steel (SUS) plate with the pitch of 2 mm. The air for blowing is supplied by a gust blower (US2-40T) of the Showa Denki Co., LTD. with an inverter. The air-chamber of the blowing device and the gust blower are connected each other by a 40mm-diameter-pipe.

A.2.4 Decision of the blowing amplitude

The input amplitude of the gust blower was fixed by checking the relationship between the input frequency of the inverter and the output blowing velocity on the wall. The velocity of the blown air was measured by I-type HW sensor without free-stream flow. Due to a limitation of the traversing device of the probe, the profiles are obtained only in the streamwise direction on the centerline of the blowing device. In the present experiment, the uniformity of the blowing was not checked. The target blowing velocity in the present experiment is 1% of the free-stream velocity, i.e., 0.09 m/s. Figures A.4 (a) and (b) show the mean blowing velocity and the root-mean-square of velocity fluctuations, respectively. It is found that the blowing amplitude achieved over 2 m/s at 100 Hz of the motor-input as a maximum one. With the minimum motor-input, 10 Hz, the blowing velocity unnaturally decreased due to the heat from the gust blower. The blowing fluctuations shown in Fig. A.4 (b) indicates that the fluctuation intensity is less than 0.2% of the blowing velocity around 20 Hz of the motor-input. The blowing velocity is comparably uniform in the streamwise direction. Due to the conditions mentioned above, the motor-input was fixed at 20 Hz in the present experiment.

A.2.5 Uncertainty

The uncertainty of the HW measurement was evaluated by 300 second-measurement at $y^* = 1$ mm on the blowing device without blowing. Figures A.5 (a) and (b) show the uncertainty in the mean velocity and the 2nd order statistics, respectively. In the measurement during 150 seconds, it is found that the mean streamwise and wall-normal velocities contained less than 0.5% and 2% of random errors, respectively, as shown in Fig. A.5(a). Figure A.5(b) indicates that, in the measurement during 150 seconds, the

Table A.2: Displacement of the wall-normal traverse by the stepping motor

Displacement [mm]	Pulse	Displacement / Pulse [μm / pulse]
1.00	248	4.032
2.00	497	4.024
3.00	745	4.027
4.00	995	4.020
5.00	1244	4.019
6.00	1495	4.013
7.00	1743	4.016
8.00	1991	4.018
9.00	2239	4.020

2nd order statistics: $\overline{u'u'}$, $\overline{v'v'}$, and $\overline{u'v'}$ contained less than 1% of random errors. The sampling time for the present experiment, i.e., 120 seconds, are appropriate to avoid large random errors. Figure A.6 shows the number of samples in the measurement during 120 seconds at $y^* = 1$ mm as a function of the angle of attack, ϕ, without blowing and with blowing, respectively. Without blowing, all data are in the range of -42 deg $\leq \phi \leq 42$ deg, which is the same as that for the calibration of the sensors. On the other hand, with blowing, the distribution of the data is wider than that without blowing and some data were out of the range of the calibration.

Uncertainty of the traversing system in wall-normal directions is the calculated from data obtained with a dial gauge, of which specification is shown in Table A.2. The data were given by the Aviation Program Group (APG) of JAXA. From Table A.2, we get the displacement due to a unit pulse of the motor, d^*_{pulse}, as

$$d^*_{\text{pulse}} = (4.02 \pm 0.58) \times 10^{-3} \text{ mm/pulse}. \tag{A.1}$$

A.3 Results and Discussion

A.3.1 Primary remarks

The velocity profiles across the shear layer were measured at different streamwise locations, $x^* = -250$ mm, -50 mm, 150 mm, and 350 mm. The probe was traversed from the vicinity of the wall to the main stream. The nearest distance from the wall was assumed $y^* = 1$ mm due to the height of the prong of the sensor.

The inlet profile was measured at $x^* = -50$ mm by the I-type HW as shown in Fig. A.8. It is found that the profile collapses on the linear-law and log-law profiles, respectively. The oncoming flow is supposed to be a turbulent boundary layer. From the result, the 99% boundary layer thickness was $\delta_0^* = 40$ mm and the friction velocity was 0.032 m/s, as shown in Table A.1. The friction Reynolds number was calculated as $Re_{\tau,0} \approx 1100$.

In order to compare the results of the present experiments with those of DNS, evaluation of the pressure gradient on the wall is important. The pressure gradient was measured by a Pitot-tube on the plate, of which results are shown in Fig. A.7. It is found that, although the pressure gradient was increased at the upstream edge, the pressure drop was much smaller than the wall shear stress at the inlet (less than 5%).

A.3.2 Statistics

The mean streamwise velocity is shown in Fig. A.9 (a). Development of the boundary layer thickness is found between $x^* = -150$ mm and -50 mm. At $x^* = 150$ on the blowing device, acceleration of mean streamwise velocity due to the punched holes is confirmed. On the blowing plate, the no-slip condition for the streamwise velocity is no longer appropriate; slip on the holes has to be considered. A depth of the holes, viz., the thickness of aluminum plate between air-chamber and main flow, is $t_p^* = 1.2$ mm. By non-dimensionalization with the wall units at the inlet, the thickness reaches $t_p^{+0} \approx 30$, which is equivalent to the height of buffer layers. With uniform blowing, the profiles are shifted away from the wall compared to the case without blowing.

The wall-normal mean velocity shown in Fig. A.9 (b) indicates that the wall-normal velocity is 2% of the main stream velocity. By the blowing, at the blowing are enhanced $x^* = 150$ mm. At $x^* = 450$ mm, however, the mean velocity in blowing case seems to decelerate in the streamwise direction near the wall. In present experiment, the uniformity of the blowing is unknown and it possibly occurred by the local suction on the blowing wall. Near the wall, also, unnatural acceleration appears on the blowing device. This is likely an artifact due to the heat of the air coming from the gust blower. Namely, the signal of the voltage was overestimated due to the heat.

The effect on the turbulence intensities is shown in Fig. A.10 (a). It is found that blowing enhances the velocity fluctuations. Furthermore, the Reynolds shear stresses (RSS) shown in Fig. A.10 (b) indicates that RSS is increased by the blowing. Although these trends similar to those in the result of DNS, the peak of profiles seems to locate lower than that in upstream flow. This seems to be due to the velocity slip on the wall, unlike the ideal control input assumed in DNS. Above the holes of the plate, the velocity fluctuations do not vanish on the solid wall.

A.3.3 Power spectral density

In order to investigate the effect of the blowing to the turbulent scales, the spectral analysis was performed. The power spectral density (PSD) of the turbulent fluctuation in the srtreamwise, Φ_{uu}, and wall-normal,Φ_{vv}, directions is shown in Fig. A.11 and A.12. It is found that blowing enhances the turbulent fluctuation. The figure shows that a certain frequency is strongly enhanced in the boundary layer. This trends also appears in the cross-spectra of Φ_{uv} shown in Fig. A.13. The one-dimensional profiles at $y^* = 1$ mm are picked up in Fig. A.14 to clearly see the PSD profiles. Turbulent fluctuations, especially the streamwise component, were all enhanced by the blowing. In Fig. A.14(a), the peak is found at the certain frequency where the wavelength is equivalent to the boundary layer thickness. The enhancement of turbulent intensities is similar to that found in the numerical simulation in Chap. 4.

A.3.4 Momentum thickness and skin friction

The calculated momentum thickness is shown in Fig. A.15. The spatial development of the boundary layer is confirmed in more upstream region than -150 mm $\leq x^* \leq -50$ mm. In the downstream region on the blowing plate, the momentum thickness decreases drastically because of the holes on the blowing plate. The transpiration through the boundary of the blowing plate should be considered. The exact measurement of skin friction is still left future work.

A.4 Closure

The velocity measurement in turbulent boundary layer by using the X-type HWA with blowing is performed. The shift of mean streamwise velocity profiles away form the wall and the enhancement of the turbulence similarly to the numerical simulation in Chap. 4 were confirmed. The peak locations of the velocity fluctuations are found to be much closer to the wall, possibly because the hole of the blowing plate breaks no-slip conditions. In the present experiment, the skin friction drag on the blowing device could not be determined and it is left for a future work.

(a)

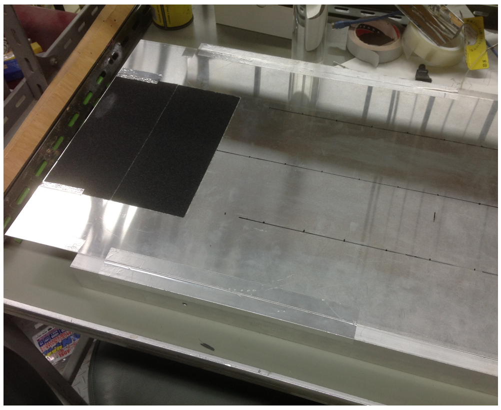

(b)

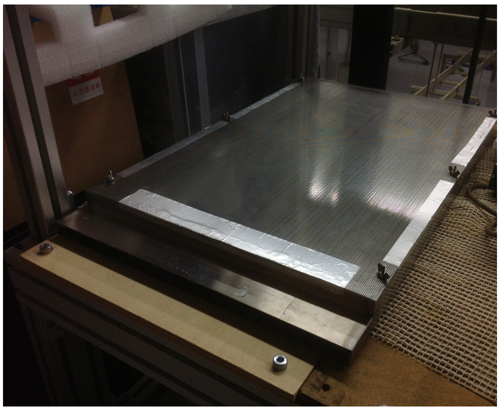

(c)

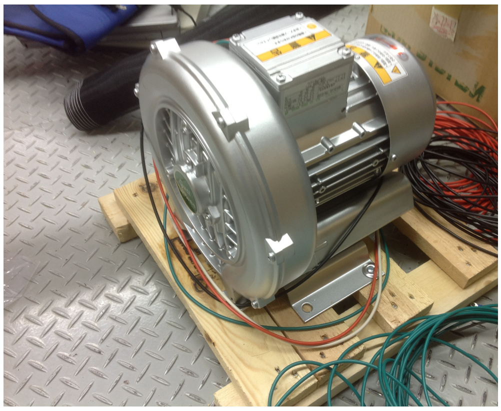

(d)

Figure A.1: The blowing device used in present work: a) overview; b) transition zone plate; c) blowing plate; d) gust blower.

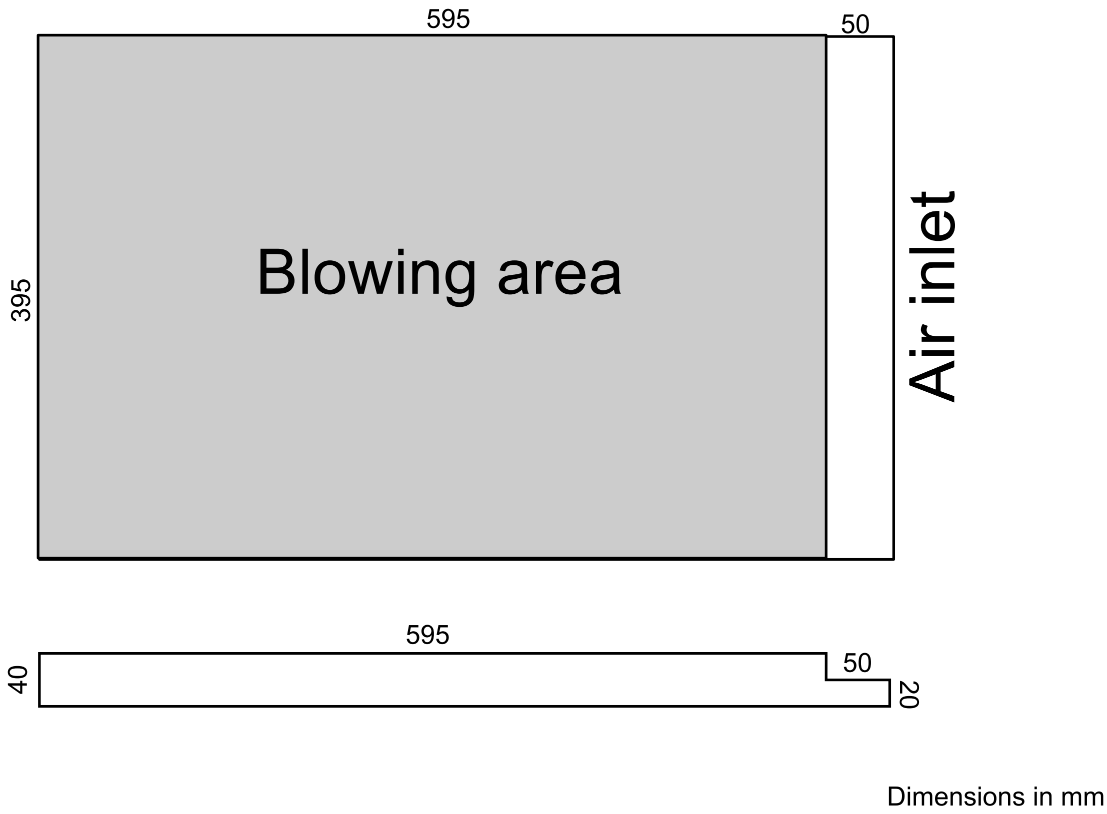

Figure A.2: Size of the blowing plate.

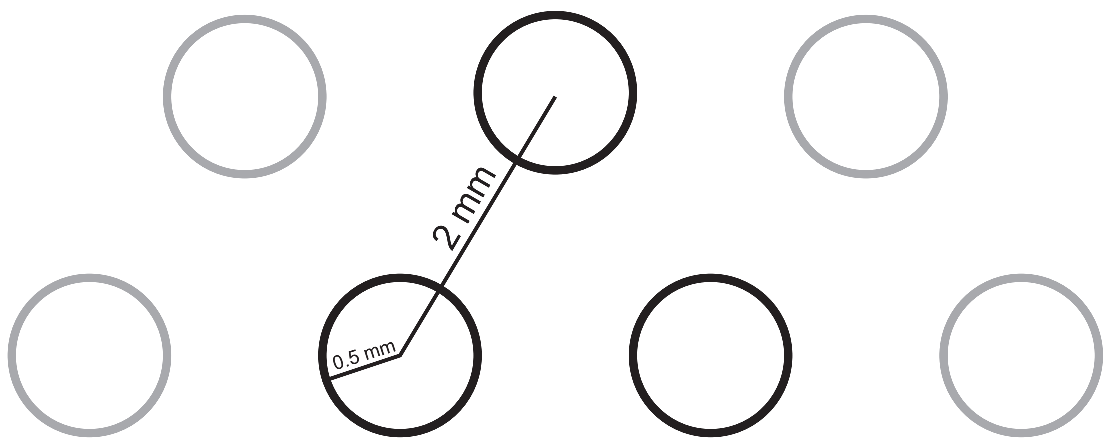

Figure A.3: Size of the punched hole on the blowing plate.

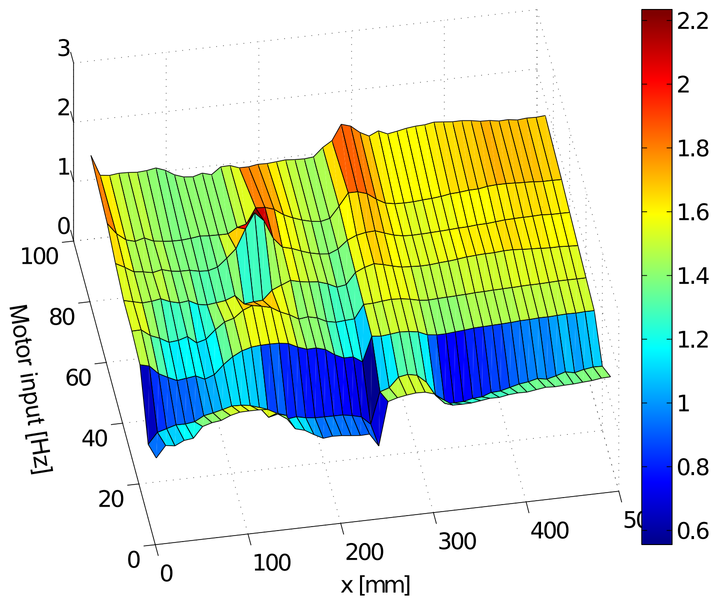

(a)

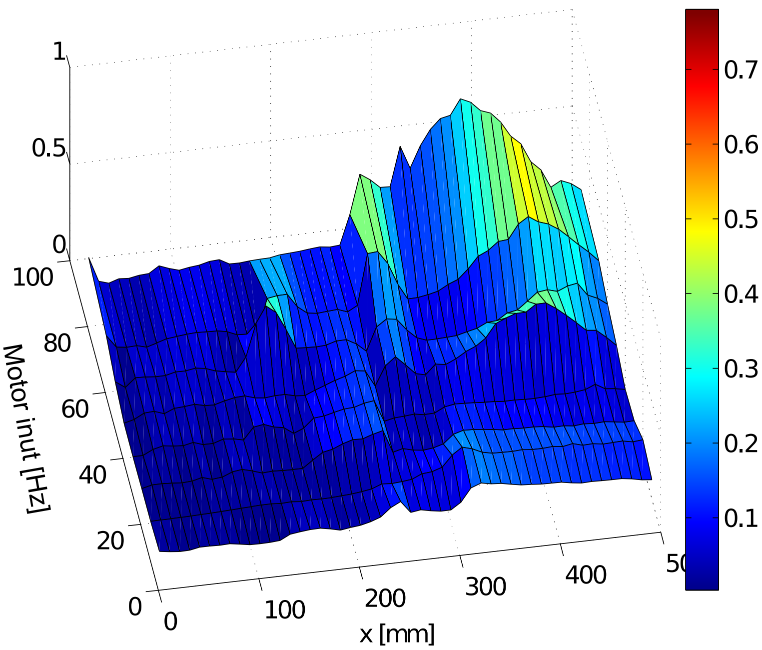

(b)

Figure A.4: Blowing velocity profile measured by I-type HW without free-stream: a) wall-normal mean velocity; b) root-mean-square of the velocity fluctuations.

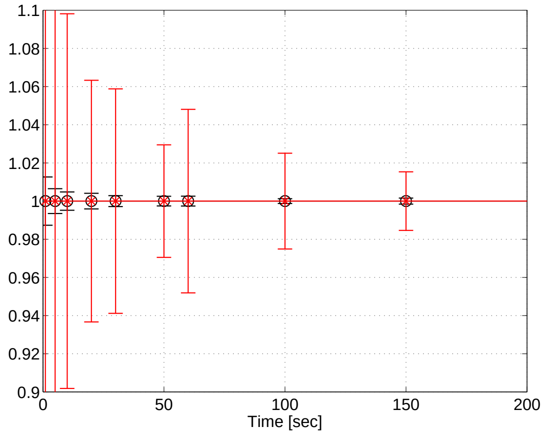

(a)

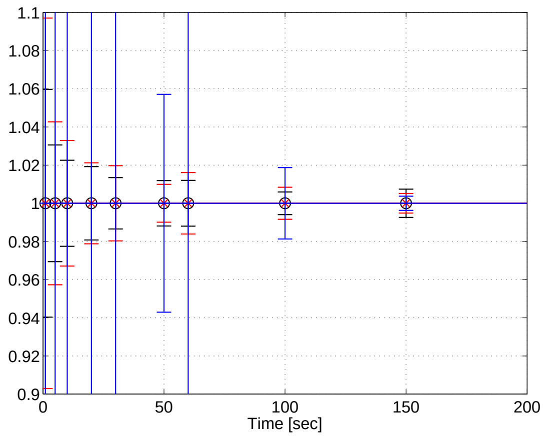

(b)

Figure A.5: A typical graph for checking the random error as a function of the number of samples. a) Mean velocity: black, streamwise velocity; red, wall-normal velocity. b) 2nd order statistics: black, streamwise fluctuations; red wall-normal fluctuations; blue, Reynolds shear stress.

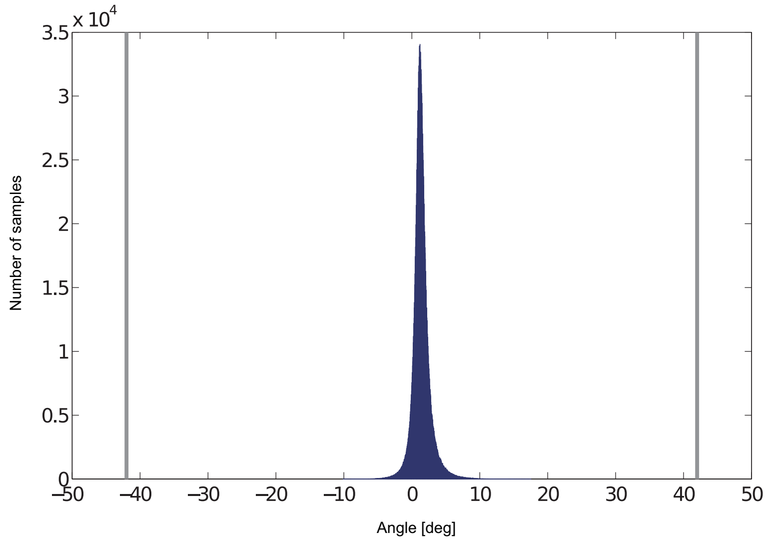

(a)

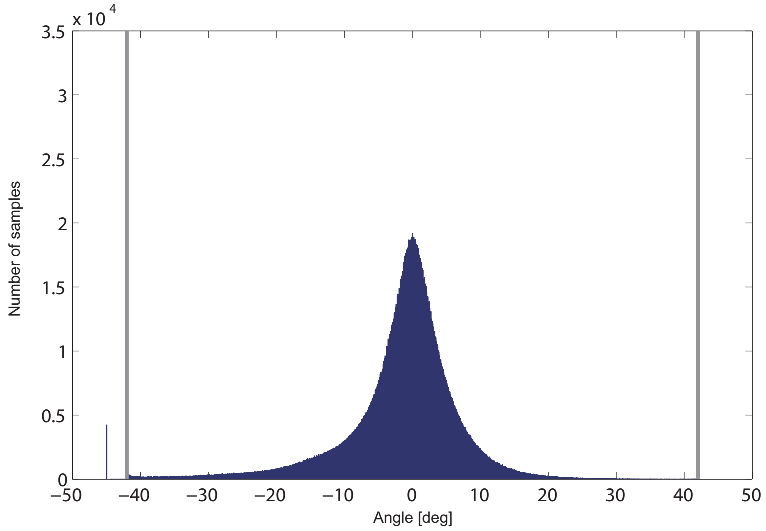

(b)

Figure A.6: The number of samples as a function of the angle of attack at $y = 1$ mm: a) without blowing; b) with blowing.

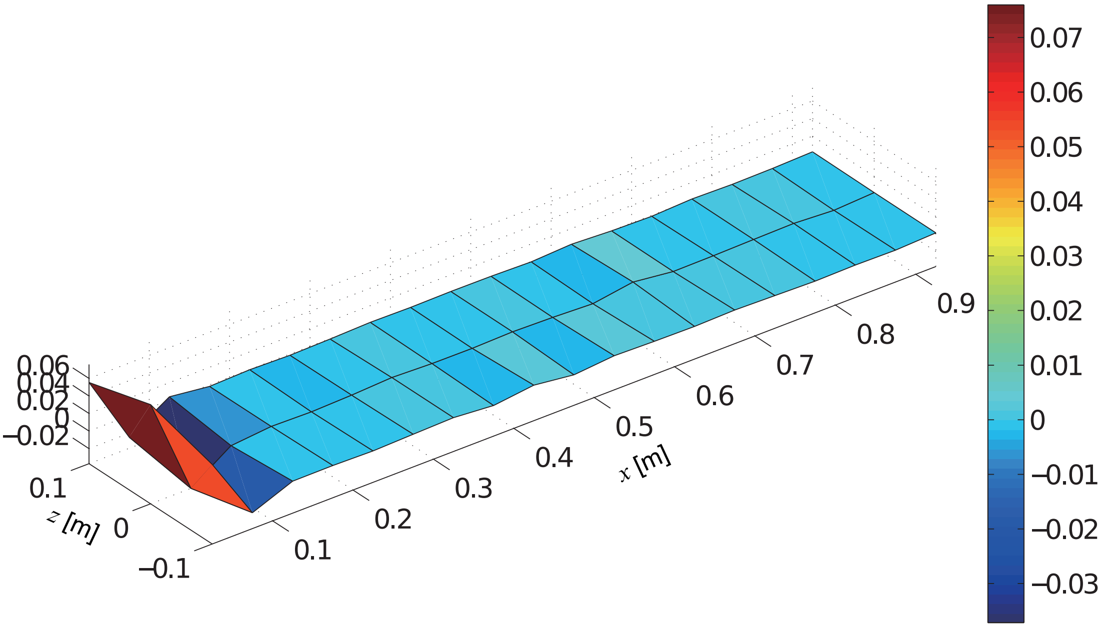

Figure A.7: Streamwise pressure gradient on the blowing plate.

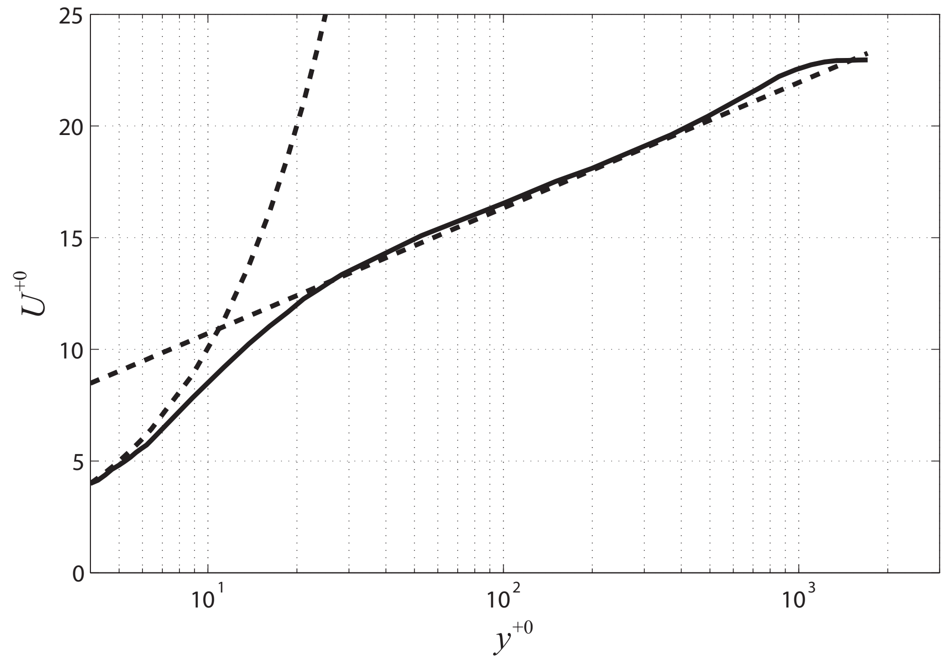

Figure A.8: Inlet profile of mean streamwise velocity

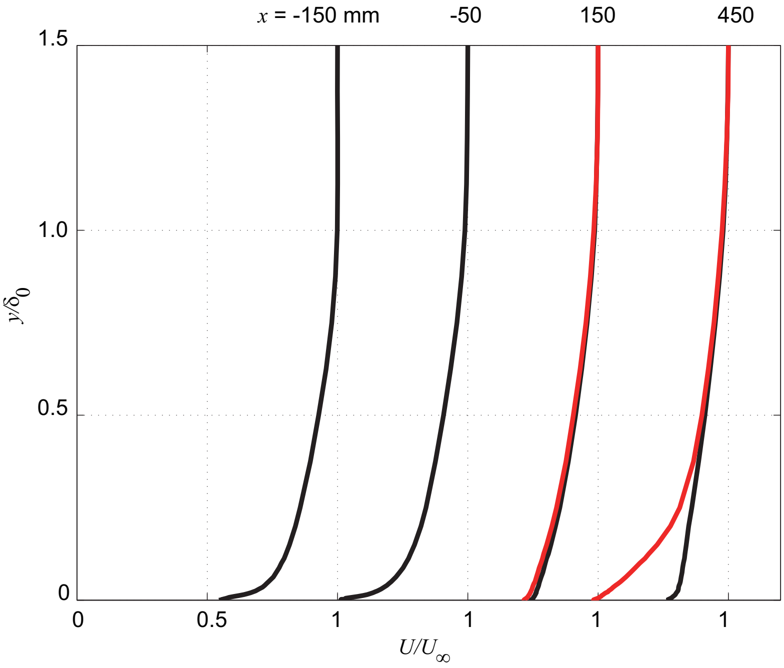

(a)

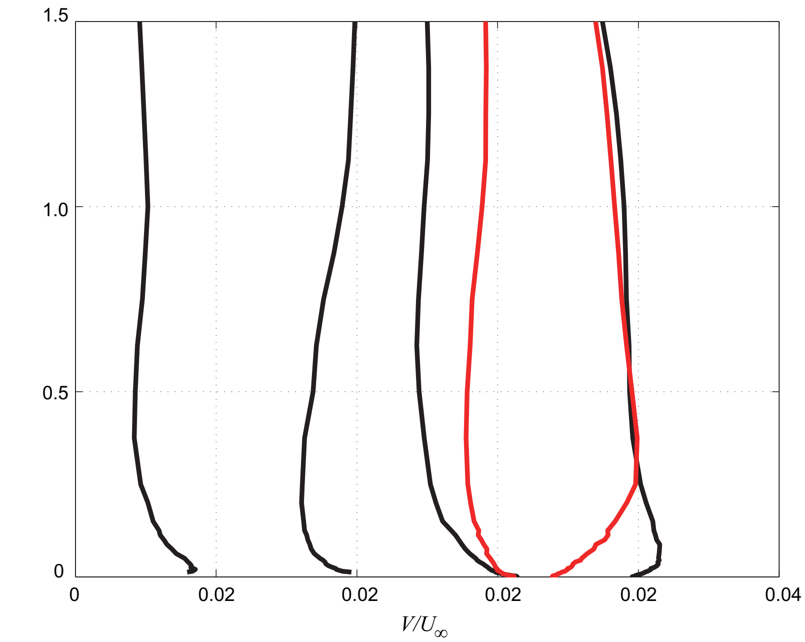

(b)

Figure A.9: Mean velocity profiles: a) streamwise velocity; b) wall-normal. Black, without blowing; red, with blowing.

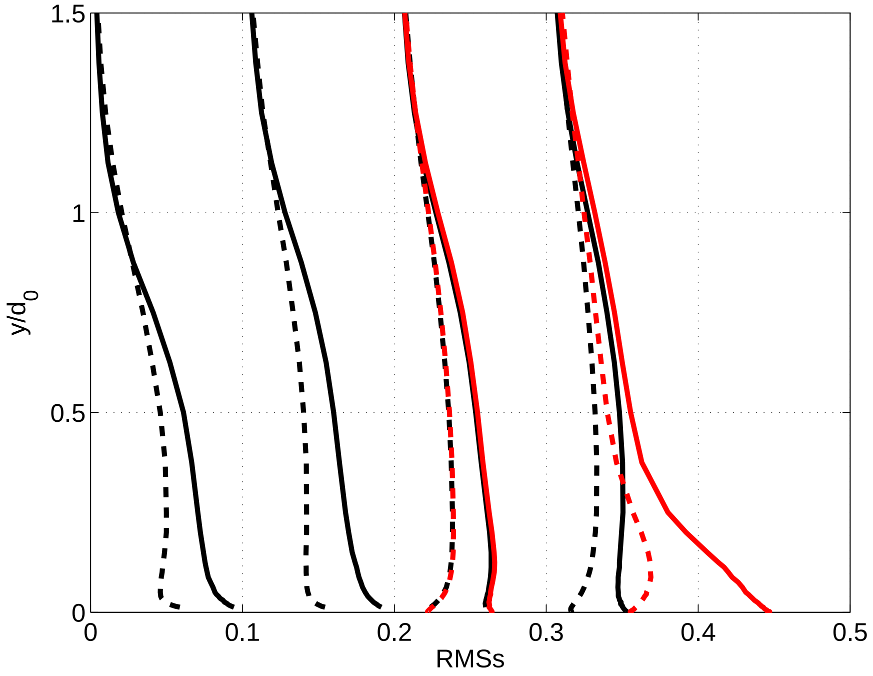

(a)

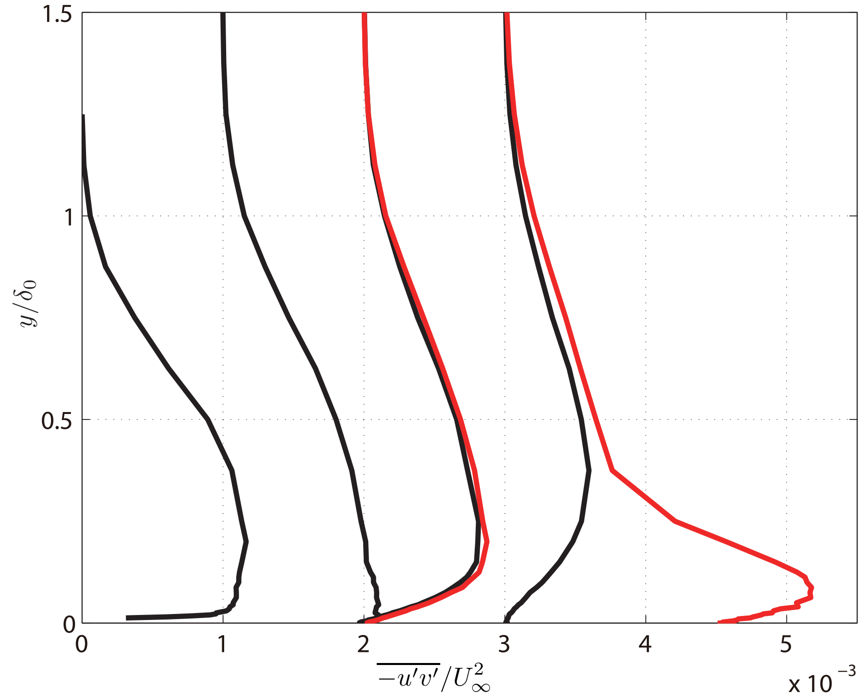

(b)

Figure A.10: 2nd order statistics: a) turbulent intensities as root-mean-squares, b) Reynolds shear stress. Black, without blowing; red, with blowing. In b), solid, streamwise; dashed line, wall-normal component.

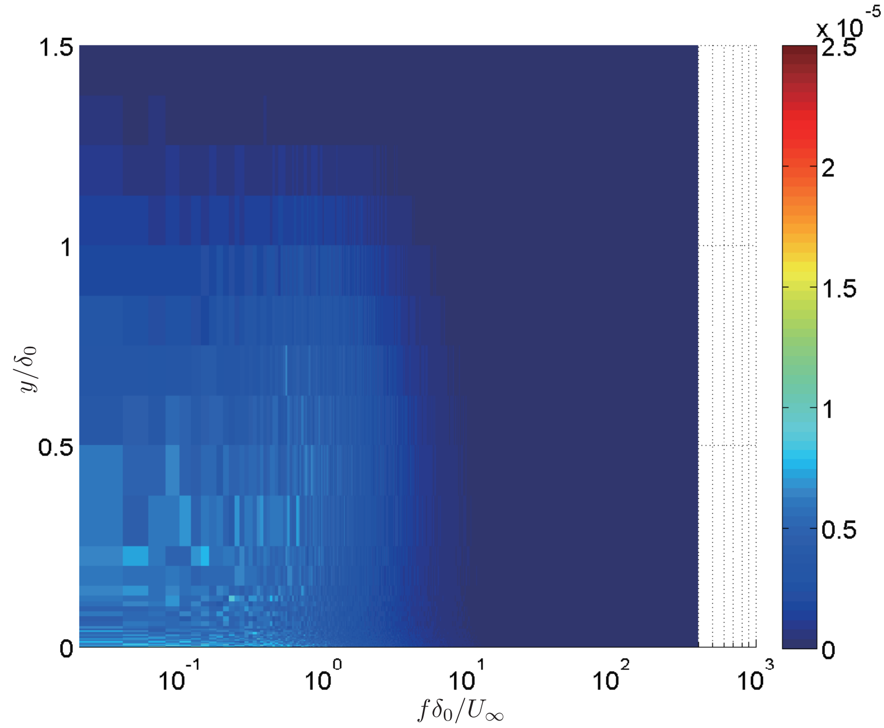

(a)

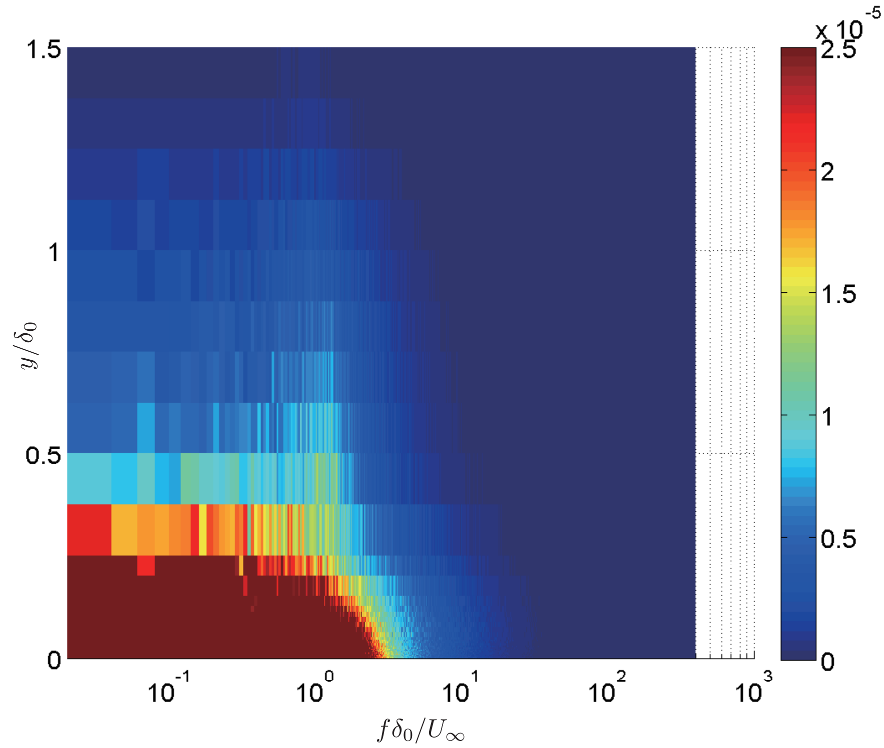

(b)

Figure A.11: Power spectral density of streamwise velocity: a) without blowing, b) with blowing.

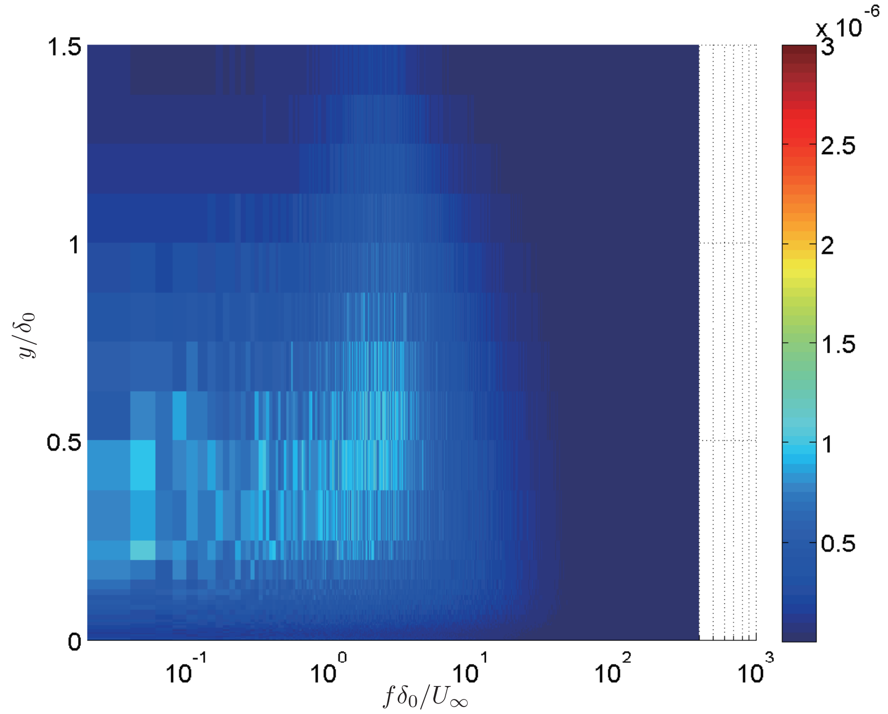

(a)

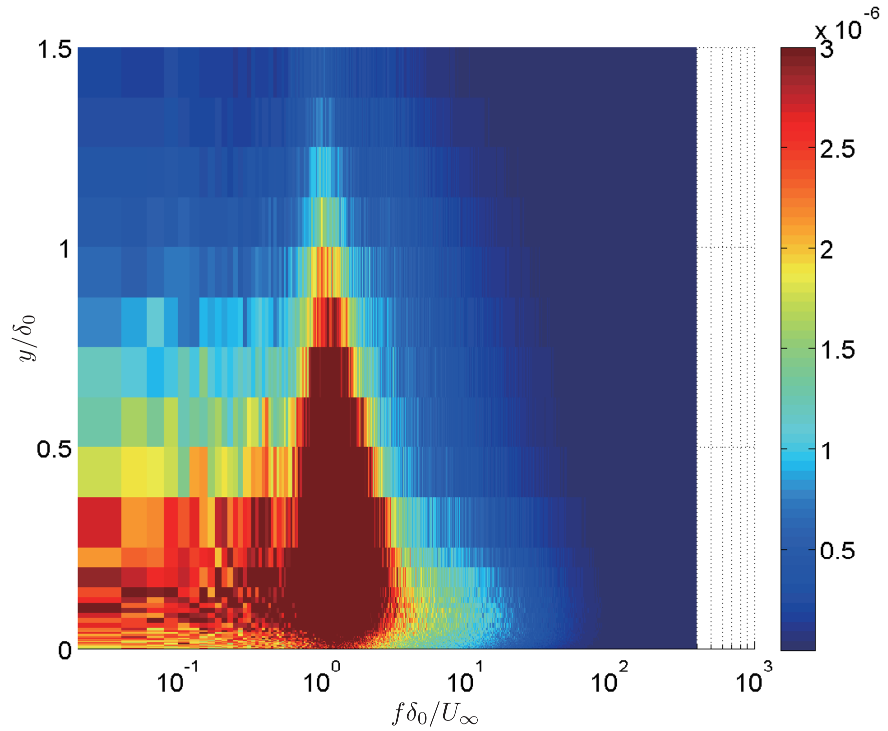

(b)

Figure A.12: Power spectral density of wall-normal velocity: a) without blowing, b) with blowing.

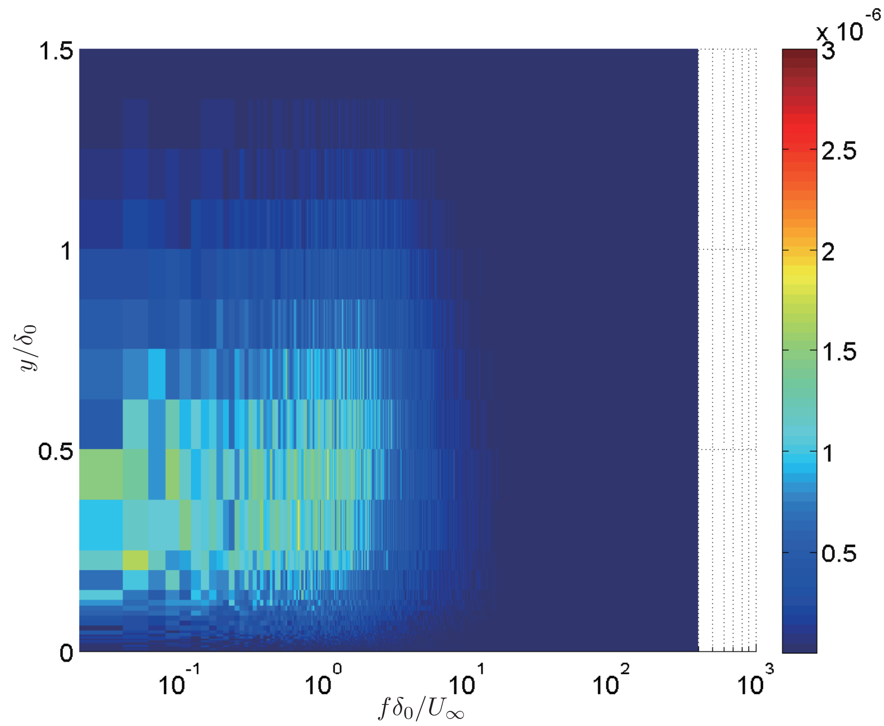

(a)

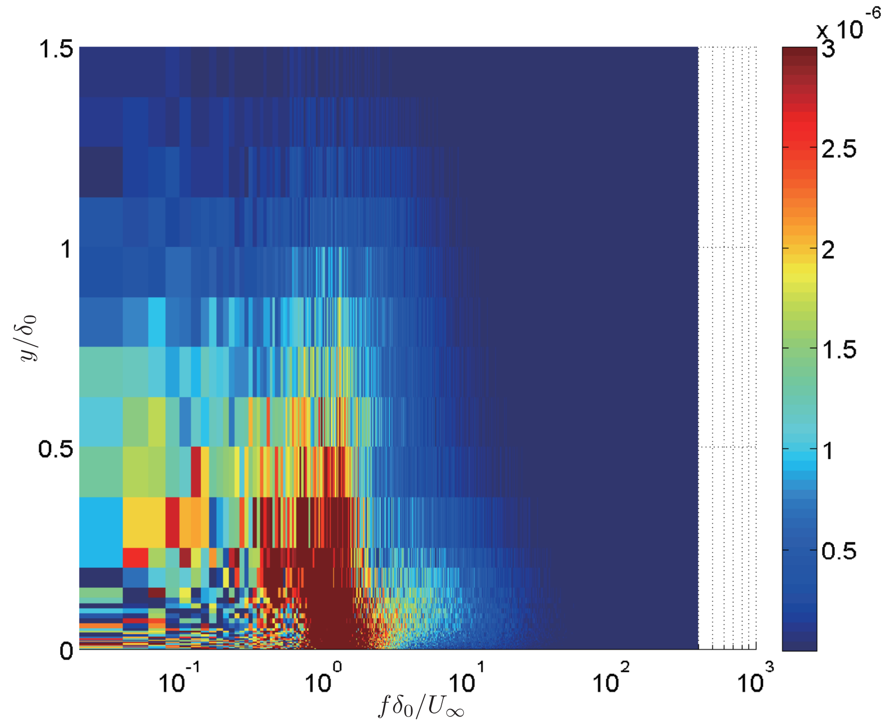

(b)

Figure A.13: Cross spectral density of streamwise and wall-normal velocity components: a) without blowing, b) with blowing.

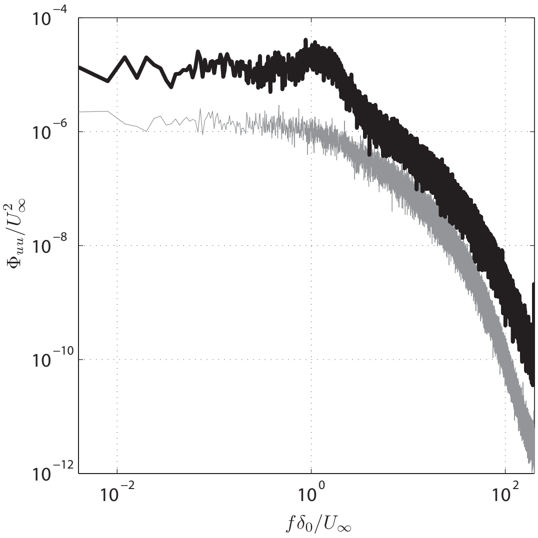

(a)

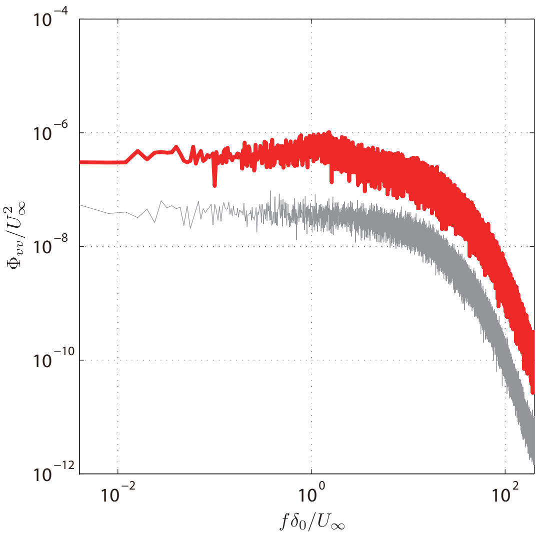

(b)

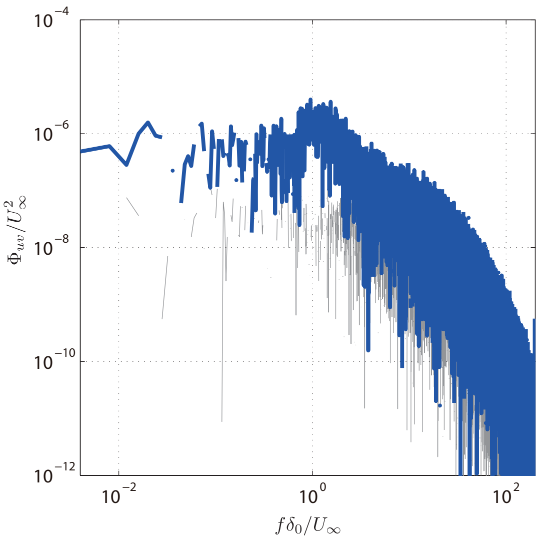

(c)

Figure A.14: Spectra with/without blowing at $y = 1$ mm: a) streamwise velocity fluctuations; b) wall-normal velocity fluctuations; c) Reynolds shear stress.

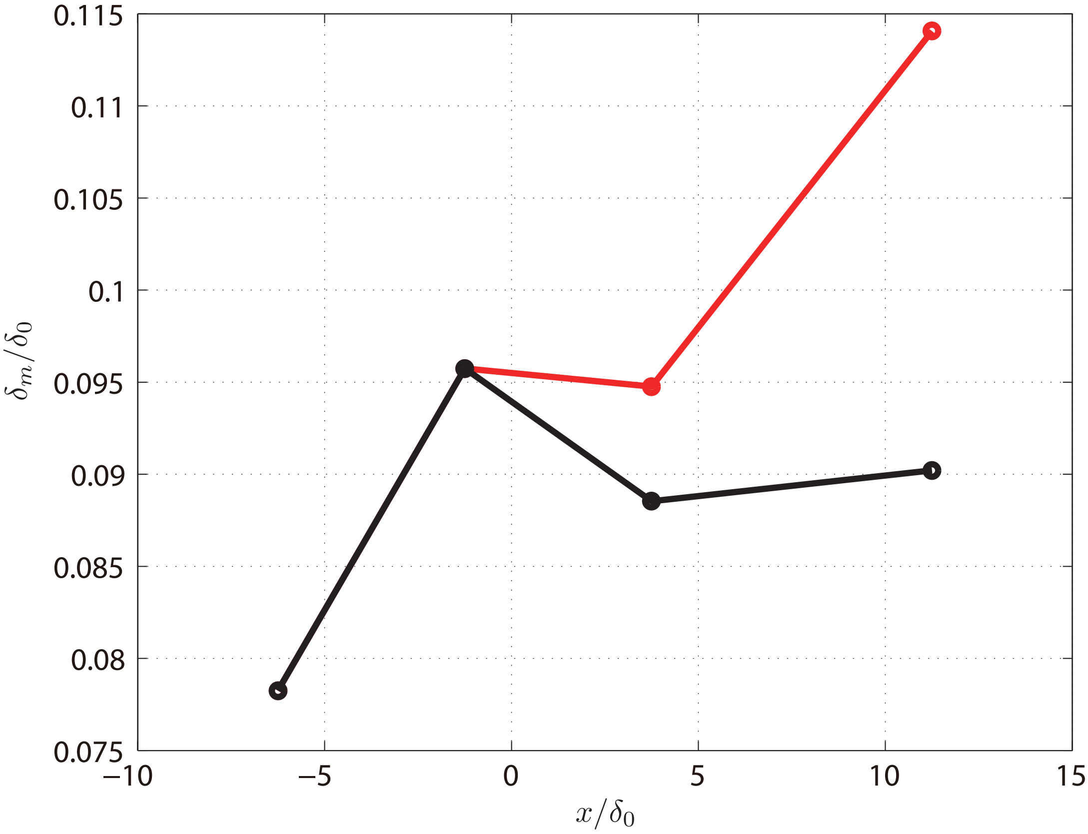

Figure A.15: Momentum thickness: black, without blowing; red, with blowing.

Table A.3: List of instruments

Name	Manufacturer	Model	Specification
thermometer	Nakamura-Rika-Kogyo	TA-5N	min scale: 1°C
low turbulence wind tunnel	set in JAXA		FST 0.05%
standard Pitot-tube	Okano-Seisakusho	LK-1	coefficient: 1.00
precision pressure difference sensor	Validyne	DP45-18	pressure range: 0-35 mmH_2O
precision pressure difference sensor amplifier	KRONE	PA-501	
constant temperature anemometer (CTA)	Kanomax	1011	
temperature unit	Kanomax	1020	
			diameter: 5μm
I-type hot-wire probe	Kanomax	0251R-T5	
X-type hot-wire probe	Dantec	55P63	
temperature compensation probe	Kanomax		

Name	Manufacturer	Model	Specification
support for dual sensor probe	Dantec	55H24	
traversing mechanism	Set in JAXA		for calibration of X-wires probe
traversing unit	self-built		*y*-direction
low-pass filter	NF corp.	3344	6th order Chevishev
A/D converter board	National Instruments	PCI-MIO-16XE-10	multifunction DAQ board, resolution: 16bit
BNC terminal	National Instruments	BNC-2120	
Blowing plate	Seika industry	Order-made	
Gast blower			
Compact size Inverter	Mitsubishi	FR-D720-0.75K	
measurement software	National Instruments	LabView 2010™	
signal processing software	MathWorks	Matlab 2011a™	
PC	HPC systems	Rack-Mount PC-500	CPU: Pentium4 2.66GHz, main memory: 1GB

Appendix B

Mach number dependency of drag reduction by the uniform blowing

B.1 Background and motivation

In the incompressible turbulent boundary layer, it is found that uniform blowing has skin friction drag reduction effect. To meat the increasing demand of high-speed transports, the investigation accounting for the compressibility of the flow is important. For not only aircrafts but also even bullet trains, the compressibility appears in the boundary layer on the body-surfaces because the compressibility cannot be neglected over $Ma \approx 0.3$. Japan Aerospace Exploration Agency (JAXA) has been developing the silent supersonic aircraft. Considering the environmental issue, the skin friction drag is the target to be suppressed.

The direct numerical simulation of compressible wall-turbulence has been performed: e.g., a channel flow of the Coleman et al. (1995) or Morinishi et al. (2004); a spatially developing turbulent boundary layer of Lagha et al. (2011a,b). The turbulent physics with compressibility is analyzed by Huang et al. (1995) with DNS data. The effect of skin friction drag reduction control examined in incompressible flow, however, is still unknown in the compressible turbulent flow. Here, direct numerical simulation of supersonic turbulent boundary layer is performed to investigate the Mach number dependency of the uniform blowing on the skin friction drag reduction.

Table B.1: Speficication of the compressible DNS code

Time integration	Low-storage third-order RK method
Advection term	Energy-conservative forth-order finite difference method
Diffusion term	Second-order Crank-Nikolson method

B.2 Numerical procedure

For compressible flow, the governing equations, continuity, Navier-Stokes and energy equations are non-dimensionalized as the followings;

$$\frac{\partial \rho}{\partial t} = -\frac{\partial \rho u_i}{\partial x_i}, \tag{B.1}$$

$$\frac{\partial \rho u_i}{\partial t} = -\frac{\partial \rho u_i u_j}{\partial x_j} - \frac{\partial p}{\partial x_i} + \frac{1}{Re}\frac{\partial \tau_{ij}}{\partial x_j}, \tag{B.2}$$

$$\frac{\partial \rho \theta}{\partial t} = -\frac{\partial \rho \theta u_i}{\partial x_i} - (\gamma - 1)\rho\theta\frac{\partial u_k}{\partial x_k} + \frac{\gamma}{Re\,Pr}\frac{\partial q}{\partial x_i} + \frac{\gamma(\gamma-1)M_\infty}{Re}\tau_{ij}\frac{\partial u_i}{\partial x_j} \tag{B.3}$$

All variables are non-dimensionalized by the free-stream quantities (ρ^*_∞, U^*_∞, θ^*_∞, μ^*_∞) and the 99% boundary layer thickness at the inlet of driver region of computational domain δ^*_0. The thermodynamical variables, ρ, θ, p are related one another by the perfect gas state equation, i.e.,

$$\gamma M_\infty p = \rho\theta. \tag{B.4}$$

The DNS code is based on that for an incompressible boundary layer performed in Chap. 2. The governing equations are discretized by the fourth-order fully conservative central finite difference method by Morinishi et al. (1998) for the convection term and the second-order central finite method for other terms. Similarly to the incompressible DNS code, the time integration is done by using the low-storage third-order Runge-Kutta/Crank-Nicolson scheme. Again, the computational domain is composed of two regions: a driver region and a main region, as illustrated in Fig. B.2. The recycling method (Lund et al. (1998); Lagha et al. (2011a)) is applied at the inlet of the driver region. The numerical schemes used for the present code are listed in TableB.1.

At the upper boundary, the streamwise velocity, temperature, and density are set to be identical to the free-stream quantities, while the wall-normal and spanwise velocities are set to be

$$\frac{\partial \rho v}{\partial y} = 0 \tag{B.5}$$

$$w = 0, \tag{B.6}$$

respectively. On the wall, no-slip condition, isothermal wall, and zero-gradient condition for the pressure are applied. Here, the temperature on the wall θ_w is estimated by using the Crocco-Busesmann approximation, i.e.,

$$\theta_w = 1 + \sqrt{Pr}\frac{\gamma - 1}{2}M_\infty^2. \tag{B.7}$$

The periodic boundary condition is used in the spanwise direction. The streamwise, wall-normal and spanwise lengths of the driver and main region are (L_x^D, L_y^D, L_z^D) = (L_x, L_y, L_z) = (10, 4, 3), where the superscript D denotes the driver region. The corresponding numbers of grid points are (N_x^D, N_y^D, N_z^D) = (N_x, N_y, N_z) = (256, 96, 128). The recycling station is located at $x^D = 6$. In order to prevent from artificial reflections from boundaries, the sponge layer (Adams (1998); Lagha et al. (2011a)) is settled on the upper and outer boundaries as shown in Fig. B.2. The sponge layers start at $x^D = x = 12$ and $y = 4$ in the driver region and the main region, respectively.

In the case with uniform blowing, a condition of constant wall-normal mass flow rate is applied on the wall. In this study, the Mach number is set to be $Ma = 0.4$ and 1.5 (denoted as MA0.4 and MA1.5) as the flow conditions. The Reynolds numbers based on the free-stream velocity, U_∞, the kinematic viscosity in free-stream, ν_∞, and the 99% boundary layer thickness δ_0 is set to be $Re_{\delta,0} = 4000$ and 7000, respectively, aiming at $Re_{\tau,0} = 200$ in both cases. The amplitude of blowing is fixed at $(\rho v)_w = 0.01$. The subscript w denotes the properties on the wall surface. The flow chart of present code is shown in Fig. B.1.

B.3 Base flow

The mean streamwise velocity in each case is plotted in Fig. B.3 with the data from incompressible turbulent boundary layer in the present thesis and the supersonic one at

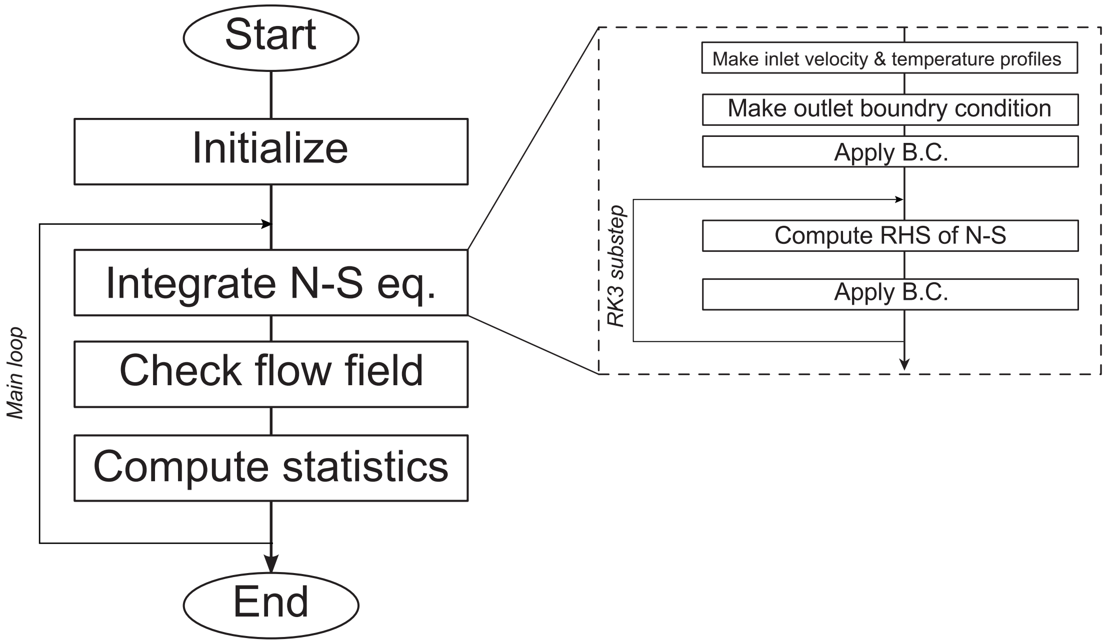

Figure B.1: Flow chart of the present simulation of the compressible turbulent bounder layer

$Re_\tau = 300$ (Lagha et al. (2011a)). By the non-dimensionalization with wall-units, it is found that all profiles collapse on the linear-law and log-law of the turbulent boundary layers. Vortex structure identified by using the Laplacian of the pressure is visualized in Figs. B.4 and B.5 to show the structures in MA0.4 and MA1.5. The skin friction coefficient in compressible flow is decomposed by the extended FIK identity (Gomez et al., 2009) as

$$c_f(x) = c^\delta(x) + c^T(x) + c^C(x) + c^D(x) + c^\mu(x) \tag{B.8}$$

$$\begin{aligned} &= \frac{4(1-\delta_d)}{Re_\delta} + 4\int_0^1 (1-y)\langle\rho\rangle\{u''v''\}\,dy \\ &+ 4\int_0^1 (1-y)\langle\rho\rangle\{u\}\{v\}\,dy \\ &+ \frac{4}{Re_\delta}\int_0^1 (1-y)\left(\langle\tilde{\mu}\rangle\frac{\partial\langle u\rangle}{\partial y} + \langle\mu\rangle\frac{\partial\langle v\rangle}{\partial x} + \left\langle\mu'\left(\frac{\partial u'}{\partial y}\frac{\partial v'}{\partial x}\right)\right\rangle\right)\,dy \\ &- 2\int_0^1 (1-y)^2\left(\frac{\partial\langle\rho u^2\rangle}{\partial x} - \frac{1}{Re_\delta}\frac{\partial\langle\tau_{xx}\rangle}{\partial x} + \frac{\partial\langle p\rangle}{\partial x}\right)\,dy, \end{aligned} \tag{B.9}$$

where the terms in the right-hand-side denote the contributions from the boundary layer thickness, the Reynolds shear stress, the mean convection, the compressibility, and the spatial development, respectively. Spatial development of each term is shown in Fig. B.6. It is found that the mean convection works as a reduction factor on the friction similarly to incompressible STBL.

The global FIK identity is defined by integration in the streamwise direction. The decomposed skin friction coefficient in MA0.4 and MA1.5 is shown in Fig. B.7. Similarly to the incompressible STBL, the dominant contributions are from the Reynolds shear stress, and mean convection, and spatially development similarly to the incompressible case. The compressibility terms are small even in the MA1.5 case. In the present simulation, the blowing is applied in the MA1.5 case only.

B.4 Results and discussion

The skin friction coefficient is defined as

$$c_f(x) = 2\frac{\tau_w^*}{\rho_\infty^* U_\infty^{*2}}, \tag{B.10}$$

where

$$\tau_w = \mu_w^* \left.\frac{\partial U^*}{\partial y^*}\right|_w. \tag{B.11}$$

The global skin friction coefficient results in $C_f = 4.2 \times 10^{-3}$ in MA1.5 case. The drag reduction rate, R, resulted in $R = 0.24$ in the present simulation. This result is almost similar to that in the incompressible case. Strictly speaking, it cannot be compared because the streamwise length to calculate C_f is shorter than that in incompressible case in present simulation. It is found that skin friction drag reduction effect of the blowing has little dependency on the Mach numbers in the present range.

The streamwise mean velocity profiles at $x = 5$ are plotted in Fig. B.8. The profiles shift away from the wall by the blowing. The shear stresses are shown in Fig. B.9. The Reynolds shear stresses are increased at distance from the wall, while the viscous shear stresses are decreased near the wall. These trends are similar to those in incompressible STBL (see Chap. 4).

Decomposed global skin friction coefficient in the cases without blowing case and with 0.1% UB cases are shown in Fig. B.10. The drag reduction seems to be achieved by the enhancement of the mean convection term, while the Reynolds shear stresses are increased. This trend is exactly similar to that in incompressible STBL.

B.5 Closure

The effect of skin friction drag reduction by uniform blowing from the wall was examined in supersonic turbulent boundary layers to investigate the Mach number-dependency of the uniform blowing on the wall. Skin friction drag reduction by uniform blowing is achieved in supersonic turbulent boundary layer at $Ma = 1.5$. In the present investigation, clear Mach number dependency between the $Ma = 1.5$ and the incompressible case was not found. To avoid the effect of sponge layer, the investigation using a longer computational domain in the streamwise direction should be performed. Moreover, examination in the wide range of Mach numbers should be performed in the future.

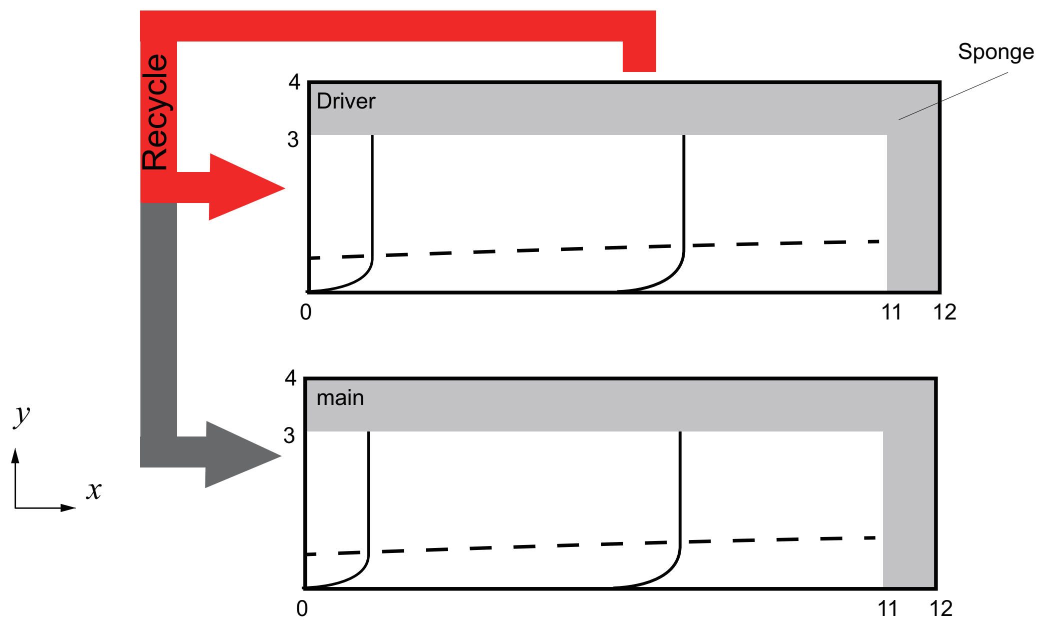

Figure B.2: Computational domain

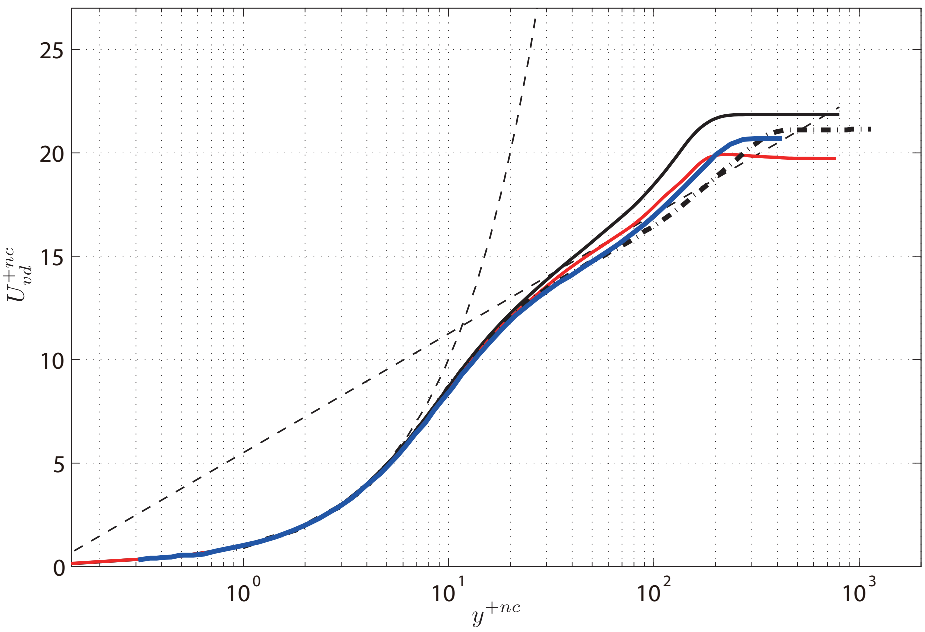

Figure B.3: Streamwise mean velocities at $x = 6$: black, $Ma = 1.5$; black, $Ma = 1.5$; red, $Ma = 0.4$; blue, incompressible flow in §3. Chain line, Lagha et al. (2011a) at $Re_\tau = 300$, $Ma = 2.5$.

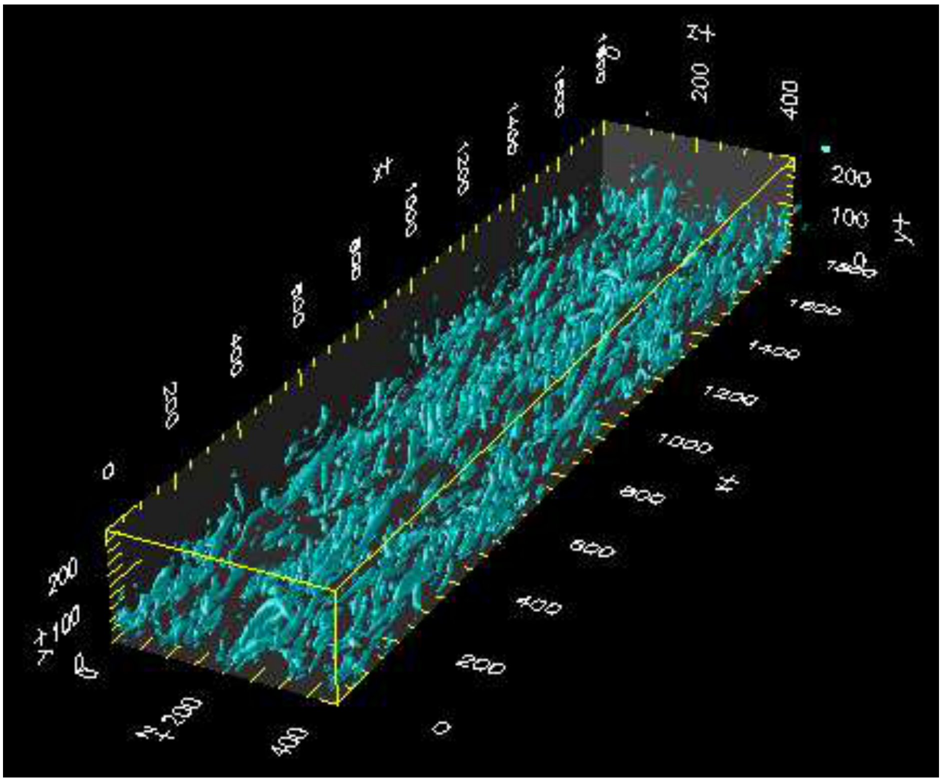

Figure B.4: Vortex structures

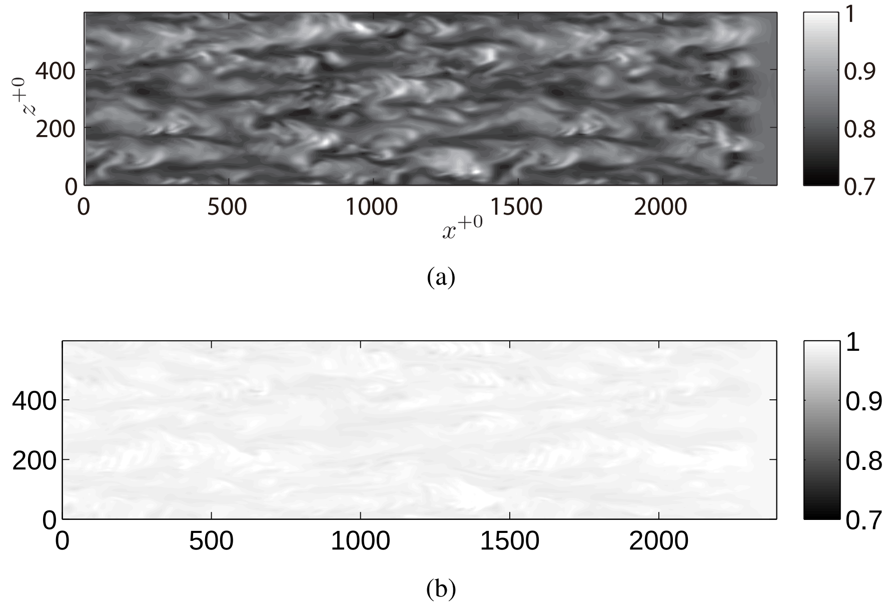

Figure B.5: Instantaneous density field in $x-z$ plane at $y^{+0} \approx 15$: (a) $Ma = 1.5$; (b) $Ma = 0.4$.

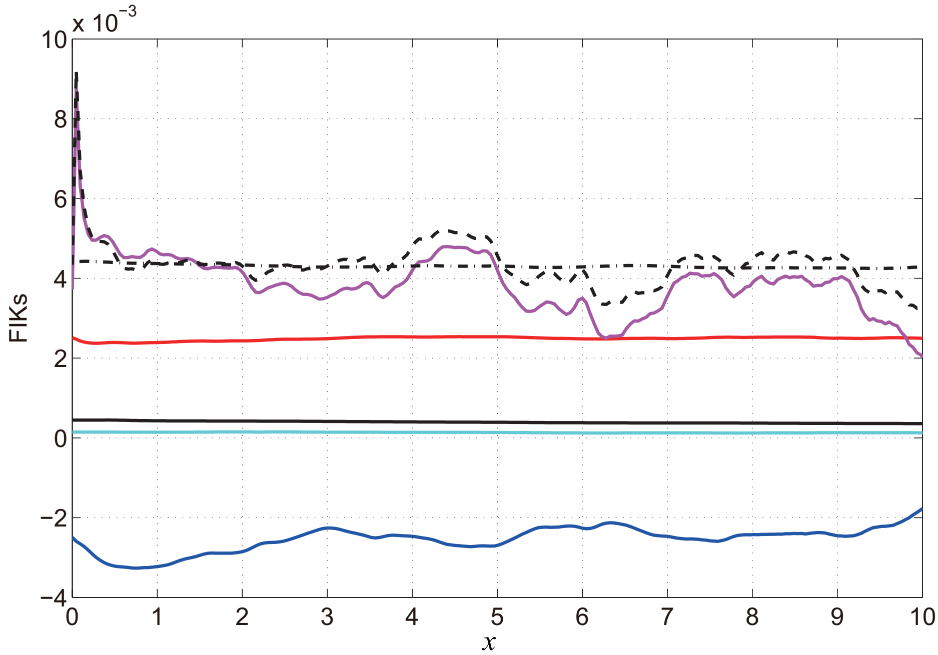

Figure B.6: Streamwise distribution of each contribution term in the FIK identity in $Ma = 1.5$: black-solid, boundary layer thickness term; red, RSS term; blue, mean

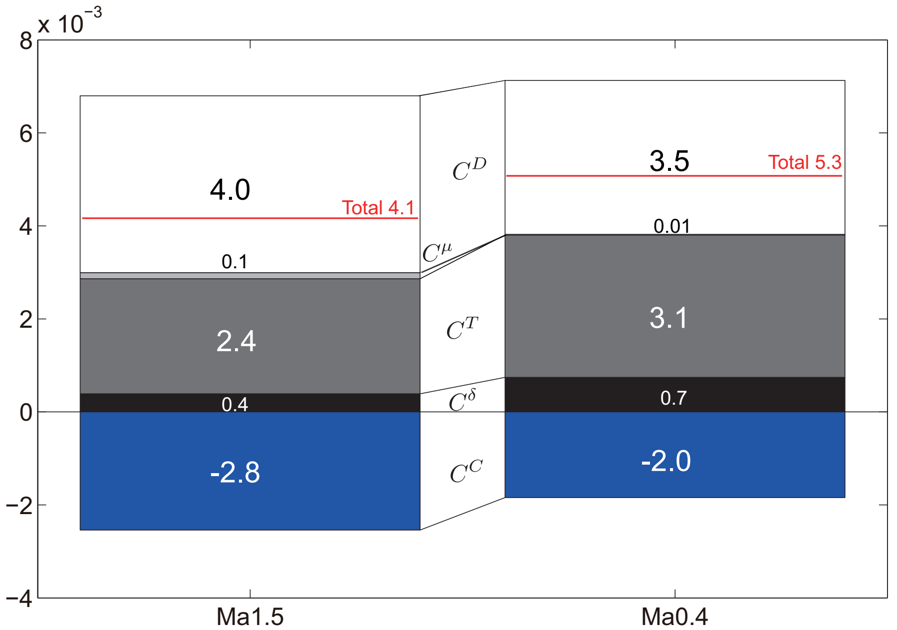

Figure B.7: Contributions to drag decomposed by the global FIK identity; a) $Ma = 1.5$, b) $Ma = 0.4$

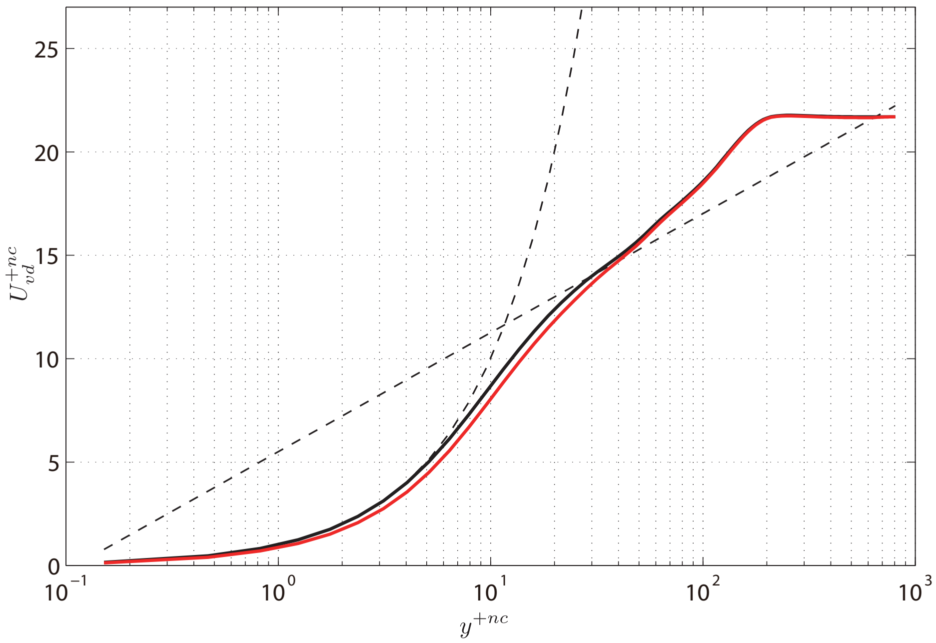

Figure B.8: Streamwise mean velocity at $x = 6$, $Ma = 1.5$: black, without blowing; red, 0.1% blowing.

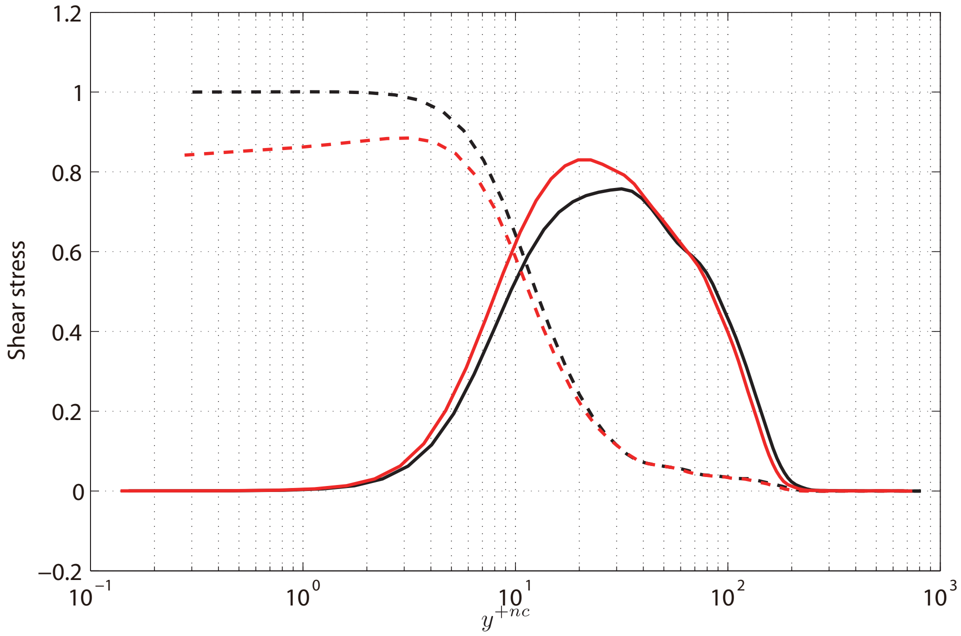

Figure B.9: Shear stresses at $x = 6$, $Ma = 1.5$: a) without blowing, b) 0.1% blowing.

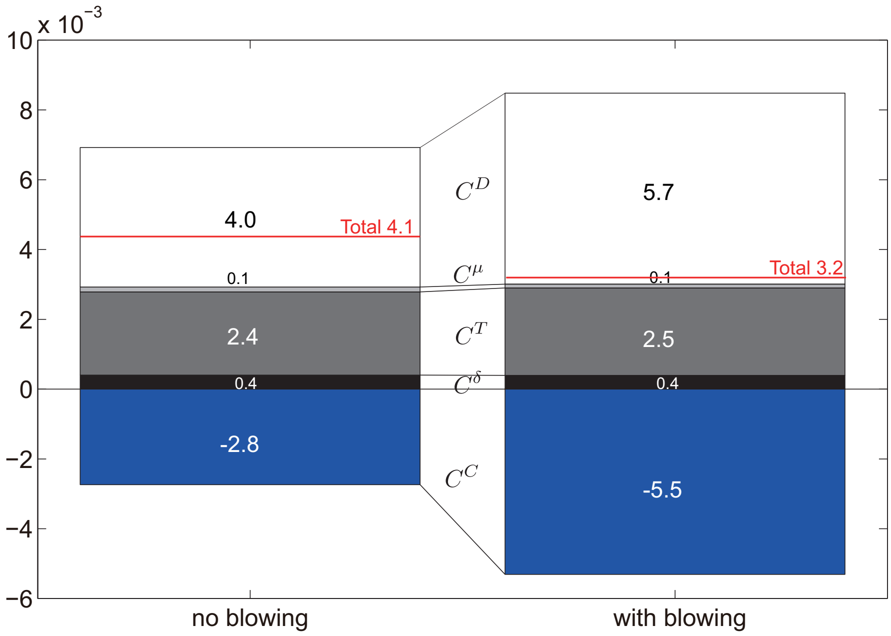

Figure B.10: Contributions to the drag decomposed by the global FIK identity at $Ma = 1.5$: black, without blowing; red, 0.1% blowing.